Understanding the astrophysical origin of silver, palladium and other neutron-capture elements

Camilla Juul Hansen

München 2010

Understanding the astrophysical origin of silver, palladium and other neutron-capture elements

Camilla Juul Hansen

Dissertation
an der Fakultät für Physik
der Ludwig–Maximilians–Universität
München

vorgelegt von
Camilla Juul Hansen
aus Lillehammer, Norwegen

München, den 20/12/2010

Erstgutachter: Achim Weiss
Zweitgutachter: Joseph Mohr
Tag der mündlichen Prüfung: 22 März 2011

Contents

Zusammenfassung

Hauptinhalt der Arbeit ist die Untersuchung von schwersten Elementen im Kosmos. Besonders ihr Ursprung ist von großem Interesse. Elemente, die schwerer als Eisen sind, entstehen in der Regel bei so genannten Neutroneneinfang-Prozessen, die bis heute noch nicht vollständig erforscht sind. Trotzdem wurden in den letzten Jahren große Fortschritte im Verständnis dieser Prozesse erzielt. Vor allem die Fragen nach dem Entstehungsort und Produktionsablauf schwerer Elemente stehen im Vordergrund dieser Forschungen. Abhängig von der Neutronendichte in ihrer Umgebung lassen sich Neutroneneinfangprozesse in zwei Arten unterteilen. Ist diese Dichte hoch, kann der Prozess dementsprechend schnell ablaufen und man spricht von einem r-Prozess (aus dem engl. rapid). Das Gegenstück stellt der s-Prozess dar (engl. slow), der wiederum in zwei Unterprozesse aufgeteilt werden kann. Im "Hauptprozess" werden schwere Isotope (wie z.B. Barium; $90 \leq A \leq 209$) gebildet, während der "schwache Prozess" die leichteren Isotope (z. B. Strontium; $56 \leq A \leq 90$) produziert. Diese s-Prozesse laufen hauptsächlich in Sternen ab, die sich im Hertzsprung-Russell Diagramm auf dem Asymptotischen Riesenast befinden. Durch die detaillierte Untersuchung der Elemente Pd und Ag in der vorliegende Arbeit finden sich auch für den r-Prozess Hinweise auf zwei Unterprozesse. Im Gegensatz zu leichteren Elementen wie Sauerstoff oder Magnesium waren Silber und Palladium vorher kaum untersucht worden, und stellten daher neben vielen anderen schweren Elementen nach wie vor weiße Flecken im Periodensystem dar. Diese Arbeit versucht nun erstmals ein paar dieser Fragen zu beantworten und das Verständnis des r-Prozesses zu verbessern. Um detaillierte Informationen der Elementhäufigkeiten in Sternen der Elemente Silber und Palladium zu erhalten, wurden hochaufgelöste Spektren mit hohem Signal-zu-Rauschverhältniss für Sterne in verschiedenen Entwicklungsstadien gewonnen. Die Spektren, aufgenommen mit UVES, einem Echelle Spektrograf im ultravioletten und sichtbaren Wellenlängenbereich, sowie mit dem hochauflösendem Echelle Spektrograf HIRES, wurden sorgfältig reduziert, so dass die stellaren Parameter und die Elementhäufigkeiten mit großer Genauigkeit bestimmt werden konnten. Dies geschah durch Anwendung von 1D Modelatmosphären in Verbindung mit synthetischen Spektren unter der Annahme lokalen thermodynamischen Gleichgewichts. Vergleicht man nun beide Elemente, kann man aus ihrem Verhältnis zueinander Schlüsse über ihre Entstehungsprozesse ziehen. Sind die Elemente miteinander korreliert, so bedeutet dies, dass sie aus dem gleichen Prozess hervorgehen. Eine Antikorrelation hingegen deutet auf verschiedene Entstehungsprozesse der beiden Elemente hin. Mit diesen Informationen ist es möglich, die Bildungsprozesse aller Elemente von Interesse (Strontium (Sr), Yttrium (Y), Zirconium (Zr), Palladium (Pd), Silber (Ag), Barium (Ba) and Europium (Eu)) zu analysieren. Der Vergleich der Häufigkeiten mittels Vorhersagen von nukleosynthetischen Modellen erlaubt es, die Vielzahl möglicher Entstehungsorte dieser Elemente einzudämmen und zu verstehen. Die Modelle beschränken sich auf zwei vorgeschlagene Szenarien: starke Winde nach Supernova Typ II Explosionen und massearme (schwache) Kernkollaps-Supernovae. Durch Untersuchung von Sternen mit nur einem Promille des Eisenanteils der Sonne bis hin zu den Sternen, deren Eisenvorkommen dem der Sonne sehr ähnlich ist, konnte die Entwicklung der schweren Elemente gut verfolgt werden. Während

der Analyse dieser unterschiedlichen Sterne wurden vier verschiedene Neutroneneinfangprozesse identifiziert. Des Weiteren wurde nachgewiesen, dass ein zweiter schwacher r-Prozess benötigt wird, um die Menge an beobachtetem Ag und Pd zu erklären. Dennoch müssen noch weitere metallarme Sterne untersucht werden, um diese Aussage zu festigen und sie auf die frühen Entwicklungsphasen der Milchstraße ausweiten zu können. Der Vergleich der Elementhäufigkeiten mit den Vorhersagen von Modellen hat außerdem gezeigt, dass entweder die astrophysikalischen Objekten z.B. sehr verschiedene Entropien haben müssen, oder dass zwei verschiedene Entstehungsorte für schwere Elemente existieren.

Abstract

Understanding the creation of the heaviest elements is the focus of this work. Elements heavier than iron are produced by the yet not fully understood neutron-capture processes. However, in recent years significant progress in understanding how and where these processes take place has been achieved. The neutron-capture processes are comprised of two different mechanisms, namely the slow and rapid neutron-capture process (the s- and r-process, respectively) which reflect both the duration and the neutron density of the processes. The s-process is subdivided into two channels, a main and a weak process, each responsible for creating heavy ($90 \leq A \leq 209$) and light ($56 \leq A \leq 90$) isotopes respectively (Heil et al. 2009). They are tied to asymptotic and red giant branch stars. For the r-process, there exists some observational proof of such a branching into main and weak processes. Detailed abundance analysis of elements like silver and palladium confirmed this. Until now these elements have not been studied in as much detail as many of the lighter elements (such as oxygen and magnesium). Silver and palladium together with many of the very heavy elements remain unknown 'gaps' in our understanding of the Periodic Table. The aim of my study is to shed light on these holes in our knowledge of the heavy elements.

In order to accomplish this, we need information from stellar abundances of the elements in question. This requires a detailed, high-resolution and high signal-to-noise stellar spectral abundance study of stars at different evolutionary stages. Our sample of stars was defined by stars spanning a broad range of stellar parameters. The stellar spectra observed with the Ultraviolet and Visual Echelle Spectrograph (UVES, Dekker et al. 2000) by Primas (2010) and the HIgh Resolution Echelle Spectrometer (HIRES, Vogt et al. 1994) required careful reduction to obtain the highest possible spectral quality. The stellar parameters were determined and the stellar abundances derived. This was carried out with 1D model atmospheres (MARCS, Gustafsson et al. 2008) and synthetic spectrum code (MOOG, Sneden 1973, v. 2009) under the assumption of local thermodynamic equilibrium.

By comparing the elemental abundances to each other, their pairwise correlation can be determined, which in turn provides the confirmation that the two elements originate from a similar process, or an anti-correlation predicting different formation processes of the elements. This will be used to map the formation processes of the seven heavy element under study (strontium (Sr), yttrium (Y), zirconium (Zr), palladium (Pd), silver (Ag), barium (Ba) and europium (Eu)).

Comparing their abundances to site dependent nucleosynthetic model predictions will provide constraints and understanding of the astrophysical object (site) in which the formation process takes place. Two model predictions are contrasted here; the high entropy winds after supernovae type II explosions (HEW Kratz et al. 2007; Farouqi et al. 2009) and the low mass (faint) O-Ne-Mg core collapse supernovae (Wanajo et al. 2010).

The evolution of these elements has been traced from old to very young stars. A range of different stars has been analysed and evidence of all above mentioned neutron-capture processes found.

Furthermore, proof of the necessity for a second 'weak' r-process yielding the observationally derived amounts of Ag and Pd is given here.

The comparison of the stellar abundances to the model predictions shows that the astrophysical site either needs to provide a range of entropies and neutron densities in order to explain the observationally derived abundance ratios of Sr - Eu, or that there is in fact a need for two different sites.

Chapter 1

Introduction

What can we learn from stellar abundances? The applications of stellar abundances are numerous and the knowledge we can extract from their ratios is extensive. Abundance ratios can be used to describe the chemical evolution of our Galaxy, the approximate age of Galactic stars, the formation processes of almost all the elements in the Periodic Table and several details about stars and stellar interiors such as mixing processes. My main interest focuses on the chemical evolution of our Galaxy and the nuclear processes that take place, enrich and develop the chemistry of the Galaxy. Different groups of elements in the Periodic Table can be used as tracers of various objects in the Galaxy. Very schematically, light elements such as hydrogen (H), helium (He) and lithium (Li) can be used to characterize the very early stages and epochs of the Galaxy just after the Big Bang, whereas the slightly heavier elements (such as O, Ne, Mg, Si, S, Ar, Ca and Ti) the so-called $\alpha-$elements, are important tracers of supernovae type II. Different $\alpha-$elements will describe specific features of the supernova explosion from which they were ejected. As the Galaxy aged, the abundances of the iron-peak elements (Cr, Mn, Fe and Co) experienced a rapid growth, as supernovae type Ia started enriching the chemical composition of the interstellar medium. Finally, the elements heavier than iron trace different end phases of various stars, and can constrain their masses and energies.

The exact formation processes of the elements vary, but they can generally be described as fusion processes, and among these are neutron-capture processes, which are responsible for forming the majority of the elements beyond the iron-peak. Simply put, the reason why elemental abundances derived from different environments can be used as tracers of the chemical evolution of the Galaxy is that they can be tied to different epochs of the Galaxy. Supernovae type II are, due to their large masses, expected to be very short lived and upon explosion, they leave behind their chemical traces in the interstellar medium of the Galaxy. Only at later stages will lower mass stars, hence longer hydrogen burning lifetimes, have had time to reach the state at which they can contribute to the enrichment of the interstellar medium. This means that the chemical feedback from different objects dominates at different Galactic ages, building up the Galaxy as we observe it today. Each chemical feedback event is mixed in the interstellar medium and enriched the gas from which later generations of stars will form. In the very early Galaxy though, only very few

supernovae have had time to recycle any gas, thus the previous generations of stars will carry imprints of only few supernova events. Large surveys like the HK and HES survey (see Section 1.4) were initiated between 1970 - 1990 searching for the oldest stars in the Galaxy with abundance signatures from the very first generation of supernovae, which are long gone.

Because the earliest stars in the Galaxy likely formed out of very pristine material, and because the metal enrichment builds up with time, metallicity[1] is usually taken as an age indicator. This is connected to the fact that very few stars have had time to recycle the gas and thereby enrich the interstellar medium with elements such as e.g. iron. However, the build-up of metal during the entire Galactic history encounters several processes, which makes it very difficult to correlate the age and the metallicity of Galactic stars especially of more recent times. In the last decade the very heavy elements turned out to be helpful in this connection. Heavy (radioactive) elements, such as uranium (U) and thorium (Th), have been detected in some extremely metal-poor stars. Since uranium has a relatively long lifetime compared to many other isotopes (^{238}U: $t_{half-life} = 4.51 \times 10^9$ years; Burbidge et al. (1957); Hill et al. (2002)), it radioactively decays to thorium. Therefore, based on their relative ratio as derived today, the age of the star can be estimated via radioactive dating. Unfortunately also the ages obtained in this way are very uncertain, due to assumptions that need to be made about the initial abundance ratios of both U and Th . Therefore, the age-metallicity relation remains highly debated (Nordström et al. 2004, and references therein). Historically, detailed knowledge and characteristics of the elements in the Periodic Table has developed from low atomic numbers to the very highest atomic numbers, and features and underlying formation processes are therefore not yet known for many of the very heavy elements. Understanding the origin and formation processes of some of these heavy elements is the main goal of my thesis.

1.1 Evolution of the formation processes

Only the very lightest elements such as hydrogen, deuterium (D), helium and a small fraction of lithium were created during the first ∼15 minutes after the Big Bang (Cayrel 2006) which yielded a primordial amount of these elements. At this point temperature and density in the universe had dropped so much that nucleons (protons, electrons, neutrons and positrons) were no longer in equilibrium ('dark ages' - see Figure 1.1) and other processes froze even earlier leaving behind a fixed amount of H, D, He and primordial Li. Millions of years later the first stars started forming (see Figure 1.1). Carbon (C), nitrogen (N) and oxygen (O) were formed in the first stars, which were very heavy due to the poor cooling that hydrogen offers compared to carbon. These stars could be hundreds of solar masses (Bromm 2010; Heger & Woosley 2002) and would therefore be very short lived. Despite being short lived these massive objects would end the dark ages and in a

[1]The metallicity referred to here is not the general Z from Galactic chemical evolution models, but the iron abundance, which spectroscopists tend to refer to as metallicity. Furthermore, any element heavier than helium is referred to as metals.

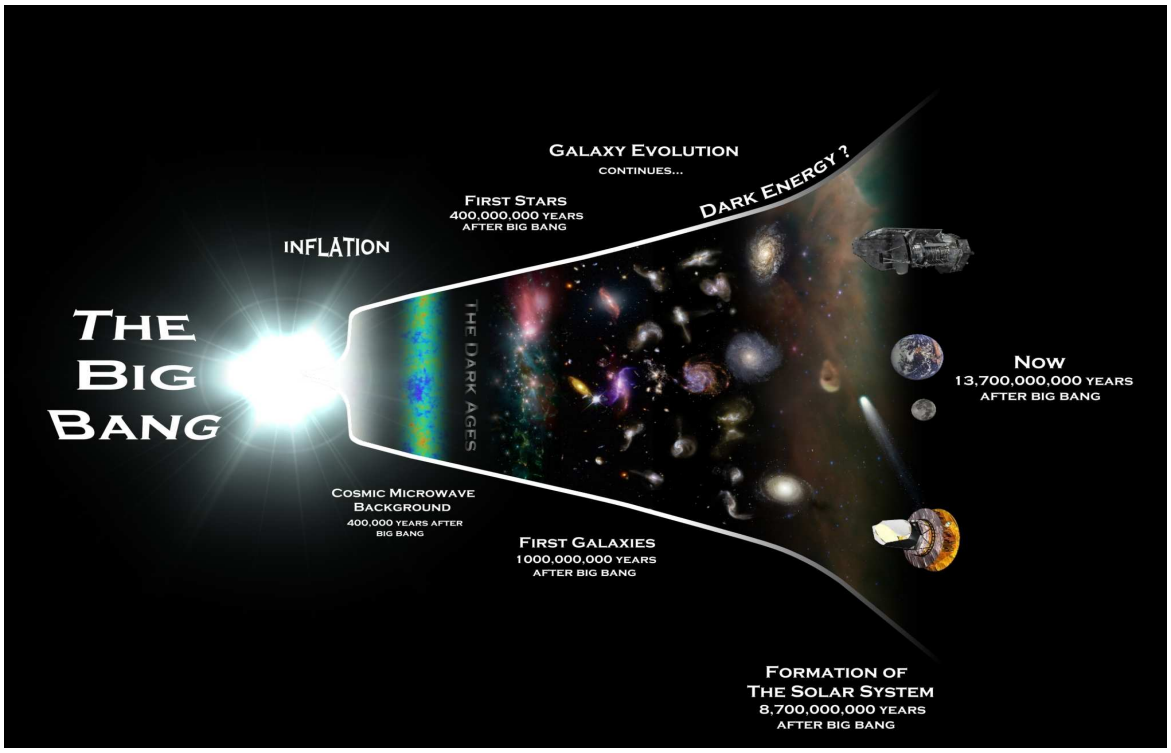

Figure 1.1: A picturesque evolution of the Universe, showing the evolution from the Big Bag through the dark ages via star formation to galaxy formation and finally present time, where we are sending satellites into space. Rough estimates of the time at which the first stars and galaxies were formed are given in the figure (http://planck.cf.ac.uk/files/Timeline_portrait.jpg).

hierarchical scenario build up the galaxies as shown in Figure 1.1. During their life time, these first stars would synthesize elements from C up to the iron-peak via fusion reactions, beyond which these become too energetically demanding to take place via silicon burning in the stars. Their stellar core would then start to collapse and subsequently explode. After a very energetic explosion they could inject these elements to the so far metal deprived interstellar medium (ISM). The details of this enrichment from the very first stars is to date only speculative (because they have never been observed), despite the many searches that have been carried out. Even though today's telescopes are powerful, it is not possible to observe these objects that are long gone. Beyond the iron-peak a lot of seed and energy is needed in order to synthesize the so-called heavy elements. The above mentioned explosion may indeed release the necessary energy and seed particles like neutrons and protons. This environment may under the proper conditions lead to neutron-captures onto already created α- and iron-peak elements and thereby create the heavy elements.

The majority of the heavier isotopes are produced by neutron-captures, and depending on the neutron density, different processes (or reaction channels) will create different ele-

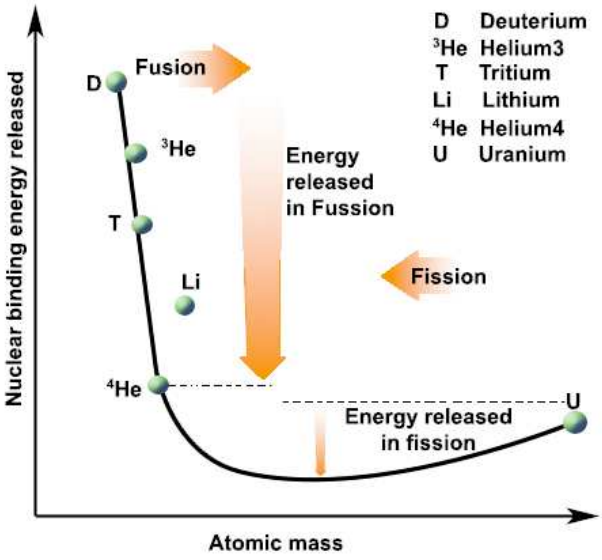

Figure 1.2: Binding energy per nucleon as a function of atomic mass. The minimum is found at proton number 30 after which the process becomes endothermic and will require energy, hence fission takes over for a while and creates free building seeds, which in turn can form the heaviest elements e.g. via neutron-capture processes (http://resources.edb.gov.hk/physics/articlePic/AtomicPhysics/starmaker_pic01.jpg).

ments (isotopes). There exists a slow and a rapid neutron-capture process, s- and r-process, respectively. The s-process is a secondary process, it takes place at relatively low neutron densities and it needs a seed to built onto. This process cannot take place in the very early Galactic stages, where there are no (or very few) suitable seeds to build onto, but it can only set in after the seeds have been created. Furthermore, the s-process can only occur once the stellar sites have had time to develop (more details in section 1.2). The r-process, on the other hand, is a primary process, i.e. the process can itself create free nucleons as well as heavier elements (e.g. iron-peak elements) and continue capturing neutrons onto the heavier seeds without needing any 'external' particles (Meyer 1994). This process only occurs in environments with large neutron densities. It also tells us that the r-process will take place before the s-process. This information is crucial to understand the formation process of the heavy elements detected in the earliest stars, since these elements must have been formed by an r-process. Some isotopes can only be created by the r-process, others only by the s-process and some have a double contribution. This depends on the beta-decay rate[2] and the neutron-capture rate. Generally speaking, the s-process creates between half and two-thirds of the heavy isotopes, and the r-process between one third to half (Meyer 1994). A proton-capture process (p-process) created the remaining few isotopes. Further

[2]The decay of the radioactive unstable isotopes, during which a neutron will be converted to a proton and an electron, see equation 1.5.

details about the neutron-capture processes can be found below.

1.2 Neutron-capture processes: The historical perspective

Ground breaking discoveries associated with stellar nucleosynthesis and hence neutron-capture processes were made by Burbidge, Burbidge, Fowler and Hoyle (B^2FH, Burbidge et al. 1957), and since then, several people have been working on the s- and r-processes, revealing more about these processes. Some of the reasons why the B^2FH paper became so popular were partially because they described the various nuclear processes ranging from hydrogen-burning to the r-process in great detail. The authors were among the first to relate all these processes to stars and not to different stages of the primordial gas as was previously done.

Details on abundance curves of all heavy elements were presented, describing clearly that both the r-process and the s-process have three abundance peaks, at the following atomic mass numbers, $A_{r-process} = 80, 130, 196$ and $A_{s-process} = 90, 138, 208$[3]. The creation of isotopes, around the peaks can be calculated from reaction cross-sections and rates versus beta-decay rates. Briefly said, B^2FH focused on the reactions and the underlying nuclear physics. In 1965 Seeger et al. made a careful experimental study of how r- and s-processes contribute to different isotopic abundances. They suggested that there were two r-process channels working at different temperatures and densities. Even though the differences were small and the site very suggestive, this was significant progress compared to what could be obtained ten years earlier. B^2FH had suggested that low-mass supernova type I should be the site of the r-process; Seeger et al. (1965) confirmed the need of an explosive site. An explosive environment was clearly needed to reach the temperatures and neutron densities in the short time intervals, during which they expected the r-process to take place and create elements at all three nuclear peaks. They estimated the mass of the r-process site to be $\sim 10^5 M_\odot$, and suggested that these massive objects could be a kind of quasi-stellar radio object. Even though both mass and site turned out to be wrong, their calculations clearly indicated that the r-process site had to be massive and explosive (which is still what we believe today).

Thirty years later, Meyer (1994) was able to further characterize the s- and r-process and their main features. He described the r-process as a primary freeze out process[4], and the s-process as a secondary process falling short of equilibrium. In both cases he emphasized that the processes work outside nuclear statistical equilibrium (NSE), and that isotopes are created away from equilibrium, and will decay and become stable. The NSE is achieved

[3]These three numbers correspond to the atomic masses of the last three magic neutron numbers: $N_{Magic} = 2, 8, 20, 28, 50, 82, 126$, which coincides with the number of nucleons it takes to complete an atomic shell. A full shell leads to larger binding energy of the nuclei (more stable nuclei) and in turn leads to larger abundances, since these nuclei are less likely to decay.

[4]A process that takes place once the temperature drops.

in a thermally isolated system, where the nucleon's macroscopic states share the energy of the system in such a way that the maximum entropy is obtained.

Due to the very large neutron density available for the r-process, r-process nuclei can be build without the need of seed elements from the external sources (as mentioned in section 1.1). This primary process will create the heavy seeds (iron-peak nuclei) as well as the free nucleons and the large neutron density ($n_n \sim 10^{26}$ Kratz et al. 2007) would then lead to a bombardment of this (iron-)nucleus until it becomes very massive (see Figure 1.3) and subsequently beta-decays. This would continue until the process ceases either due to seed exhaustion or dropping temperature (freeze out). This is why this process is primary, while the s-process is secondary. The latter process needs a much lower neutron density ($n_n = 10^8$, Busso et al. 1999) and will need a seed, like an iron-peak nuclei to build onto.

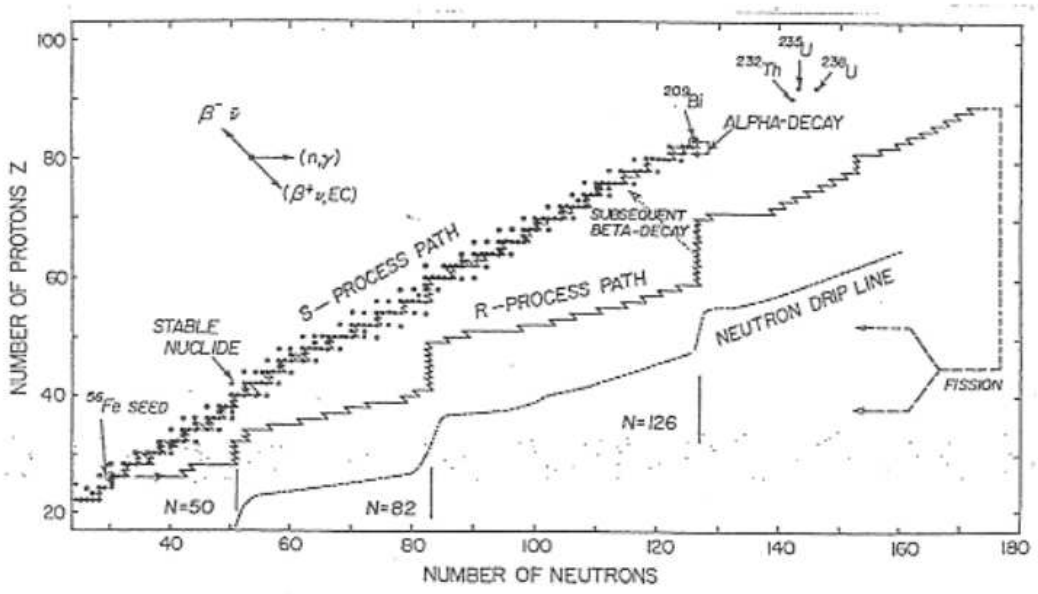

Figure 1.3: A schematic figure of the creation of heavy elements showing the increase in number of protons as a function of the neutrons. The r-process peaks are indicated with vertical lines (magic neutron numbers, N = 50, 82, 126). The s-process takes place close to stability, whereas the r-process is positioned further away from stability. An indication of the direction of neutron-captures and beta-decays are given in the upper left corner to guide the reader (http://www.alaskajohn.com/physics/charts/binding_energy.jpg).

In the last decade also the s-process has been further characterized and divided into two components; a main (or classical) and a weak component. The sites and reactions leading to these two different reaction channels will be discussed in Section 1.3.
Both theoretical and observational studies have found increasing indications of a similar scenario for the r-process, as tentatively suggested by Seeger et al. (1965). More recently

Cowan et al. (2002) revealed a great deal about the r-process, and they are some of the frontiers in the field of theoretically exploring the behaviour of the r-process. The site of the rapid neutron-capture process is still being debated, but recent theoretical studies have suggested various scenarios (see Figure 1.4).
Freiburghaus et al. (1999), suggested neutron star mergers
Wasserburg & Qian (2000), proposed high mass supernovae
Wanajo et al. (2001), neutrino-driven winds
Wanajo et al. (2003), low O-Ne-Mg supernovae
Argast et al. (2004), core-collapse supernovae and Farouqi et al. (2009), high entropy winds.
Despite the variety of sites having been and/or being explored for the origin of the r-process (see also Figure 1.4 and Section 1.4), most of them seem to imply the need for a second r-process in order to explain observationally derived abundances of the heavy elements (see Figure 1.6 and 1.7).

1.3 Features and description of the neutron-capture processes

Depending on the neutron density a slow or rapid neutron-capture process will take place. The s-process works through two channels as the r-process is thought to. The site, yields and reactions of the various n-capture processes are described below.

The main component of the s-process is thought to take place in asymptotic giant branch (AGB) and red giant branch (RGB) stars (see Figure 1.4) in the mass range 1.5 to 8 $M_{\odot}$ (Sneden et al. 2008) and is generally associated with ^{13}C reactions creating the elements with atomic masses of $90 \leq A \leq 209$ (Heil et al. 2009). These reactions take place in carbon-rich pockets in the helium-burning inter-shell. Neutrons will be released from $^{13}C(\alpha,n)^{16}O$ reactions, where the ^{13}C is created by ^{12}C burning in the stellar core (central parts where the temperature is high enough to allow this burning). The third dredge up[5] then brings the neutron-capture products up through the hydrogen-burning shell and further through the convective H-rich envelope to the surface. The weak s-process was recently defined by Heil et al. (2009) and Pignatari et al. (2010) to create the lighter elements in the range $56 \leq A \leq 90$ via $^{22}Ne(\alpha,n)^{25}Mg$ reactions in He core burning in more massive stars ($M \geq 8\ M_{\odot}$).

For both s-process channels the neutron-capture is of similar or longer duration compared to the β^--decay, which means that these processes take place close to stability (see the black stable nuclide in Figure 1.4). The neutron can be captured onto a heavy, stable seed (proton number: Z, atomic mass: A) and decay:

[5]A deep convective motion, which brings material from the surface to the center and from the centre to the surface, thereby possibly changing the chemical composition of the star's atmosphere. The third dredge up takes place during the late pulsating asymptotic giant phase.

$$(Z, A) + n \rightarrow (Z, A + 1) + \gamma \tag{1.1}$$

this nucleus is unstable and can decay

$$(Z, A + 1) \rightarrow (Z + 1, A + 1) + e^{-} + \overline{\nu_e} \tag{1.2}$$

or if the neutron density is very high the unstable nucleus might capture another neutron before decaying,

$$(Z, A + 1) + n \rightarrow (Z, A + 2) + \gamma \tag{1.3}$$

where n is a neutron, ν_e electron neutrino and $\overline{\nu_e}$ its anti-neutrino, p a proton and e an electron, e^{+} the positron and γ represents gamma radiation. The r-process will typically go through several of the reactions in equation 1.3 before decaying which causes a shift far to the right of the stability shown in Figure 1.4 (see the blue squares which identify the r-process isotopes). In this case the neutron-capture is much faster than the β^{-}-decay (due to the large neutron density).

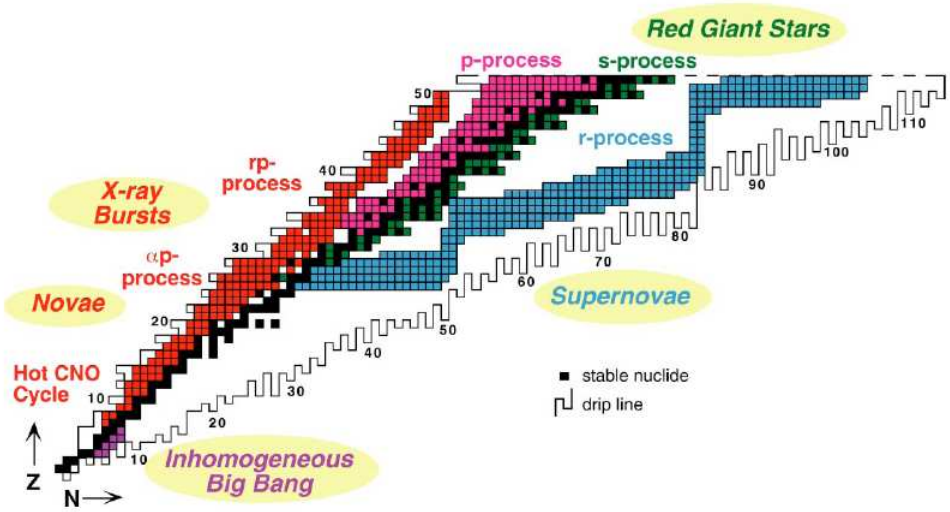

Figure 1.4: A schematic illustration of the neutron-capture processes with site suggestions indicated in bubbles next to the isotopes. Shown is the number of protons as a function of neutrons. The black squares are stable isotopes, indicating that the s-process takes place close to stability, whereas the r-process (blue squares) is shifted towards more neutron-rich isotopes.

In Figure 1.4 the formation of the r-process elements is associated with supernovae, which reflects one of the most common assumptions currently being made. In this scenario, prior to the supernova explosion, a stellar core with high energy is contracting. It is too energetically demanding for the Si-burning core to fuse elements beyond the iron-peak.

The nuclei in the core will start capturing the very energetic electrons, since this is energetically favourable and thereby release a lot of neutrons and neutrinos (Christensen-Dalsgaard 2004). The reaction taking place is the following:

$$(Z, A) + e^- \rightarrow (Z - 1, A) + \nu_e \tag{1.4}$$

The number of electrons will drop, which means that the electron-to-baryon ratio (electron fraction), Y_e, will drop as well. This, in turn, leads to a drop in electron pressure, which will lead to a free collapse, when the electron pressure is too low to sustain the gravity. The density of the core will increase and once the value is around $\rho \sim 10^{14} g/cm^3$, the so-called homologous core (Christensen-Dalsgaard 2004), will trap the neutrinos. At some point the core cannot contract any more because nuclear densities are reached (it has become a neutron star) and the sound speed in the core will be larger than the velocity of the in-fall, thereby turning the collapse into an outgoing shock wave. This is also known as the bounce off on the homologous core. The highly energetic shock front dissociates matter on the way outwards. This dissociation depends on the energy of the shock. If the energy is high enough to push through the amount of material it has to travel through, the supernova will explode. The newly made neutron star will try to cool down and thereby eject neutrinos. These lead to a neutrino burst from the 'hot bubble' in which the neutrino pairs will annihilate and try to transfer energy to the surrounding matter via weak force interactions. If the material in this bubble is sufficiently hot and energetic, parts of it will escape from the gravitational potential of the supernova (SN) and the newly formed neutron star. In supernova models the amount that escapes is determined by the so-called mass-cut. The hot bubble has a high entropy and the anti-electron-neutrinos emitted as coolants of the neutron star, will drive the second reaction in equation 1.5 to the left, resulting in a neutron excess. The neutrino reactions taking place are as follows:

$$n + \nu_e \rightarrow p + e, \qquad \text{and} \qquad \overline{\nu_e} + p \rightarrow n + e^+ \tag{1.5}$$

which shows the 'cycling' of neutrons and neutrinos that in turn provides neutrons for the neutron-captures. The neutron excess in the hot bubble is of fundamental importance for the r-process. In order to understand how much r-process material will be ejected into the interstellar medium (ISM), parameters such as Y_e[6], density, temperature, entropy and mass cut need to be known and properly accounted for in the SN models. To date, this has only been handled through approximations, but a lot of progress has been made in this field, leading to better and more solid isotopic yield predictions. The derived abundances are compared to some promising model predictions in Chapter 6.

1.4 What is known from observations?

This section introduces observational progress and obstacles related to studying neutron-capture elements and it shows how observationally derived abundances indicate the exis-

[6] $Y_e = \frac{Z}{A}$

tence of more than one r-process.

Telescopes and spectrographs are very efficient nowadays and can achieve very high resolutions. These, combined with very high S/N ratios, which we can reach in reasonable amounts of time, allows us to derive very accurate stellar abundances.

One of the main reasons we made progress only recently is because most of the heavy elements show very weak lines in the stellar spectra. High quality spectra are needed in order to resolve and detect these weak lines, which mostly fall below 4300 Å (Sneden et al. 2003). Furthermore, a large part of these neutron-capture elements display their lines in the near-ultraviolet spectral range down to (or below) the atmospheric cut-off, which clearly requires very sensitive near-UV spectrographs. Thanks to this last generation of UV sensitive spectrographs mounted on 8-10 m class telescopes (HIRES (Vogt et al. 1994) at Keck, UVES (Dekker et al. 2000) at VLT and HDS (D'Odorico 1998) at Subaru) accurate abundance studies of elements such as silver are now possible.

Figure 1.5 shows 40 Å in the near-UV and the visual. From this it is evident that dealing with lines in the near-UV is difficult due to all the line blends, and furthermore that the high-resolution is needed to resolve and distinguish all these lines. Silver is found at 3280.7 Å and 3382.7 Å (the first line is included in the left-hand figure) and barium can be found at e.g. 4934 Å a line which is shown in the right hand plot. These plots illustrate that it is more straightforward to measure the equivalent width and determine the continuum in the region around Ba than around Ag, however, there are no other regions which include silver lines, hence the necessity for dealing with near-UV wavelength ranges.

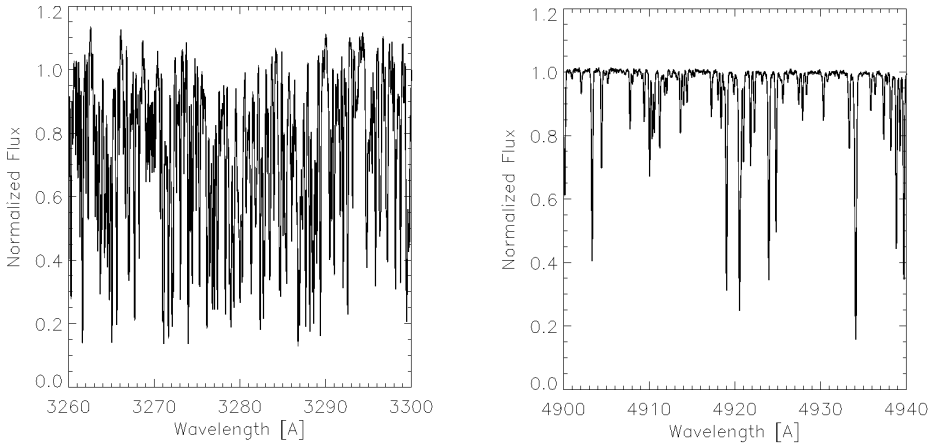

Figure 1.5: To plots of the same star, HD122956, both showing a wavelength range of 40Å . The figure on the left shows how crowded the UV region around the bluest (3280 Å) silver line is, whereas the figure on the right indicates a region around a Ba line (4934 Å) in the visual where less blends occur.

The alpha elements show the clearest abundance correlation with [Fe/H][7] with a low

[7]This is a standard abundance notation, where number densities are scaled with respect to the Sun.

star-to-star scatter (Cayrel et al. 2004) followed by the iron-peak elements. This was not the case in 1995, when McWilliam et al. noted that a considerable fraction of the error on the abundances, was due to observational uncertainties. From their analysis of medium-resolution spectra with a S/N $\sim$ 35, they found that the observational error on equivalent widths[8] larger than 60 mÅ had a 10% observational error, while equivalent widths below 10 mÅ had an 80% error! This meant that very weak lines, such as those for silver, could not be detected because of observational errors stemming from data reduction and low spectral resolution. Intermediate and strong lines would still yield trustworthy abundances. Today this kind of error is minimal, which means that the trends, correlations and scatter we see in abundance plots are real and due to formation processes, and not due to instrumental insufficiencies.

Neutron-capture elements, on the contrary, tend to show much larger scatter in their abundances compared to alpha elements. This is discussed in detail in Chapter 5, where formation processes of target elements are discussed. For instance barium shows a star-

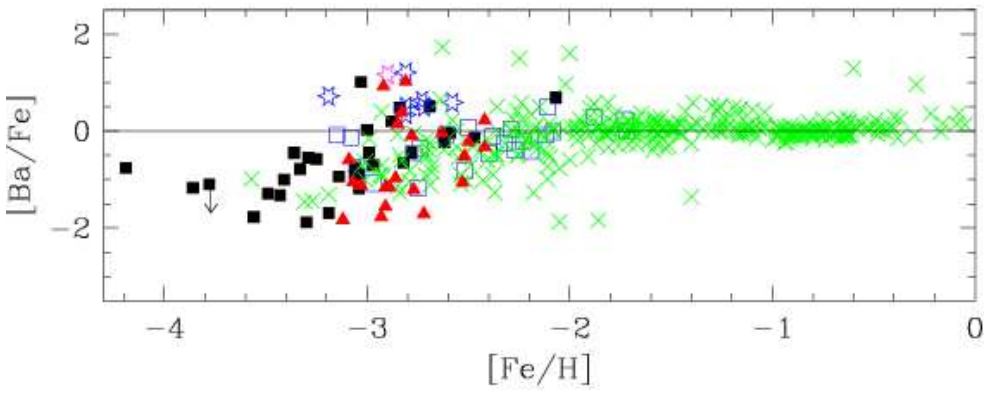

Figure 1.6: This figure is taken from François et al. (2007) and shows different studies of [Ba/Fe] plotted as a function of [Fe/H]. The star-to-star scatter is large and [Ba/Fe] covers a range of almost 4 dex. The large scatter indicates that the inhomogeneous ISM consisted of very different Ba yields, which would likely arise from different formation processes. Data sources: Black squares (François et al. 2007), red triangles (Honda et al. 2004), blue open squares (Johnson & Bolte 2002), magenta star (Hill et al. 2002) and green ×'s are based on values from the literature.

to-star scatter of several dex[9] (see Figure 1.6), which makes it very difficult to explain its

Generally, [A/B] = log (N_A/N_B) - log (N_A/N_B)$_\odot$.

[8]This corresponds to the integrated area of the spectral line (Emerson 1996).

[9]The stellar abundances are determined as the logarithm of the number densities, hence the there will be no real unit of the abundances, except for 'dex'.

formation via only one process.
Furthermore, if there were only one process creating so diverging abundances, why would other elements supposedly created by the same process not show similar star-to-star abundance variation?
Among all heavy elements studied to date, only strontium shows a comparably large scatter, which cannot be due to observational or analytical errors. For instance, Andrievsky et al. (2009) looked into NLTE corrections for Ba, and found a slightly smaller scatter, which however remains very significant. Instead, the findings of the large star-to-star scatter have been interpreted as the need for two different formation channels (François et al. 2007). Another interesting aspect is the detection of Ba and Sr at very low metallicities ([Fe/H]< -3.0). Both are considered s-process elements (at solar metallicities, [Fe/H]$= 0$), but there is a time-scale problem here. The s-process is tied to AGB and RGB stars, hence it cannot be efficient in the very early phases of the Galactic evolution ([Fe/H] < -3; when the stars are still evolving to their AGB and RGB stages). Therefore, what we see at these early phases is only r-process syntheses, which implies that both Sr and Ba should be considered r-process elements in the early Galaxy (Burris et al. 2000). The Sr and Ba abundance scatter should be related to the r-process, possibly to the two different r-process components already proposed.

Further support to the need for two r-process channels comes from the elemental anti-correlations found by François et al. (2007) when comparing Sr, Y and Zr abundances to Ba. A second r-process, or need for another primary process, seems to be implied by most, if not all, recent theoretical studies, despite the variety of scenarios investigated:
Wanajo et al. (2003, 2010), a weak r-process from low mass O-Ne-Mg SN
Montes et al. (2007), a light element primary process proposed without direct site connection
Farouqi et al. (2009), a weak r-process from high entropy winds

Efficient instruments and large telescopes, however, should not take full credit. The major break-through in the studies of neutron-capture elements is the discovery of the (very rare) r-process enhanced stars.

Sneden et al. (1994) were the first to find and analyse the very r-process enhanced star CS 22892-052 (an enhancement factor of more than 10 in all its heavy elements, compared to stars of similar stellar parameters). The large overabundance of its r-process elements opened the door to the analysis of relatively unstudied heavy elements, such as La, Ce, Nd, Sm, Eu, Gd, Dy and Er at a [Fe/H] $<$ -3 dex. Until this discovery, most studies of neutron-capture elements had focused on the analysis of Sr, Y, Zr, Ba and Eu Gilroy et al. (1988), Ryan et al. (1991), Primas et al. (1994), and McWilliam et al. (1995). As more and higher quality spectra were collected for this star, Sneden and collaborators were able to detect more and more 'exotic' heavy elements. Thorium and uranium abundances were then also derived in the second r-process enhanced star (CS 31082-001, Hill et al. 2002) discovered with UVES at VLT. In these years, the importance of the Th/Eu ratio and the U/Th ratio were discovered to be important for radioactively dating the age of a star (Cowan et al. 1999; Cowan & Sneden 2006).

Both these stars came from the HK objective prism survey of Beers et al. (1985, 1992) where they searched for metal-poor stars using the Ca H and K lines, hence the survey name, as metallicity indicators. These time consuming searches resulted in a very large sample of metal-poor stars, which became the first large metal-poor stellar sample known in the early - mid 1990's. These were also the years where a different extra-galactic survey was being carried out, the Hamburg-ESO survey (HES, Wisotzki et al. 1996), from which Christlieb et al. (2001a) and Christlieb et al. (2001b) extracted the stellar content. Among the various follow-up projects of the HES, the most relevant for this study is the Hamburg/ESO R-process Enhanced Star (HERES) survey aimed at searching for metal-poor r-process enhanced stars (Christlieb et al. 2004). This is to date the largest r-process enhanced star survey covering 373 (giant) stars below [Fe/H]= -2.5 (Barklem et al. 2005). All spectra were obtained at moderate resolution, with short (snapshots) exposures giving a relatively low S/N of around 30 at 4100 Å (Christlieb et al. 2004). Because of the large number of spectra that were obtained these were semi-automatically analysed and up to 10 different neutron-capture elements were measured ranging from Sr to Th (but not including Pd or Ag). Their study defined two different classes of r-process enhancements based on the [Eu/Fe] and [Ba/Eu] abundance ratios: The r-I class is characterised by 0.3 $\leq$ [Eu/Fe] $\leq$ 1.0 and [Ba/Eu] $\leq$ 0; the second r-II class is identified by [Eu/Fe] $>$ 1.0 and [Ba/Eu] $<$ 0. The main goal of their survey was to discover more r-II stars, to derive the halo metallicity distribution as well as characterize the scatter among the studied elements, which was indeed found in the abundance ratios of light to heavy neutron-capture elements. Barklem et al. (2005) also confirmed what had already been found by Hill et al. (2002), but not by Sneden et al. (2000), namely that the lighter n-capture elements were deviating from the solar scaled (SS) r-process ratio[10]. For the rest of the heavy elements, the SS r-process ratio provided a good fit. Barklem et al. (2005) found eight r-II stars, all in the [Fe/H] interval -3.2 to -2.6 dex, making such a strong Eu enhancement rare.

Focusing on the scatter of the light n-capture elements, Barklem et al. (2005) obtained an increasing scatter with decreasing metallicity below [Fe/H] = -2.5, whereas above this value the scatter is much lower, indicating that the Galactic halo is better mixed/homogenized. Interestingly, [Fe/H] $\sim$ -2.5 is also the metallicity at which Burris et al. (2000) found the s-process to set in. However, if confirmed this would mean that differences in r-process trends are expected to be most prominent below [Fe/H] = -2.5. Lai et al. (2008), based on a high resolution, high signal-to-noise abundance study of 28 metal-poor stars concluded, that the early interstellar medium must have been well mixed since very low scatter is present in the iron-peak elements. Furthermore, they found that below [Ba/H] = -5.0[11] the Ba abundances correlate with [Sr/H], and interpreted this as a common origin of the neutron-capture elements in so-called hyper neutron-capture poor stars and that the second r-process sets in only above [Ba/H] = -5.0. Hence, the mixing of the ISM is still under debate. The next question arises:

[10]This ratio is derived from predicted amounts of s-process abundances in the Sun and then scaled to the metallicity of the star under study.

[11]obtained for six stars originating from different literature studies

– When does the second r-process set in or do the two r-process co-exist even at the lowest metallicities?

A larger sample than presented by Lai et al. (2008) is needed to answer these questions (see Chapter 5). Another indication of a second r-process taking place at the lower metallicities can be seen from stellar abundances of neutron-capture elements when comparing these to Solar System (SS) scaled r-process predictions (see Figure 1.7). Only few stars

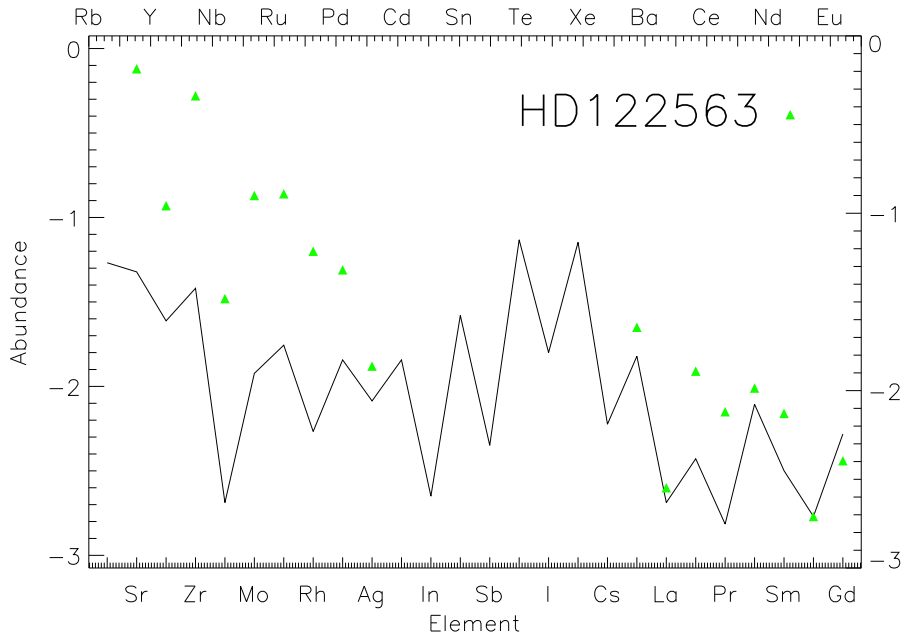

Figure 1.7: The solar system scaled r-process predictions based on Burris et al. (2000) shown as the jagged line compared to observationally derived abundances of HD122563 (green triangles) (Honda et al. 2006). HD122563 is known as the prototype type star indicating the presence of a second primary process, however, several other very metal-poor ([Fe/H] $<\sim$ -3) stars also show similar patterns, especially HD88609 (as well as many HERES stars: HE1320-1339, HE2347-1334, HE0051-2304 and HE1225+0155 just to mention a few).

have been studied in detail yielding more than 25 neutron-capture element abundances. Some of these stars indicate the presence of a second r-process creating the lighter of the elements beyond the iron-peak in the Periodic Table. This was most recently confirmed by Cowan et al. 2010 in press. One of these stars is HD122563 showing 17 neutron-capture elements in Figure 1.7. Of these 17 elements only the lighter lie above the jagged SS r-process line. More stars have the same abundances pattern, some of these are listed in the figure caption, however, these stars have not been studied in the same detail as e.g. HD122563 and HD88609 (Honda et al. 2006).

Figure 1.7 shows that the heavier elements around Eu follow the SS curve relatively well, whereas the elements from strontium to silver ($38 < Z < 47$)[12] all lie above this scaled r-process curve, implying a relative excess of these elements compared to the SS scaled values. This indicates that a second r-process could be at play, creating this excess of the lighter r-process elements.

Yet another study presenting Sr, Y, Zr and this time also a few derivations of Pd and Ag abundances in metal-poor stars is that of Johnson & Bolte (2002). They report large deviations from the SS r-process line of these elements, whereas the even heavier elements as Ba and Eu fit the SS r-process prediction. They detect a large scatter for [Y/Ba] and [Pd/Ag]. Since the stars showing these trends are metal-poor they disregard both the main and the weak s-process as a possible explanation for the scatter. The authors loosely suggest that the large scatter and the odd-even effect around Pd and Ag, could be due to the variety of suggested r-process sites. Comparisons to e.g Johnson & Bolte (2002) and comments on abundance trends, scatter and odd-even effects of Pd and Ag will be made in Chapter 5.

1.5 Why study palladium and silver?

Elements in the range $38 < Z < 47$ are of great interest since these elements can reveal key information on the existence of a second primary process (Montes et al. 2007), since this range contains relatively light elements for which the r-process contribution is dominating the heavy part of this range (Sr: 15%, Y: 8%, Zr: 17%, Nb: 15%, Mo: $<\sim$ 50%, Ru: 68%, Rh: 86%, Pd: 54% and Ag: 80%; Arlandini et al.) and hence Ru, Rh, Pd and Ag are good candidate elements. However, a high r-process fraction is not the only factor to take into consideration when selecting the target elements. So far elements like Sr, Y, Zr and Ba have been studied in greater detail, since they have stronger lines that are easily detected, even in lower S/N spectra, however these elements seem more sensitive to other process contributions (see also Chapter 5). The lines of Pd and Ag are difficult but possible to study (see Figure 1.5), and they fall within a range of 120 Å, which allows a very detailed analysis of both elements. Since their lines are so close, the abundances will most likely be exposed to the same problems and corrections, and these might cancel in the relative abundance ratios of Ag and Pd. Furthermore, of the remaining elements in this interval, silver and palladium have only been subject to very few and limited studies. Silver was studied by six groups (Crawford et al. 1998; Johnson & Bolte 2002; Cowan et al. 2002; Hill et al. 2002; Sneden et al. 2003; Honda et al. 2006) four of which only studied one star each, while Crawford et al. (1998) detected silver in seven stars, and Johnson & Bolte (2002) determined Ag upper limits in three stars. All in all, a low number of Ag derivations, statistically speaking.

The situation of palladium is very similar. Johnson & Bolte (2002) analysed palladium in 12 stars, but for nine of them they were able to derive only upper limits. The 'single star' studies, mentioned above, also derived Pd in the stars. Yet, the overall sample of

[12] Z is the atomic number

stars with known Ag and Pd abundances remain small ($<\sim$ 20). Since Ag and Pd carry important clues on a possible second r-process, and have been scarcely studied, I chose to study Pd and Ag in a large sample of metal-poor dwarf and giant stars to trace the second r-process. From this sample I gained key information on the second r-process, and I also included abundances of Sr, Y, Zr, Ba and Eu, so that all these abundances can be compared to each other. All these elements have known formation processes at solar metallicity. Therefore, if Pd or Ag were to correlate with either of these elements it should be possible to constrain the underlying process and physics, which must be the same. At solar (and sub-solar, [Fe/H] $\sim>$-2) metallicity, Sr and Y (and to some extent Zr) are weak s-process elements, whereas Ba is a main s-process element. Eu, on the other hand, is a main r-process element at all metallicities (Arlandini et al. 1999). As already mentioned, there seems to be different observational trends and behaviours characterizing light and heavy neutron-capture elements (Johnson & Bolte 2002; François et al. 2007), which strengthen the need to compare Pd and Ag to both the lighter (Sr - Zr) and the heavier (Ba and Eu) elements.

The abundance comparisons yielded important constraints of the formation process of Pd and Ag (see Chapter 5). Furthermore, the derived abundances compared to various model predictions, allowed a discussion on the formation site (cf. Chapter 6).

1.6 A bigger picture

Looking beyond stellar spectra and the chemical history of our Galaxy, I will now end this introductory chapter with an expanded view on the multiple applications and basic curiosities about the elements studied here.

The applications of palladium and silver (see Figure 1.8) are numerous: Both metals belong to a small group of four elements (palladium, silver, gold and platinum) that are used in currencies[13], and both are important metals for jewellery, photography and dentistry. Palladium is used in everything from LCD TVs to capacitors and chemical catalysts. Furthermore, Pd has the ability to absorb hydrogen (Hammond (2004)) which allowed the Fleishmann-Pons experiment[14]. Its radioactive isotopes ^{103}Pd and ^{109}Pd are both used in cancer treatments[15], whereas the ^{106}Pd isotope is the most stable nuclei (one of the six naturally occurring isotopes) and ^{107}Pd β^--decays over time to ^{107}Ag.
Several radioactive silver isotopes will β^--decay to cadmium. Silver has the highest conductivity of all metals, it is a good reflector (therefore used in glasses), and furthermore in its Ag^+ form also has antibacterial and antibiotic effects, hence it is used by the pharmaceutical industry. In 1922 a silver beam was sent through a magnetic field in the Stern-Gerlach experiment, which served to study and discover the spin of the electron[16]. Silver was

[13]ISO 4217 currency codes: http://www.iso.org/iso/support/currency_codes_list-1.htm

[14]A very debated cold-fusion experiment from 1989 applying a palladium cathode in deuterium oxide as a sort of calorimeter which might provide the proper energy for cold-fusion

[15]http://www.webelements.com/palladium/isotopes.html

[16]http://hyperphysics.phy-astr.gsu.edu/hbase/spin.html

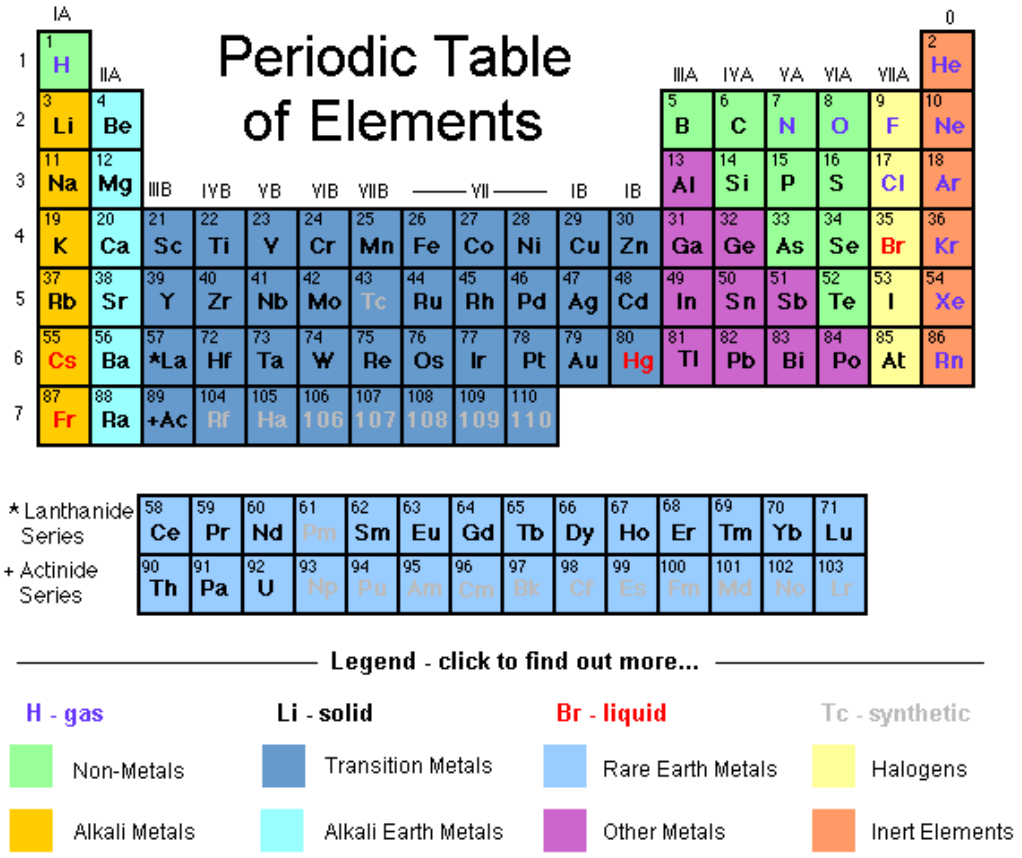

Figure 1.8: The periodic table indicating the position of the heavy elements studied here.

suitable for this study due to its electron configuration with an outer s^1 electron. This represented (discovering the spin of the electron) a step forward in quantum mechanics, which resulted in Otto Stern receiving the Nobel price in 1943[17]. The only two stable isotopes of silver, ^{107}Ag and ^{109}Ag[18], are the ones studied here in the near-UV spectra.

Understanding and tracing where these two elements originated from is interesting and will improve our overall knowledge of the formation and evolution of the heavy elements.

[17] http://nobelprize.org/nobel_prizes/physics/laureates/1943/press.html
[18] http://www.webelements.com/silver/isotopes.html

Chapter 2

Data - Sample and Data Reduction

This chapter describes the assembling of the stellar sample and provides a detailed picture of the most important steps in the data reduction of high-resolution echelle spectra. The sample is comprised of stars at various evolutionary stages (from dwarfs to giants and horizontal branch stars) as well as different metallicities. Additionally the giants cover both chemical normal and chemically r-process enhanced stars.

2.1 Composition of the sample

The sample spans a range in stellar parameters that exceeds 1000 K in temperature, 4 dex in gravity and more than 2.5 dex in metallicity. The dwarf stars were originally observed for a different project, targeting high signal-to-noise (S/N) and spectral resolution in the near-ultraviolet (to determine beryllium abundances Primas 2010) where many other interesting lines are found. Furthermore, the dwarfs were selected so that they span a wide metallicity range. All dwarf spectra were retrieved from the UVES archive[1] and have been reduced with the UVES pipeline version 4.3.0 (for further details see Section 2.2). This reduction gave a very homogeneous high resolution sample with a large S/N typically above 100 in the blue and above 250 in the red wavelength ranges.

The sub-sample of the giants consists of a mixture of UVES/VLT (Dekker et al. 2000) and HIRES/Keck1 (Vogt et al. 1994), which were extracted already reduced from the respective archives. This leads to a slightly less uniform sub-sample, but it still contains stars observed with a very high resolution (R $\sim$ 43.000 - 60.000) and high signal-to-noise (S/N $>$ 100 at 3400 Å). The selection was carried out in such way that the sample spans broadly in metallicity and chemical enrichments, so that also very r-process enhanced stars could be included.

Table 2.1 lists the 73 stars included in my sample, where the colours (V-K) and (b-y) taken from Nissen et al. (2002, 2004, 2007) are listed as some of the known properties of these stars together with my determinations of the [Fe/H], which were included in order to indicate this sample's range in metallicity.

[1] http://archive.eso.org/eso/eso_archive_main.html

Table 2.1: The stars in my sample, their colours and my determinations of their [Fe/H] are listed in this table.

Dwarfs	V-K	b-y	[Fe/H]	Giants	V-K	b-y	[Fe/H]
BD+092190	1.240	0.307	-2.60	BD-012916	1.280		-1.99
BD-133442	1.270	0.308	-2.56	BD+82856	0.000		-2.09
CD-3018140	1.294	0.323	-1.92	BD+302611	3.040		-1.20
CD-333337	1.418	0.334	-1.55	BD+42621	0.740		-2.48
CD-453283	1.594	0.384	-0.99	BD+541323	1.970		-1.64
CD-571633	1.438	0.343	-1.01	CS22890-024	1.970		-2.77
HD3567	1.366	0.332	-1.33	CS29512-073	1.410		-2.67
HD19445	1.413	0.352	-2.13	CS30312-100	2.170		-2.62
HD22879	1.508	0.370	-0.95	CS30312-059	2.440		-3.06
HD25704	1.567	0.371	-1.12	CS31082-001	2.210		-2.81
HD63077	1.612	0.365	-1.05	HD74462	2.640		-1.48
HD63598	1.579	0.358	-0.99	HD83212	2.720	0.658	-1.25
HD76932	1.439	0.354	-0.97	HD88609	2.580		-2.87
HD103723	1.410	0.356	-0.85	HD108317	1.880	0.439	-2.11
HD105004	1.446	0.387	-0.84	HD110184	2.920		-2.40
HD106038	1.418	0.342	-1.48	HD115444	2.350		-3.00
HD111980	1.598	0.369	-1.31	HD122563	2.470	0.639	-2.81
HD113679	1.594	0.403	-0.63	HD122956	1.350	0.668	-1.45
HD116064	1.501	0.349	-2.19	HD126238	2.320		-1.92
HD120559	1.774	0.424	-1.33	HD126587	2.442		-3.16
HD121004	1.605	0.395	-0.73	HD128279	0.900	0.466	-2.34
HD122196	1.455	0.343	-1.81	HD165195	3.200	0.919	-2.10
HD126681	1.669	0.400	-1.28	HD166161	2.780		-1.25
HD132475	1.643	0.401	-1.52	HD175305	2.120	0.488	-1.38
HD140283	1.625	0.380	-2.58	HD186478	2.700		-2.42
HD160617	1.422	0.347	-1.83	HD204543	2.500	0.635	-1.84
HD166913	1.310	0.327	-1.30	HE0315+0000	2.320		-2.59
HD175179	1.529	0.384	-0.72	HE0442-1234	2.950		-2.32
HD188510	1.709	0.416	-1.58	HE1219-0312	2.050		-3.21
HD189558	1.571	0.386	-1.18	RR Lyrae			
HD195633	1.446	0.361	-0.71	CS 22881-039			-2.75
HD205650	1.479	0.375	-1.19	CS 30317-056			-2.85
HD213657	1.312	0.322	-2.01				
HD298986	1.307	0.324	-1.48				
G005-040	1.624	0.402	-0.93				
G013-009	1.259	0.311	-2.27				
G020-024	1.460	0.362	-1.89				
G064-012	1.250	0.307	-3.10				
G064-037	1.221	0.300	-3.17				
G088-032	1.239	0.311	-2.50				
G088-040	1.424	0.351	-0.90				
G183-011	1.258	0.319	-2.12				

Figure 2.1 illustrates the distribution of this sample's stars in a log T, log g diagram. The actual determination of the temperature and gravity will be described in Chapter 3 and 4.

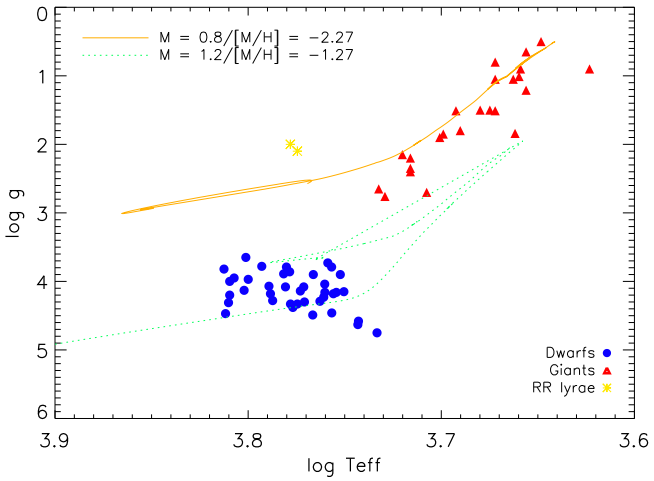

Figure 2.1: This figure shows how the sample stars are distributed in a log temperature versus log gravity diagram. Two isochrones with different masses and metallicities are shown to illustrate the variation in parameters of this sample. Giants are shown as filled red triangles, dwarfs as filled blue circles and the RR lyrae as yellow asterisks.

2.1.1 Sample biases

Even though the sample was put together carefully in order to avoid biases, some selection biases will always be present, as we see in Chapter 4. Silver and palladium are seen only in giant stars at low metallicities, therefore this will introduce a bias. Similarly for the r-process enriched stars, where only one metal-poor ([Fe/H] $<$ -3 dex) r-process enhanced dwarf is known to date, implying that all selected r-process enhanced metal-poor stars are giants. The latter is an observational bias which will remain for a while, and despite chemical enrichment, my sample of stars with known silver abundances will be biased towards giants. Therefore it is important to see if giants and dwarfs show the same abundance trends in the metallicity range where they overlap, and to test how much this bias affects the final conclusions. Generally, stars with low gravities and metallicities are subject to LTE deviations especially lines with low excitation transitions (Asplund 2005) as considered for Ag and Pd, therefore a comparison of dwarf and giant stars will allow an assessment of the severity of e.g. NLTE effect in the giants compared to the less affected dwarf stars. To ensure that the obtained Pd and Ag abundance trends are purely tracers of the formation processes, and not due to biases or effects from e.g. the effective temperature, they were compared to the stellar parameters of all stars (see Section

5.2). Lai et al. (2008) found such abundance - temperature relations for Si, Cr and Ti, and therefore these abundances should not be trusted as chemical tracers (not those determined in their analysis).

2.2 Data reduction

The UVES data have been reduced using both the most recent UVES pipeline (v. 4.3.0) and interactively with IRAF[2], in order to test the output quality of the semi automatic reductions. UVES is a cross-dispersed high-resolution echelle spectrograph mounted on the Nasmyth focus of the VLT2/Kueyen telescope at Paranal in Chile. A typical fake coloured raw echelle frame is shown in Figure 2.2. Each order is seen as horizontal coloured lines and the absorption lines are the vertical black lines. With two arms and a beam splitter, UVES can cover both the very blue part of the spectrum (from 3000 Å) as well as the redder parts, reaching up to 11000 Å. When applying a one arc second slit UVES has a resolving power of R $\sim$ 40.000. This is exactly the kind of instrument needed to observe near ultraviolet (near-UV) lines at high-resolution in high signal-to-noise spectra. There are two main ESO tools to carry out the data reduction, Gasgano[3] and EsoRex[4]. Gasgano is a graphical interface that classifies all frames (science, flat, bias and arc frames) and allows the user to directly mark the files needed to carry out a partial or full reduction. In order to apply EsoRex, a non-graphical recipe execution tool, the files must first be classified (manually) but afterwards all the files will be reduced in batch mode making it straight forward to test the reductions and reduce the files again. EsoRex v. 3.6.8 was for latter mentioned reasons chosen. For the record the most recent publicly available ESO data reduction work bench is called Reflex[5] which is the successor of EsoRex.

2.2.1 From raw to reduced spectra

First I will mention the reduction steps that needs to be taken in chronological order. The raw science frame (similar to Figure 2.2) needs to be bias subtracted, have cosmic rays removed, orders recognized, background subtracted, flat field corrected and wavelength calibrated. Finally the spectrum will be extracted and the orders merged. When the pipeline is applied, all intermediate steps will be saved separately, and spectra with orders not merged will be available as well. To carry out such a reduction the following files are needed: biases, flat fields, an arc file (from the Thorium-Argon lamp in this case) and an object (science) file.

Here the IRAF reduction will be described in detail. In order to avoid extreme counts and errors that might occur in single frames, every science frame (meaning every exposure

[2]IRAF is distributed by the National Optical Astronomy Observatory, which is operated by the Association of Universities of Research in Astronomy, Inc., under contract with the National Science Foundation.

[3]http://www.eso.org/sci/software/gasgano/

[4]http://www.eso.org/sci/data-processing/software/cpl/esorex.html

[5]http://www.eso.org/sci/software/sampo/reflex/documents.html

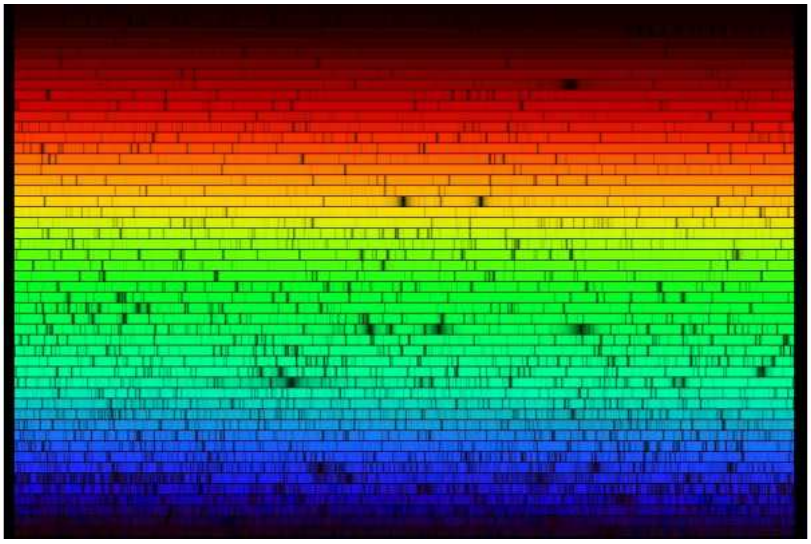

Figure 2.2: An echelle frame. The colours indicate the wavelengths ranging from blue (near-UV) through visual (green/yellow) to the red parts of the spectrum. The vertical black lines are absorption lines, which via data reduction will turn into the 1D absorption spectra (see Figure 2.5). The thicker the black lines are, the stronger the absorption lines are.

of the observed star) is corrected by several bias and flat field frames (see Figure 2.3), which have been combined into a single master bias and a master flat field frame, respectively.

This co-addition was done in two different ways to select the best method. I tested averaging versus median combination. The median would a priori be preferred since it automatically discards pixels with very high or low counts from the master file. However, the median master files showed picket fence pattern which is not physical, but artefacts of the reduction. Hence, the files were averaged, and in order to avoid having extreme counts in the master bias file, I applied sigma clipping[6] (I selected three sigma). This cuts out pixels deviating with more or less than three sigma. In this procedure the cosmic ray hits are removed from the master bias. This approach resulted in a reduced bias frame (see first panel of Figure 2.3) with a slight jagged pattern around the average counts per pixel.

A bad pixel map was then created to remove bad pixels and/or bad columns. This map simply contains the coordinates of the pixels/regions that should be ignored.

The master flat was then created. First, each single flat was master bias subtracted and had all bad pixels removed. All the flat frames were combined using an average algorithm, rejecting pixels deviating more than three sigma as well as cosmic rays. Then the flat frame needs to be normalised. In order to do so, one needs to trace and specify where the orders lie and how broad they are, so that the sensitivity of the pixels in the orders and not in the inter-orders can be corrected later on.

[6]Removing points that deviate more than a certain number of sigma from the mean value.

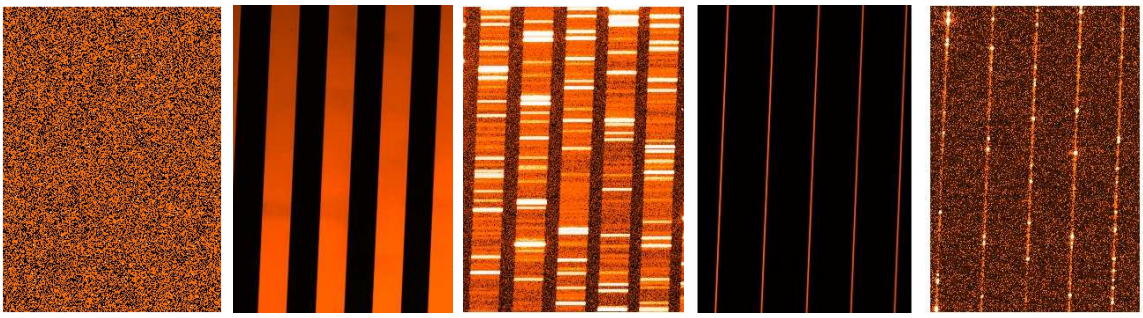

Figure 2.3: Parts of five 2D calibration frames are shown here. From the left: Bias, flat, wavelength calibration, format check file and order defining file.

Once the flat field is normalised, all remaining files, i.e. the arc files and the science files can be bias subtracted, bad pixel and cosmic ray corrected, as well as divided by the normalised flat.
As for the master flat field we now have to trace and extract the orders, also for the science and the arc files, by centring the orders and specifying their width and total number present on the CCD. At this stage we are still dealing with 2D images as shown in Figure 2.3. Furthermore, the science frames need to have any background residual properly subtracted, which is done by identifying and specifying the order/inter-order regions. The definition of order versus inter-order/background is very important for the final signal-to-noise ratio of the science spectrum. If the orders are defined too narrow the flux of the inter-orders will be too high, and this will result in a lower S/N spectrum. On the other hand, if the orders are defined too broad the flux of the inter-orders/background will be very low, thus leaving extra noise in the spectra, again leading to a lower S/N spectrum. Once the background is subtracted, we can extract the orders.

The next step is to move from a pixel scale to a wavelength scale. This is a rather time consuming part of the reduction, since a manual identification of at least two lines in each echelle order is recommended, well sampling the beginning and the end of the orders. This identification is performed on the arc frame (including thorium and argon emission lines), where the marked recognized lines are assigned the correct wavelengths (part of an echelle order is shown in Figure 2.4) and then applied to the science file.

The orders can now be merged, and following a radial velocity shift needs to be applied to the merged spectra, bringing them to the same rest frame (for further details see section 2.3.1). Once all spectral lines are shifted to the rest frame, exposures of the same object can be added into a 'master' object. Adding the frames this way increases the signal-to-noise ratio. Finally the merged, shifted and added spectra are normalised, i.e. the continuum flux is forced to unity. In IRAF a pseudo-continuum with a polynomial is fitted by specifying the polynomial and its order in the 'CONTINUUM' package. After several

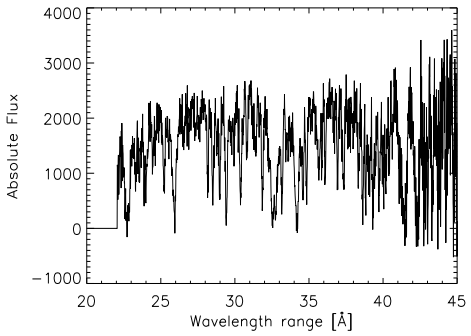

Figure 2.4: Part of a blue order of G 005-040. The x-axis indicates a relative range in Angstrom.

tests, polynomial with a fourth order cubic spline or a sixth order Legendre polynomial turned out to give satisfactory fits to the observed spectra. The Legendre polynomial were only resorted to, if the cubic spline provided bad fits or left strong polynomial trends in the normalised observed spectra. An example can be seen in Figure 2.5. Such trends can be completely removed by applying much higher polynomial orders or by normalising with more interactive routines, where the user can set the continuum points to be forced to unity. Either way, each spectral region has always been carefully inspected before synthesizing spectra or fitting profiles to obtain the equivalent widths.

2.2.2 IRAF versus UVES pipeline

All the steps described in the previous section are common to any data reduction of an echelle frame. The main difference between the standard, manual reduction and the usage of an automated pipeline is that the latter must rely on a specific "instrument physical model" in which all instrument characteristics must have been recorded. In the specifics of the UVES pipeline, the major difference with respect to the manual reduction I have performed with IRAF, is that it uses two extra calibration files. These are taken by default by the ESO observatory, when observing with UVES. The files are the so-called order definition file and the format check file (see the last two panels in Figure 2.3). The former is basically a frame with a continuum flat lamp, gained with a narrow (0.5") slit and it is used to automatically find the central position of all echelle orders and of the inter-order background. The latter set of files are obtained with a thorium-argon wavelength calibration lamp, again with the narrow slit. Furthermore, the pipeline includes also the flux calibration of the science frames, via the usage of a standard star exposure, also part of the ESO calibration plan.

The resulting spectra of a manual reduction are similar to the UVES pipeline products. Reduction steps like order merging are carried out better in the manual IRAF reduction, however a manual reduction of several hundred spectra would be too time consuming,

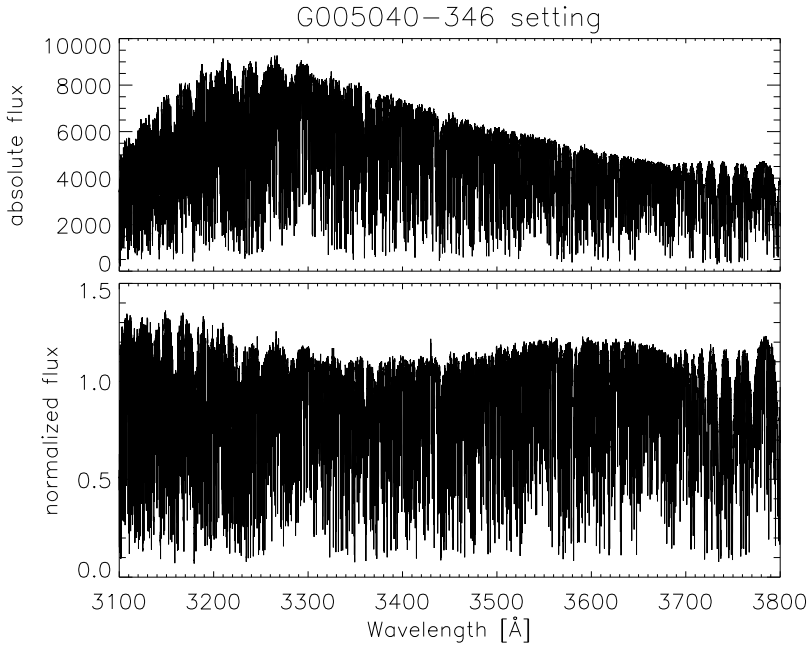

Figure 2.5: Top: A reduced blue spectrum of G 005-040 showing a clear Planck spectrum. Bottom: A continuum normalised spectrum of the same star, with weak imprints of the fitted polynomial.

and therefore the UVES pipeline reduction was chosen. Special attention was paid to the resulting order merging.

2.3 Merging

Each echelle order is about 50/100 Å long in the blue/red UVES spectra. The extraction of the science spectra is carried out order by order. One then has the choice to work with separate orders (30 - 35 full orders per spectrum depending on the setting) or to merge the orders into a single spectrum. This is a rather delicate step, as merging algorithms are notoriously not very robust, and their performance depend strongly on the data. When echelle orders are improperly merged a repeated bumpy pattern is introduced. The overlapping, merged regions result in an artificially lower flux level (see Figure 2.6 where repeated bumps are indicated by arrows.) The UVES pipeline available in 2007 did not provide an optimized order merging. Therefore several of the reduced UVES spectra in the ESO archive (http://archive.eso.org/eso/eso_archive_adp.html) were affected by this bumpy pattern (see Figure 2.6). This clearly has a significant impact on the placement of the continuum and the derivation of abundances, especially for the elements with lines falling exactly where the orders are merged. This was seen for the majority of this sample's stellar spectra. The blue silver line falls exactly in the overlapping region of two consecutive order, which led to the re-reduction of all the dwarf spectra. This is why we had

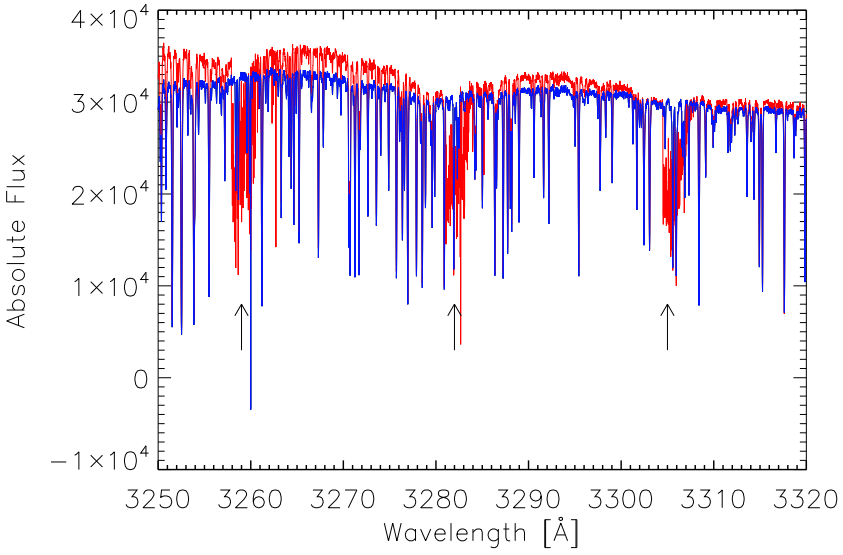

Figure 2.6: Arrows indicate the merging problems around 3255, 3280 and 3305 Å in the spectrum of HD122196 obtained with the pipeline from 2007 (red spectrum), whereas the newly reduced (applying UVES pipeline version 4.3.0) spectrum of HD122196 is over plotted in blue.

to resort to a manual IRAF-based reduction. In the meantime, a new, improved UVES pipeline was released (v. 4.3.0), which included a much more robust merging algorithm, and yielded satisfactory merged spectra.

2.3.1 Radial velocity shift

There are two main methods of carrying out the radial velocity shift. One option is to identify the lines, determine and apply the average shift to the spectra. This can be accomplished in IRAF by applying the 'RVIDLINES' followed by the 'DOPCOR' packages. The former package identifies spectral lines by the use of a line list[7] with known rest wavelengths, and calculates the shifts needed to bring the spectral lines to the rest wavelength. The latter package applies the shift to the lines.

Another method is to carry out a cross-correlation with a template spectrum in the rest frame. In IRAF one cross-correlating package is 'FXCOR', which predicts the necessary shift (by fitting Gaussian profiles and Fourier transforming) in order to bring the lines of the not shifted spectra to the rest wavelength of the corresponding template lines. Again the actual shift would be applied by using 'DOPCOR'.

[7]One should avoid strong lines since these introduce uncertainties in the final radial velocity and spectrum shift.

I applied the cross-correlating method since I have a large sample of stars with many individual spectra per star. The template must have a well known radial velocity and be accurately shifted to the rest frame. In order to obtain the best possible cross-correlation, the template needs to be similar to the non shifted spectra. This means that it is not wise to apply the same template for metal-poor and metal-rich stars. There is also a difference between dwarfs and giants. Due to the span in my data sample, I selected four templates, i.e. for the dwarfs and the giants, one metal-poor and metal-rich template each. For each of these four templates several lines were identified with 'RVIDLINES' and then these spectra were shifted and carefully inspected before these were accepted as templates. The resulting radial velocities ([km/s]) are accurate to the first decimal.

The radial velocities derived directly from line recognition or cross-correlation is the geocentric radial velocity. Generally speaking, the stellar radial velocities are a measurement of the Doppler shift of the star with respect to the observer, who is positioned in a moving rotating geocentric reference system centred on Earth. This velocity can be converted from our geocentric reference system, e.g. to the heliocentric reference system centred on the Sun. These velocities are called heliocentric radial velocities, and are computed from the geocentric radial velocities by adding the heliocentric correction. This conversion corrects the imprint of the relative motion, which the Earth introduced in the geocentric radial velocity. Furthermore, transferring all observationally determined radial velocities to the heliocentric reference system eases comparisons of radial velocities. Similarly, the so-called barycentric radial velocity (the centre of mass of the solar system) (Nidever et al. 2002) can be calculated from the geocentric velocity, by adding the barycentric correction. These radial velocities are the most 'absolute' velocities of the three mentioned, and are mainly used for extra-galactic radial velocities.

A positive radial velocity is obtained from redshifted spectral lines.

Chapter 3

Stellar Parameters

In order to derive stellar abundances we first need to know the stellar atmosphere parameters, namely temperature, gravity, [Fe/H] and microturbulence velocity. These are fed to the synthetic spectrum code together with the stellar model atmospheres. Since the main purpose of this work is to understand the chemical evolution of elements like silver and palladium, and obtain as much information as possible on their formation process, a homogeneous analysis of the sample is very important. Trends and offsets in stellar parameters propagate into uncertainties on the final abundances. Therefore all stellar parameters have been carefully determined and tested. The analysis has been carried out with 1D local thermodynamic equilibrium (LTE) models and codes. Even though some 3D models exists and NLTE abundance corrections are available for several elements, this is unfortunately not the case for the majority of the very heavy elements considered here. MARCS model atmospheres[1] (Gustafsson et al. 2008) have been used in this analysis and have been interpolated using the code written by Masseron (2006). MOOG (Sneden 1973) synthetic spectrum code was applied to derive the abundances as well as stellar parameters.

3.1 Methods for determining stellar parameters

We derived the stellar parameters for most of the sample stars via: colour-$T_{\rm eff}$ calibrations for the effective temperatures (Alonso et al. 1996b, 1999), Hipparcos parallaxes for the gravities, and equivalent width measurements of Fe I lines for the metallicity (too few Fe II lines could be detected in the most metal-poor stars). For those stars missing photometry or having uncertain reddening values, E(B-V), we had to resort to excitation temperatures, whereas for those stars with inaccurate parallaxes, we had to constrain their gravities via the ionization balance. The microturbulence velocity was constrained by requiring that all Fe I lines give the same abundance, irrespective of their strength (see also Jofré et al. 2010).

[1] www.marcs.astro.uu.se/

3.2 Temperature

The temperature is the parameter with the largest influence on the silver and palladium abundances. This parameter is in general seen to affect (0.01 to 0.14 dex depending on the element) the abundances of lighter elements (Cayrel et al. 2004). For silver I found the effect of changing the temperature by 100 K to be slightly larger (0.05 to 0.2 dex). Different colour calibrations from various groups were tested confirming a difference in the temperature scale as is mentioned in Section 3.2.1.

Consistently too high or low temperatures cause offsets in abundances, and in order not to predict too high abundances by adopting a temperature scale that predicts high temperatures, I selected a scale that predicts intermediate temperatures (see Section 3.2.1 and Figure 3.1). This places my determinations of the stellar parameters in the mid range of the stellar parameters compared to other studies. There are several ways to determine the temperature of a star, one method is by fitting synthetic spectra with known temperature to temperature sensitive lines (such as H lines), another method to determine the temperature is via excitation potentials and a third method is to adopt calibrations that relate the star's colour and metallicity to the temperature. Not all methods can be applied to all types of stars. For instance horizontal branch stars, which have anti-symmetric lines making line fitting very difficult, and due to their very blue colour they fall outside the allowed calibration ranges, which leaves the excitation potentials as the only temperature determination method. This method can lead to large uncertainties depending on the accuracy of the excitation potentials of the selected Fe lines. Therefore I chose the most accurate T-colour calibration (as done in high accuracy abundance studies Meléndez et al. (2010)) and supplemented with excitation temperatures only when necessary. There exist several such colour-T calibrations and in order to avoid inhomogeneities and method dependent offsets in the colour calibrations it is important to stick to one calibration.

The colour of a star is sensitive to its temperature and metallicity. Photometry, colour indices and extinction are necessary input for this colour calibration as is the metallicity. Colour-$T_{\rm eff}$ calibrations from Alonso et al. (1996b), Ramírez & Meléndez (2005), Önehag et al. (2009) and Masana et al. (2006) were applied for V,K and Strömgrem photometry. Alonso et al. (1994, 1996b) noted that the V-K colour is a good choice because it is almost insensitive to metallicity and includes infra-red magnitudes which are generally less affected by reddening (less dust absorbed) compared to the visual magnitudes. However, according to L. Casagrande (priv. comm.) this colour calibration is far from being flawless, since it spans over a wide flux range, in which case the Infra Red Flux Method (IRFM) (Alonso et al. 1996a; Casagrande 2008) has difficulties fitting the entire black body curve. A purely infrared colour is preferred, but for our data sample it is not available for all the stars. Therefore, the V-K colour calibration had to be adopted:

$$\begin{aligned} \theta_{eff} &= 0.555 + 0.195(V-K) + 0.013(V-K)^2 - 0.008(V-K)[\mathrm{Fe/H}] \\ &+ 0.009[\mathrm{Fe/H}] - 0.002[\mathrm{Fe/H}]^2 \end{aligned} \quad (3.1)$$

where $\theta_{eff} = 5040/T_{eff}$. This formula is only valid in certain colour and metallicity ranges

(see Alonso et al. 1996b) e.g. $1.1 \leq (V-K) \leq 1.6$ for -1.5 $\geq$ [Fe/H] > -3.5 and the lower limit for (V-K) decreases with increasing metallicity. This agrees with the fact that for a fixed temperature the colour of a star will become more red the more metal-rich it is. The impact the metals have on the colour can be explained by the line blanketing from all the metallic lines. The UV and blue continuum will be reduced and the star will experience a flux distribution to the red wavelengths (Ramírez & Meléndez 2005). In order to apply the colour-$T_{\rm eff}$ formula for the dwarf stars from Alonso et al. (1996b), the colour terms need to be de-reddened and converted to the TCS (The Carlos Sanches Telescope) filter system from which this calibration was derived. Our infra-red magnitudes are taken from 2MASS[2] and the visual magnitudes are from the Johnson-Cousins (Johnson) filter system[3]. Thus, to apply the formulas from Alonso et al. (1996b, 1999) we need to convert the 2MASS to Johnson and then to TCS following Bessell (2005). Ramírez & Meléndez (2005) is on the other hand adjusted to deal directly with 2MASS-Johnson colours so no conversion is needed here. An example of calculating the temperature for a dwarf star is given below. According to Bessell (2005) the K magnitudes can be converted from 2MASS to the Johnson (J) filter system via the following:

$$K_{2MASS} = K_J - 0.04 \tag{3.2}$$

and converting the V-K colour from Johnson to TCS can be carried out via this relation:

$$(V-K)_{TCS} = 0.05 + 0.994(V-K)_J \tag{3.3}$$

The above mentioned filter relation is taken from Alonso et al. (1994) (to keep the calibration as homogeneous as possible) and the two filters are seen to be very similar for this colour. The difference between TCS and Johnson filter system is on average 0.04 magnitudes. This indicates that the filter conversion from Johnson to 2MASS would almost cancel out the conversion from Johnson to TCS. Nissen et al. (2002) note that the error on the V - K colour might be 0.05 mag, similar to the colour difference from the filter conversion, would lead to an error of $\pm$ 50 K in the temperature. I found that a 0.04 mag increase in V - K could lead to a 100 K decrease in temperature for a few of the dwarfs, but generally agree with the estimate from Nissen et al. (2002), and would furthermore only imply a decrease of 30 K for the giants. To limit the errors and uncertainties the filter conversion was implemented.

The reddening has a much larger effect on the temperature than the filter conversion. The values for the reddening have generally been taken from Nissen et al. (2002, 2004, 2007) for the dwarfs and otherwise estimated from the Schlegel dust maps[4] (Schlegel et al. 1998) for the giants. It is well known that these dust maps tend to overestimate the extinction for stars close to the plane, and for a few stars the reddening values E(B - V) had to be rescaled by multiplying with an empirical adjusted factor according to Bonifacio et al.

[2]http://www.ipac.caltech.edu/2mass/

[3]Taken from the General Catalogue of Photometric Data http://obswww.unige.ch/gcpd/gcpd.html

[4]http://spider.ipac.caltech.edu/staff/jarrett/irsa/dust.html

(2000) in order to obtain reasonable temperatures. Figure 3.1 shows the different colour–temperature calibrations, and for e.g. HD298986 a wrong E(B-V) of 0.52 would lead to a too high temperature (10100 K). The value of the temperature is much too high to match the values of F and G stars ($\sim$ 6000 K), and by applying the rescaling of the dereddening the values predicted become acceptable for these types of stars.

$$E(B-V)_{true} = E(B-V)_{Schlegel}, \text{if} \leq 0.1, else \quad 0.1 + 0.65(E(B-V)_{Schlegel} - 0.1) \quad (3.4)$$

Since the derivation of the majority of our stars is based on V - K colours, the reddening needs to be transformed to this colour as well. For consistency the transformation from Alonso et al. (1996b) was chosen:

$$E(V-K) = 2.72 \cdot E(B-V) \quad (3.5)$$

The derived stellar parameters can be found in Table 3.1 and 3.2 for giants and dwarfs, respectively. In these tables an 'a' indicates that the temperature was derived from excitation potentials either because photometry or extinction (E(V-K)) was missing, or because the metallicity or colour fell outside the allowed calibration ranges. For the gravities the 'a' indicates that I did not have parallaxes and therefore had to resort to ionisation balance of Fe I and II to determine log g. The 'b' implies that the stars are r-process enhanced and the 'c' shows that the stellar parameters had their values altered in order to provide flat trends for either temperature, gravity or microturbulent velocities.

3.2.1 Comparing temperature scales

I determined the temperature based on several colour–T_{eff} calibrations, applying two different colours V–K and b–y (Strömgren photometry). The calibrations considered here are based on Masana et al. (2006), Önehag et al. (2009) (only b–y)), Alonso et al. (1996b), Alonso et al. (1999), Ramírez & Meléndez (2005) and Casagrande et al. (2010) (combined with L. Casagrande priv. comm.). The derived temperatures based on these studies scale slightly different between the dwarfs and giants, and they will therefore be discussed separately. Generally the Strömgren photometry for the dwarfs predicts higher temperatures than the V–K colour. The difference between the five mentioned colour calibration studies can span several hundreds of Kelvin, but can in other cases all agree within $\sim$ 50 K (see Figure 3.1). The studies tend to predict temperatures, where Casagrande et al. (2010) yield the lowest values and Önehag et al. (2009) and Ramírez & Meléndez (2005) the highest. All the temperature predictions are mentioned in increasing order for the more metal-rich stars as well as shown in Figure 3.1:
Casagrande et al. (2010), Masana et al. (2006), Alonso et al. (1996b), Ramírez & Meléndez (2005) and Önehag et al. (2009)
However, for the very metal-poor stars the studies predict different temperatures (starting with the lowest temperature and ending with the highest):
Alonso et al. (1996b), Masana et al. (2006), Casagrande et al. (2010), Önehag et al. (2009),

Ramírez & Meléndez (2005).

The predicted temperatures of Alonso et al. (1996b) and Masana et al. (2006) generally

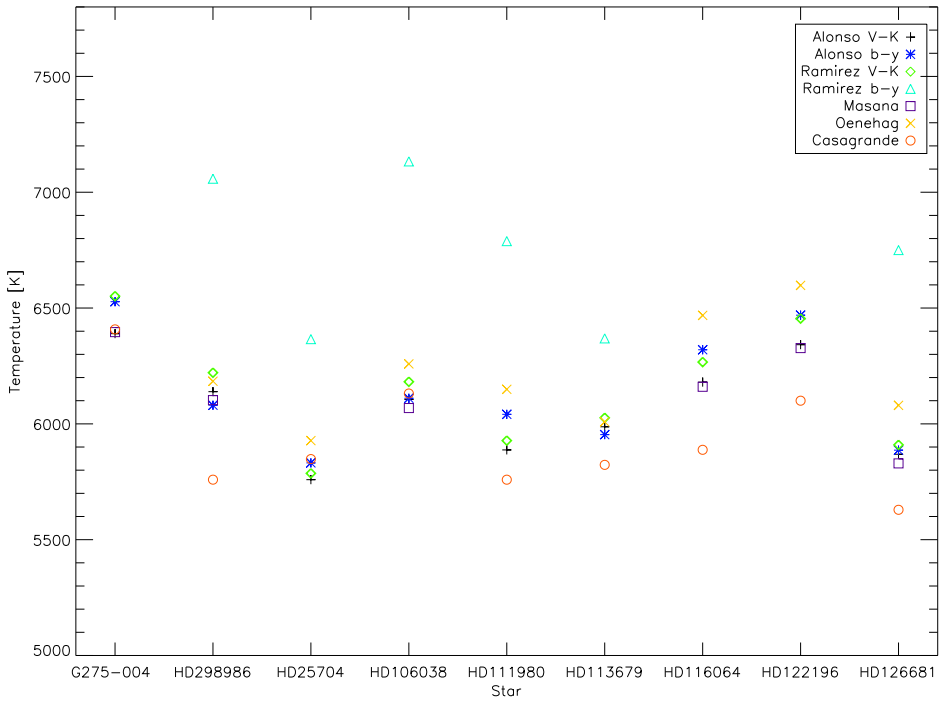

Figure 3.1: Temperatures for nine stars calculated with formulas from five different studies (as indicated in the figure legend). Alonso et al. (1996b) is seen to predict temperatures located in the middle of the temperature range for the more metal-rich stars ([Fe/H]>-2.0) and yields temperatures in the lower parts of the range for stars with lower metallicity. Generally, the b-y (Strömgren colour) predicts a higher temperature than V-K does.

agree, often within 30 - 40 K, whereas the derived temperatures from Strömgren photometry from Alonso et al. (1996b) and Önehag et al. (2009) are higher and agree within 100 - 150 K. The temperatures derived from Ramírez & Meléndez (2005) are always in the high end of the temperature range. The temperatures provided by L. Casagrande (Casagrande et al. 2010) can deviate by 240 K compared to the values derived by Alonso et al. (1996b), but are mainly 100 - 140 K lower than the temperatures derived using their calibrations. This changes for the most metal-poor stars where the temperatures from Casagrande can be 30 - 140 K higher than those derived by the use of calibrations from Alonso et al. (1996b) (see Figure 3.1).

The overall view of these calibrations is that the temperature estimates based on the calibrations from Alonso et al. (1996b) tend to be around the mid range of the estimated temperatures, which was another reason to select these calibrations despite not being the most recent ones. Additionally, Nissen et al. (2007) showed the excellent agreement

of the temperatures derived by H_β line fitting and temperatures derived by T_{eff}–colour calibration using the V–K colour (Alonso et al. 1996b), supporting my choice of this colour–T_{eff} calibration.

For the giants, calibrations from Alonso et al. (1999) tend to predict lower temperatures than those from Ramírez & Meléndez (2005). There are several cases however, where temperatures derived based on the calibrations from Önehag et al. (2009) are lower than the Strömgren colour calibrations from both Ramírez & Meléndez (2005) and Alonso et al. (1999), and where the temperatures derived from the V–K calibrations from Alonso et al. (1999) are higher than the temperatures derived from the V–K colour calibrations from Ramírez & Meléndez (2005). Generally the temperatures derived from my samples giants agree within 80 - 150 K when derived from T_{eff}–(V–K) calibration from Alonso et al. (1999) and Ramírez & Meléndez (2005). To have one consistent temperature scale for both dwarfs and giants, the calibration from Alonso et al. (1999) was chosen for the giants.

3.3 Gravity

If accurate parallaxes were available, the gravity was determined via the parallax – gravity relation (given below). Assuming an absolute V magnitude for the Sun is V = 4.83 (Nissen et al. 1997) and a solar bolometric correction of -0.12, the gravity can be derived from:

$$\log g = \log \frac{M}{M_\odot} + 4 \log \frac{T_{eff}}{T_{eff\odot}} + 0.4V_0 + 0.4BC + 2 \log \pi + 0.12 + \log g_\odot \tag{3.6}$$

and

$$BC = -2.5 \log \frac{\phi}{6.68885 \cdot 10^{-5}} - 0.12 \tag{3.7}$$

where

$$\begin{aligned} \phi &= 2.38619 \cdot 10^{-4} - 1.93659 \cdot 10^{-4}(V-K) + 6.52621 \cdot 10^{-5}(V-K)^2 \\ &- 7.95862 \cdot 10^{-6}(V-K)^3 - 1.01449 \cdot 10^{-5}[\mathrm{Fe/H}] \\ &+ 8.17345 \cdot 10^{-6}(V-K)[\mathrm{Fe/H}] - 2.87876 \cdot 10^{-6}(V-K)^2[\mathrm{Fe/H}] \\ &+ 5.40944 \cdot 10^{-7}(V-K)^3[\mathrm{Fe/H}] \end{aligned} \tag{3.8}$$

These relations (Nissen et al. 1997) connect the parallax (π) to the gravity (log g), via mass (M), temperature (T_{eff}), de-reddened visual magnitude (V_0) and the bolometric correction (BC). The bolometric correction is based on Alonso et al. (1995) for dwarfs and sub-dwarfs and on Alonso et al. (1999) for the giants. The BC formula (3.7) is for dwarfs, and all solar values have been inserted in the expression. The masses were adopted from Nissen et al. (2002, 2004, 2007). If the parallax is accurate, this is a very precise method to derive the gravity, due to its low dependency on Fe I, which can be erroneous due to unknown NLTE effects (Mashonkina et al. 2010), see below. When the parallax or absolute magnitude

were not available this method could not be applied and the gravity was constrained by requiring that Fe I and Fe II give the same iron abundance. The gravity determined from this method was adopted when Fe I and Fe II agreed within 0.1 dex (0.15 dex in a few cases).

3.4 Metallicity

The metallicity was determined from equivalent widths of Fe I lines. This choice was consciously made knowing that Fe I lines are to a larger extent affected by NLTE effects than Fe II lines (Mashonkina et al. 2010, full statistical calculations of all the Fe transitions are difficult to carry out, due to the incompleteness of the model atom where many upper energy levels are missing). However, the exact size of the NLTE abundance correction is not known yet, and for some of our most metal-poor stars it was very difficult to measure accurate equivalent widths of Fe II lines. Barely one or two Fe II lines could be detected in these stars, hence the determination would statistically speaking be very weak. We always have at least five Fe I lines even in the very metal-poor stars, therefore the [Fe/H] was based on Fe I and not Fe II.

It is important to note that in spite of possible NLTE abundance corrections of the Fe I abundances, our metallicities agree with values found in the literature, where some of the metallicities were derived from Fe II. This may indicate that the corrections for our stars may actually be of minor importance. The equivalent widths of the Fe lines were derived using both Daospec[5] and `Fitline` (François et al. 2007). Daospec offers a very automated way to determine the equivalent widths, but has some weaknesses in determining the normalized continuum level in the near-UV. Thus, I resorted to `Fitline`, a semi automatic genetic algorithm, which fits Gaussian profiles to already normalized spectra. The output is wavelength and equivalent width of the lines, which must be provided in the form of an input line list. The Fe abundances were then derived with MOOG.

3.5 Microturbulence velocity, ξ

This parameter was found by requiring all Fe I lines to give the same iron abundance, no matter how large the equivalent widths were, i.e. requiring one consistent abundance value for Fe (metallicity) no matter how strong or weak the line is (see the trend fitted to the Fe abundances in Figure 3.2).

All the above stellar parameters are interdependent. The temperature depends on [Fe/H], gravity on temperature and [Fe/H], while Fe I is temperature and Fe II gravity sensitive. The microturbulence (ξ) depends directly on metallicity. Therefore, if one of the parameters changes, it will affect all the others, and this requires an iterative process, altering the

[5]This research used the facilities of the Canadian Astronomy Data Centre operated by the National Research Council of Canada with the support of the Canadian Space Agency. Version 2004 developed by E. Pancino and P. B. Stetson.

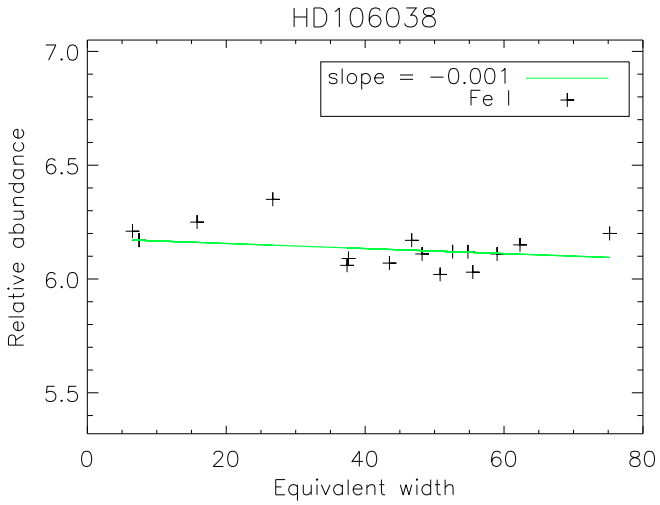

Figure 3.2: The microturbulence is altered until the trend in the above plot is flat. The figure shows relative abundance (in dex) as a function of equivalent width (in milliangstrom) of Fe I lines for HD106038. The slope of the fitted line is given in the legend.

parameters obtained directly from the above mentioned formulas. I iterated these computations until all the parameter changes were found to be negligible (specifics are found in the section below). The reason why the microturbulence was determined separately for each star, is because these small scale turbulent motions, i.e. smaller than the line forming region, will effect the line formation and Doppler broaden the line (Gaussian line broadening Emerson 1996), which in turn will affect the resulting abundances. The microturbulence is proportional to the wavelength but independent of the mass of the atom in question (Emerson 1996). All the derived stellar parameters, and information needed to obtain these, are listed in Table 3.2 and 3.1.

To provide a rough idea on how large the impact of the stellar parameters on the silver line is, I have shown four figures of different syntheses indicating the behaviour of the 3280 Å silver line in dwarf and giant stars. I have selected a temperature that can represent both the dwarfs and the giants, which is T = 5500 K. This temperature is in the upper range of the giant's temperatures, and in the lower range of the dwarf's temperatures. The silver abundances synthesised are the same for both dwarfs and giants regardless of metallicity and have the values: [Ag/Fe] = -0.75, -0.25, 0.0 and 0.75. The first two figures show the effect of different temperatures (T = 5250, 5500 K) in metal-poor giants. For the largest silver abundance the 250 K change is visible, however, the Ag abundances are rarely that large (only in enhanced stars) and for the lower abundances, the difference is still there, though harder to distinguish. The silver line in the dwarfs are very weak at this metallicity (see Figure 3.3) and since I have no enhanced dwarf stars due to the observational bias (see Section 2.1.1) the silver lines will not be detectable at this metallicity ([Fe/H] = -2.8) due to e.g. blending lines like NH. I therefore chose to include a more metal-rich ([Fe/H] =

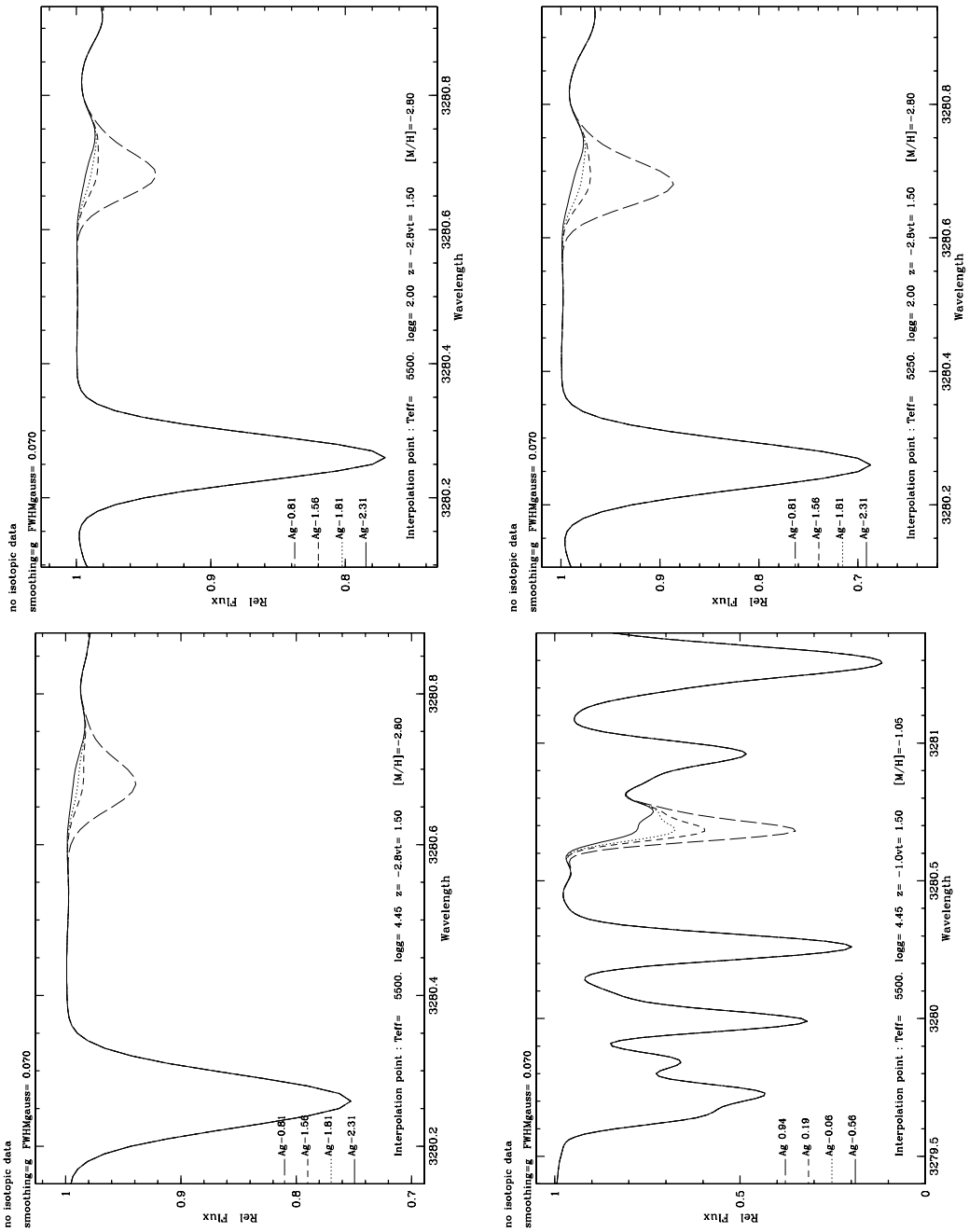

Figure 3.3: Four different syntheses with [Ag/Fe] = -0.75 (solid), -0.25 (dotted), 0.0 (dashed), 0.75 (long dashed) shown for stars with different stellar parameters. The values of the parameters are indicated in the figures. The upper two panels show giants (T/g/[Fe/H]; 5500/2.0/-2.8 and 5250/2.0/-2.8), while the lower two show dwarfs (T/g/[Fe/H]; 5500/4.45/-2.8 and 5500/4.45/-1.0).

-1.0) dwarf where the behaviour of the different silver lines is evident. The large number of

lines present in the last figure is due to the higher metallicity shown, and the crowding of the UV stands out (note the larger wavelength range shown here). From this comparison it can be seen that at low metallicity, the cool giants are the preferred stars to study silver in.

3.6 Error estimation

Every stellar parameter has a main contribution to the final error on the derived abundances, which needs to be included in the error propagation for the abundances (see Section 4.5). The largest source of error when estimating the temperature is the de-reddening, e.g., applying the overestimated de-reddening values from the Schlegel dust maps, may translate to errors on the derived temperature much larger than several hundred Kelvin (see Figure 3.1). Except for these extreme cases, the standard uncertainty on the de-reddening is usually 0.05 mag which together with the filter conversion uncertainty leads to an error of 100 - 150 K spanning from giants to dwarfs (due to the slightly stronger colour dependence in the dwarf's temperature compared to that of the giants). When excitation temperature is determined the adopted error is ± 100 - 150 K as well. I tested the slope/temperature relation in detail in four stars by running MOOG on a fine grid (step in temperature 25 - 50 K) of MARCS models and a list of the derived equivalent widths of the Fe lines. The temperature varies with $\sim 7 \pm 1.5$ K for a slope change of 0.001, a value I calculated by interpolating the slopes for two consecutive models with temperatures differing by 50 K. Generally, the excitation temperature was accepted if the slope was below ± 0.016, yielding uncertainties in the above mentioned range. This slope was chosen since the temperature and the number of iterations were acceptable.

The main uncertainty on the gravity comes from the uncertainty on the parallax. The common average error on the parallaxes is ± 1.4", which translates into 0.2 - 0.25 dex in log g. A change of 100 K in temperature only affects the parallax determined gravity with 0.04 dex, confirming that the parallax has the largest influence on log g. By altering the gravity with -1 dex, the Fe II abundance is lowered by -0.5 dex, whereas the Fe I abundance remains the same. From this it is evident that Fe II is very log g sensitive and Fe I is not.

Generally, the metallicity is based on solid equivalent width measurements from which the values of Fe I and Fe II agree within 0.1 dex, confirming the literature values for the metallicity of these well studied stars. Therefore the adopted error on the metallicity is 0.1 dex. Only for a few stars a maximum difference between Fe I and II allowed is 0.15 dex and leads to an uncertainty of ± 0.15 dex in [Fe/H].

The microturbulence velocity is derived by minimising the slopes between equivalent widths and Fe I abundances (see Figure 3.2). Using the iterative process I have estimated uncertainties of the order of 0.15 km/s, stemming from the error on the [Fe/H] and the uncertainty of the equivalent width measurements of Fe (see below).

Since the stellar parameters are interdependent the error on one stellar parameter will affect another parameter. Several tests have shown that this has only a minor effect. For instance, an uncertainty of ± 0.15 dex in metallicity will result in an error of ± 1 K

for most of the sample stars, and only in a few cases lead to an error of ± 10 K in the stellar temperature. The uncertainty of ± 0.2 dex on the gravity causes an uncertainty in the temperature of ± 1 - 6 K. The microturbulent velocity was found to have almost no impact on the temperature. This confirms that the reddening is indeed the major source of uncertainty for the temperature.

Finally, measuring the equivalent widths of the Fe lines will introduce some errors in the stellar parameters. The error on the equivalent widths are ± 2 mÅ . This value was assessed by carrying out the measurements of the same lines in the same stars at different days, which shows that the measurements are quite robust. The effect on the gravity amounts to an 0.01 dex offset, a 0 - 25 K offset in the temperature, $\sim$ 0.05 dex in [Fe/H] and less than 0.1 km/s change in the microturbulence velocity.

Table 3.1: Values applied to derive the stellar parameters for my giant and RR lyrae stars. Listed below are: Star, V magnitude, K magnitude, parallax (π in mas), error on π, E(B-V) reddening, temperature [K], gravity (log g) [dex], [Fe/H], microturbulence velocity [Km/s]. (a) Stars with Teff and log g derived from excitation potential and ionisation balance. (b) Stars with an elemental r-process enhancement. (c) Stellar parameters were lowered in order to fulfil different criteria (see text). The last two stars listed here are RR lyrae stars.

Star	V	K	π	$\sigma(\pi)$	E(B-V)	T	g	[Fe/H]	ξ
BD-01 2916	9.31	8.03	20.20	16.60	0.00	4480[a]	1.20[a]	-1.99	2.4
BD+8 2856	–	–	–	–	0.00	4600[a]	0.80[a]	-2.09	2.0
BD+30 2611	9.13	6.09	3.45	1.31	0.02	4238	0.50[a]	-1.20	1.7
BD+42 621	10.5	9.76	16.10	30.50	0.00	4725	1.50	-2.48	1.7
BD+54 1323	9.34	7.37	1.22	1.20	0.01	5213	2.01[c]	-1.64	1.5
CS22890-024	13.41	11.44	–	–	0.05	5400	2.65[a]	-2.77	1.7
CS29512-073	13.92	12.51	–	–	0.05	5000	1.85[a]	-2.67	1.1
CS30312-100	13.05	10.88	–	–	0.08	5200	2.35[a]	-2.62	1.4
CS30312-059	13.14	10.70	–	–	0.12	5021	1.90[a]	-3.06	1.5
CS31082-001[b]	11.67	9.46	–	–	0.00	4925	1.51[a]	-2.81	1.4
HD74462	8.69	6.05	1.55	1.16	0.05	4590	1.84	-1.48	1.1
HD83212	8.33	5.61	1.96	0.98	0.05	4530	1.21[c]	-1.25	1.8
HD88609[b]	8.59	6.01	0.63	1.14	0.01	4568	1.01	-2.87	1.9
HD108317	8.03	6.15	4.53	1.06	0.01	5360	2.76[c]	-2.11	1.2
HD110184	8.27	5.35	1.00	0.99	0.02	4450[a]	0.50[c]	-2.40	2.1
HD115444[b]	8.96	6.61	3.55	1.12	0.01	4785	1.50	-3.00	2.1
HD122563[b]	6.20	3.73	3.76	–	0.025	4560[a]	0.90[a]	-2.81	1.8
HD122956	7.25	5.90	3.30	–	0.083	4700	1.51	-1.45	1.2
HD126238	7.66	5.34	3.81	0.95	0.04	4900	1.80	-1.92	1.5
HD126587	9.11	6.668	1.40	1.44	0.09	4700[a]	1.05[c]	-3.16	1.7
HD128279	7.97	7.07	5.96	–	0.10	5200[a]	2.20[a]	-2.34	1.3
HD165195	7.34	4.14	2.20	–	0.195	4200[c]	0.90[c]	-2.10	2.1
HD166161[b]	8.12	5.34	3.25	1.19	0.13	5250[a]	2.15[c]	-1.25	1.9
HD175305	7.18	5.06	6.18	0.56	0.03	5100[c]	2.70[c]	-1.38	1.2
HD186478	9.14	6.44	1.34	1.25	0.12	4730	1.50[c]	-2.42	1.8
HD204543	8.28	5.78	0.24*	1.38	0.04	4700	0.80[a]	-1.84	2.0
HE0315+0000	15.52	13.20	–	–	0.081	5200	2.40[a]	-2.59	1.6
HE0442-1234	12.91	9.96	–	–	0.133	4530	0.65[a]	-2.32	1.8
HE1219-0312	15.94	13.89	–	–	0.00	4600	1.05[a]	-3.21	1.4
CS 22881-039	–	–	–	–	–	5950	2.10	-2.75	3.0
CS 30317-056	–	–	–	–	–	6000	2.00	-2.85	3.0

Table 3.2: Column 2- 7: Values applied to derive the stellar parameters for my dwarf stars. Column 8 - 11: My determinations of the stellar parameters. See Table 3.1 for explanation on a,b,c.

Star	V	K	π	$\sigma(\pi)$	E(B-V)	Mass	T	g	[Fe/H]	ξ
BD+092190	11.15	9.91	1.04	2.79	0.0281	0.8	6450	4.00	-2.60	1.5
BD-133442	10.29	9.02	–	–	0.044	0.8	6450	4.20	-2.56	1.5
CD-3018140	9.95	8.66	7.32	1.56	0.030	0.75	6340	4.13	-1.92	1.0
CD-33 3337	9.08	7.67	9.11	1.01	-0.0155	0.8	5952	3.95	-1.55	1.4
CD-45 3283	10.57	8.97	15.32	1.38	0.0001	0.8	5657[c]	4.97	-0.99	0.8
CD-57 1633	9.53	8.09	10.68	0.91	0.0	0.8	5907	4.26	-1.01	1.1
HD3567	9.26	7.89	9.57	1.38	-0.0028	0.82	6035	4.08	-1.33	1.5
HD19445	8.05	6.64	25.85	1.14	-0.0014	0.70	5982	4.38	-2.13	1.4
HD22879	6.69	5.18	41.07	0.86	-0.0056	0.8	5792	4.29	-0.95	1.2
HD25704	8.12	6.56	19.02	0.87	-0.0211	0.8	5700	4.18	-1.12	1.0
HD63077	5.36	3.75	65.79	0.56	-0.0225	0.8	5629	4.15	-1.05	0.9
HD63598	7.95	6.37	20.14	1.09	0.0	0.8	5680	4.16	-0.99	0.9
HD76932	5.80	4.36	46.90	0.97	-0.024	0.85	5905	4.08	-0.97	1.3
HD103723	10.07	8.66	7.63	1.62	0.038	0.88	6128	4.28	-0.85	1.5
HD105004	10.31	8.87	2.68	4.49	0.038	0.8	5900[a]	4.30	-0.84	1.1
HD106038[b]	10.18	8.76	9.16	1.50	-0.025	0.70	5950	4.33	-1.48	1.1
HD111980[b]	8.37	6.77	12.48	1.38	-0.0113	0.79	5653	3.90	-1.31	1.2
HD113679	9.70	8.11	6.82	1.32	0.024	0.96	5759	4.04	-0.63	0.9
HD116064	8.81	7.31	15.54	1.44	0.0352	0.8	5999	4.33	-2.19	1.5
HD120559	7.97	6.2	40.02	1.00	0.0070	0.8	5411	4.75	-1.33	0.7
HD121004	9.03	7.43	16.73	1.35	0.017	0.80	5711	4.46	-0.73	0.7
HD122196	8.73	7.28	9.77	1.32	0.032	0.78	6048	3.89	-1.81	1.2
HD126681[b]	9.30	7.63	19.16	1.44	-0.0183	0.70	5532	4.58	-1.28	0.6
HD132475	8.56	6.91	10.85	1.14	0.058	0.75	5838	3.90	-1.52	1.5
HD140283	7.21	5.59	17.44	0.97	0.021	0.75	5738	3.73	-2.58	1.3
HD160617	8.73	7.31	8.66	1.25	0.0155	0.82	6028	3.79	-1.83	1.3
HD166913[b]	8.23	6.92	16.09	1.04	-0.004	0.73	6155	4.07	-1.30	1.5
HD175179[b]	9.07	7.54	11.85	1.52	-0.0056	0.80	5758	4.16	-0.72	0.9
HD188510	8.83	7.13	25.32	1.17	0.0141	0.68	5536	4.63	-1.58	1.0
HD189558	7.74	6.16	14.76	1.10	0.0042	0.76	5712	3.79	-1.18	1.2
HD195633	8.55	7.10	8.63	1.16	0.0253	1.10	6005	3.86	-0.71	1.4
HD205650	9.05	7.57	18.61	1.23	-0.007	0.70	5842	4.49	-1.19	0.9
HD213657	9.66	8.35	5.68	1.54	0.0099	0.77	6208	3.78	-2.01	1.2
HD298986	10.05	8.74	7.68	1.43	0.000	0.76	6144	4.18	-1.48	1.4
G005-040	10.76	9.13	–	–	0.0366	0.8	5766	4.23[a]	-0.93	0.8
G013-009	10.0	8.74	5.75	1.55	0.027	0.76	6416	3.95	-2.27	1.4
G020-024	11.13	9.67	5.42	2.32	0.118	0.78	6482	4.47	-1.89	1.5
G064-012	11.46	10.21	1.88	2.90	0.042	0.8	6459	4.31	-3.10	1.5
G064-037	11.14	9.92	2.88	3.10	0.0127	0.8	6494	3.82	-3.17	1.4
G088-032	10.78	9.54	3.07	2.32	-0.0028	0.80	6327	3.65	-2.50	1.5
G088-040	8.93	7.51	12.15	1.24	-0.0084	0.8	5929	4.14	-0.90	1.4
G183-011	9.86	8.60	6.47	7.85	0.0084	0.70	6309	3.97	-2.12	1.0

Chapter 4

Abundance Analysis

Two different methods were applied to determine the abundances of this project, namely equivalent width measurements and spectrum syntheses. Both approaches require atomic and the latter also a molecular line lists, model atmospheres and a spectrum synthesis code.

4.1 The tools: MOOG and MARCS

MOOG spectrum synthesis code (Sneden 1973, version 2009) was used for determining the abundances. It is a FORTRAN code with a user-friendly graphical interface, which offers the possibility to visualize abundance plots and synthetic spectra, and to interact with them in real time (e.g. by changing the continuum placement, input abundances etc.). It is a 1D LTE code, i.e. line transitions are not treated by exact/detailed statistical calculations based on quantum level populations, but calculated instead under the assumption of local thermodynamic equilibrium (LTE). This allows excitations to be described by the Boltzmann equation and ionizations to be characterized by the Saha equation (see section 4.2).

The MARCS 1D model atmospheres (Gustafsson et al. 2008) have been downloaded from the MARCS web page (http://www.marcs.astro.uu.se/) and interpolated to the proper stellar parameters by using the Masseron FORTRAN interpolation routine (Masseron 2006).

4.2 Stellar atmospheres and terminology

In order to derive stellar abundances, we need a stellar model atmosphere calculated with the proper stellar parameters (T, log g, [Fe/H] and ξ, the microturbulent velocity). The stellar model atmospheres connect temperature, electron pressure, absorption coefficient and density at various optical depths (τ), leading to a T - τ relation. These models together with the detailed line lists are used by synthetic spectrum codes, in order to reproduce the formation of all spectral lines and to calculate their sizes and shapes. The line list feeds

all atomic and molecular information such as central wavelength of the line, excitation potential and the line's transition probability specified via the so-called oscillator strength. To finally derive the stellar abundances in local thermodynamic equilibrium, I can choose to synthesize the spectral region of interest, thereby solving the inverse problem (i.e. computing a synthetic spectrum and varying abundance until the correct equivalent width of the line is obtained and the synthetic spectrum matches the observed spectrum). Alternatively, I can measure the equivalent widths, applying the same models and codes thereby deriving the abundances and solving the direct problem. The equivalent width corresponds to the area covered by the spectral line:

$$W_\lambda = \int 1 - \frac{F_\lambda}{F_0} d\lambda \tag{4.1}$$

where F_0 is the continuum flux, F_λ is the line flux and W is the equivalent width. The equivalent width can now be related to the abundance via absorption coefficients and transition probabilities:

$$\log(W_\lambda) = \log(constant) + \log(A) + \log(gf\lambda) - \theta_{ex}\chi - \log(\kappa_\nu) \tag{4.2}$$

where A corresponds to the elemental abundance, calculated as the fraction of the number density of the element over the number density of hydrogen (see also equation 5.3). The oscillator strength is represented by log (gf), one of the parameters describing the line strength, $\theta_{ex} = 5040/T$ (T being the temperature), χ is the excitation potential and κ is the absorption coefficient. This general description of the abundance - equivalent width relation, can also be written in a different way with the constant specified (see equation 4.3). For weak lines we can apply the Milne-Eddington approximation, which assumes that the source function[1] is a linear function of the continuum optical depth (τ_C), and the relation gains the following shape:

$$\frac{W}{\lambda} = \frac{\pi e^2}{4\pi\epsilon_0 mc^2} \frac{R_C}{\alpha_C} \lambda gf \frac{N_i}{gN_{ion}} \frac{N_{ion}}{N_{elem}} \frac{N_{elem}}{N_H} \tag{4.3}$$

where N_i/N_{ion} represents the fraction of excited atoms, ions or molecules described by the Boltzmann equation, and N_{ion}/N_{elem} is given by the Saha equation yielding the fraction of ionized species. The ratio N_{elem}/N_H, corresponds to the log(A) term in equation 4.2. Phrased differently, altogether these number densities describe the number of atoms per unit mass which are capable of absorbing radiation relative to the number of hydrogen atoms (Emerson 1996). This is indirectly what we are measuring when we derive abundances from absorption lines. The constants in equation 4.3 represent:

[1]The source function describes the ratio of the emission coefficient relative to the absorption coefficient

α_C = the product of continuous absorption coefficient and continuous absorption cross-section per hydrogen atom
R_C = maximum central line depth
m = electron mass
ϵ_0 = vacuum permeability
g = statistical weight of the lower level of the transition
f = oscillator strength

When deriving the abundances, a set of simplifying assumptions are usually made. The two most important ones are that the model atmosphere is one dimensional and that the synthetic spectrum code assumes LTE conditions. This implies that a stellar atmosphere layer is assumed to be dominated by collisions (generally true at high densities) and that any localized area can be described by one temperature only. However, in the outer parts of the stellar atmosphere the density is lower and LTE might not be a valid assumption any longer. A statistical calculation of the quantum level population including both radiative and collisional transitions of all concerned levels might be necessary. This is generally referred to as a non-LTE or NLTE case. The NLTE abundances are estimated as the deviation from LTE via statistical equilibrium calculations and the LTE abundance is then corrected accordingly.

Two of the neutron-capture elements under study are palladium and silver (Pd and Ag), only have weak lines (validating the above mentioned formula) in the near-UV (e.g. 3280 and 3404 Å). The study of these elements relies on absorption lines formed relatively deep in the stellar atmosphere. Also, because of their relatively low temperature and low gravity, giant stars are preferred targets: They have extended atmospheres making it easier to observe weak lines found deep in the stellar interior, due to the lower opacity encountered along the radiation path. On the contrary, dwarf stars are much tighter bound, due to their high gravities, hence the optical depth at which the atmosphere becomes optical thick (τ = 1, and impenetrable to observations) is found at a geometrically speaking much "higher" point in the stellar atmosphere. This means that it is possible to observe geometrically deeper in the atmosphere of giants than of dwarfs before reaching the $\tau = 1$ limit. This partly explains the sample bias I have and why the Pd and Ag lines are easier to observe in metal-poor giants than dwarfs. Still, it remains possible to study neutron-capture elements in dwarfs as well. The last missing input before being able to derive any stellar abundances is a list with lines of interest and their atomic/molecular characteristics.

This list will be described below.

4.3 Compiling a line list

Creating a complete up-to-date line list is very important for obtaining accurate abundances, especially in the near-UV where there are severe line blends (see Figure 1.5). Unfortunately, a lot of lines in the near-UV have not been properly measured yet, thus

I am sometimes forced to rely on line predictions[2]. In my case, the core of the line list was retrieved from VALD[3] (Kupka F. 2000) the Vienna Atomic Line Database. The lines were extracted applying the 'extract all' option, which yields everything available in the database in the given wavelength interval. This is not the case if further constraints are added to the search, e.g. by providing the stellar parameters, the VALD search selects only lines that are visible in the that type of stars. I wished to control that selection myself with support lend from literature. Hence, a cut in log gf and excitation potential was introduced in order to remove all very weak lines. Lines with log gf values less than -4 dex and excitation potentials above 4 eV were excluded. A similar cut was made by Johnson & Bolte (2002). Several different cuts were tested, however, the chosen values are the maximum cuts that can be introduced without removing lines that effectively (and individually) contribute to the spectral synthesis. Lines with excitation potentials above 4 eV and log gfs below -4 dex, are not visible in the spectra in the observed or synthetic spectra. Together, all the weak lines have a combined effect on the continuum, and excluding all the weak lines lead to a higher continuum placement (in better agreement with the observed spectra), which in turn meant larger abundances. The effect of removing the weak and invisible lines, corresponded to a ~ 0.2 dex larger silver abundance. The atomic values of this list were then cross-checked against the NIST[4] database, and I searched the literature for recent analyses of atomic lines. When synthesizing regions around Ag and Pd located in the near-UV, there are a lot of molecular lines, especially NH, that are affecting these regions. All the molecular lines were taken from Kurucz's database[5].

The atomic values of the Pd line (3404.58 Å) found in VALD were directly used in the spectrum synthesis. This was not the case for Ag, since the line transitions of the two silver isotopes (^{107}Ag and ^{109}Ag) are affected by hyperfine splitting (hfs). A literature search on silver's hfs values only yielded the somewhat old study by Ross & Aller (1972), in which they include two hyperfine levels. This was the basis for a collaboration with H. Hartmann working at the atomic laboratory in Lund. He measured and provided new log gf values for silver, now based on three hyperfine levels.

The hyperfine splitting arises because the interactions between the nucleus and the moving electrons create a magnetic field around the nucleus (Brandsden & Joachain 2003). This magnetic field can cause perturbations of the systems energy leading to the splitting of the energy levels (ΔE_{HFS}), which can be characterized by:

$$\Delta E_{HFS} = \frac{1}{2} A_{HFS}[F(F+1) - J(J+1) - I(I+1)], \tag{4.4}$$

where I is the total angular momentum (or nuclear spin), J is the total electronic angular momentum (a sum of the orbital angular momentum and the spin) and F is the total angular momentum of the atom ($F = I + J$; nucleus plus electron). A_{HFS} is the hyperfine

[2]mostly taken from the list of predicted lines assembled by R. Kurucz and available at http://cfaku5.cfa.harvard.edu/atoms.html

[3]http://vald.astro.univie.ac.at/∼vald/php/vald.php

[4]http://physics.nist.gov/PhysRefData/ASD/lines_form.html

[5]http://kurucz.harvard.edu/molecules.html

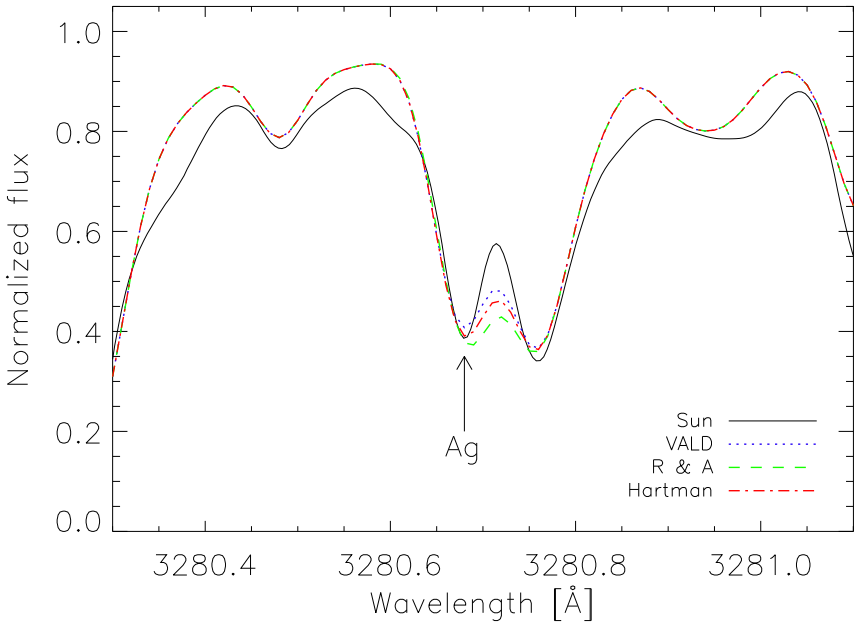

Figure 4.1: The solar spectrum (Kitt Peak) with different spectrum synthesis over-plotted. In dotted blue a line list with VALD's log gf and no hfs is over-plotted, in red (dash-dotted) the spectrum is based on a line list containing log gfs with the most recent hfs from H. Hartmann is over-plotted. Finally, the green – dashed spectrum calculated with a line list is based on the old hfs (only two levels) from Ross & Aller (1972) – R & A.

magnetic dipole moment. Since the silver isotopes have mass numbers of 107 and 109, and show transitions from a 5s to a 5p level (resonance lines) with a nuclear spin of I = 1/2, only the magnetic dipole moment is non-zero (Cowan 1981). From the energy splitting (difference) the frequency, hence the relative wavelengths of the transitions can be found: $\nu = \Delta E/h$. In order to obtain absolute wavelengths the different components of the resonance lines can be determined via centre of gravity measurements (Pickering & Zilio 2001). Furthermore, once the wavelength for each transition is known as well as the lifetime (which can be measured by laser spectroscopy, Carlsson et al. 1990) the hfs log gf can be calculated:

$$gf = 1.499 \cdot 10^{-14} \lambda^2 g \frac{1}{\tau} \tag{4.5}$$

where gf is the transition strength, g is the statistical weight, λ is the wavelength and τ is the lifetime ($1/\tau$ = A, the transition rate).

This was an important step forward because even if the Ag lines are relatively weak, different treatments of hfs have a clear impact on the log gf values, and in turn on the abundances. If I had adopted the log gf value available from VALD without hfs all the Ag abundances would have been overestimated (see Figure 4.1). This effect is even more

pronounced in the cool metal-rich stars, where the silver lines are stronger. The new hfs predicted log gf values can in dwarf stars, like the Sun, lead to a difference of $\sim<+0.2$ dex in silver abundances, compared to the results based on Ross & Aller (1972) values (see Figure 4.1). The figure shows that the blue dotted line synthesised without hfs (log gf from VALD) yields a weak line (compared the the syntheses that includes hfs), and a larger Ag abundance would be needed in order to make this line stronger and match the observations. Hence, neglecting hfs would lead to overestimated silver abundances.

Unsatisfactory synthetic spectral fits confirmed by a literature study showed the need for a 'fake' iron line in the Ag line's wing. The 3280 Å Ag line experiences several blends in the red wing of which Zr II, Mn I, NH and Fe I are the dominant ones. A cerium line weakly blends in the blue wing of the 3280 Å line, but is only noticeable in very r-process enhanced stars. The Fe I line strength was empirically adjusted in order to obtain a satisfactory fit of the red wing. For the 3382 Å Ag line, Moore et al. (1966) have a Fe I line in their line list, which, however, has not been found in VALD or NIST, but it is necessary in order to obtain a satisfactory fit (see Figure 4.2). The excitation potential of this Fe I line is known, but not the log gf, which I have constrained by running several tests on both dwarfs, giants and the Sun.

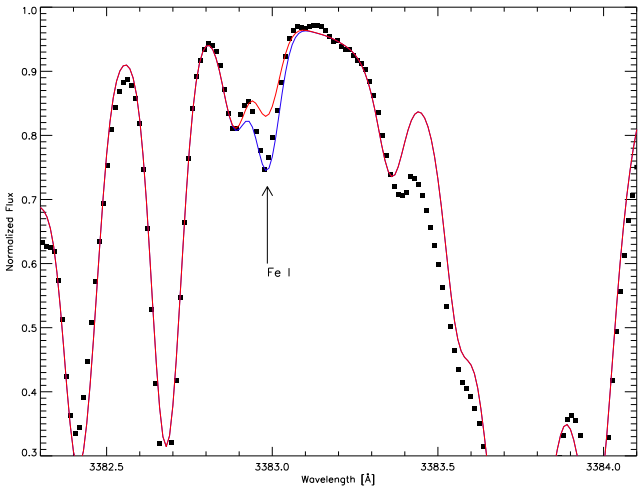

Figure 4.2: A spectrum of HD121004 (dots) to which two syntheses are fitted. The red indicates that the log gf value is too low, while the blue shows the properly adjusted log gf for the blending Fe I line.

Between the two Ag lines, the 3382 Å Ag line is the cleanest and has only a blending Fe I line in it's red wing. Furthermore, the two features surrounding the 3382 Å Ag line are easily resolvable, allowing a more straightforward synthesis than the 3280 Å line does. The palladium line shows similar blends as the 3382 Å Ag line, but the iron blend is in the blue wing in the case of Pd. No strong changes around the Pd line were required.

Line lists for iron transitions and other heavy elements were also assembled. For iron

(see appendix A.1), it is important to include lines with different strengths and excitation potentials, because the range in Fe I line strength is needed in order to determine the microturbulence velocity, and the span in excitation potential is necessary to constrain the excitation temperature. The line list for the heavy elements includes strong lines visible in most of the stars (see Section 4.4.1).

4.4 Calibrating the line list

Every line list needs to be calibrated, so that it does not introduce biases in the derived abundances. In my case the line list was first of all calibrated on the Sun, for which the abundances are very accurately known, allowing a detailed comparison of derived abundances to literature values. For this purpose, I need to select a solar spectrum and there are several high resolution solar spectra available. The tests have been carried out on three different spectra: The UVES solar spectrum (R $\sim$ 85000, http://www.eso.org/observing/dfo/quality/UVES/ pipeline/solar_spectrum.html), the Kitt Peak solar spectrum (R $\sim$ 840000) and the Kurucz solar flux atlas (R $\sim$ 500000, http://kurucz.harvard.edu/sun.html). According to Caffau et al. (2010) different solar spectra yield different abundances, which is indeed confirmed by this study. From the UVES solar spectrum a very low silver abundance is derived. An average of the two silver lines yield a value of log ϵ $(\mathrm{Ag})_{\odot} = 0.63 \pm 0.27$ dex, but such a large standard deviation is unacceptable. A fit to the Kurucz solar spectrum yields a similar result. In this case the average Ag abundance I derived is 0.87 $\pm$ 0.25, again too large a standard deviation. In both cases the 3280 Å line yields a lower abundance (more than 0.3 dex lower). In addition, a careful inspection of the Kurucz solar spectrum showed that the 3382 Å line also had problems around the line centre, which are very difficult to quantify, hence these abundances should not be trusted. Therefore I decided to use the Kitt Peak solar spectrum, which supplies more consistent solar abundances. This could be due to the fact that this spectrum has the highest resolution and S/N ratio. However, the two silver abundances derived from this analysis still differ by 0.19 dex, which is too much. Since there seems to be nothing wrong with either this or the UVES spectrum, the reason must be found in the line list. As a matter of fact, a detailed comparison of line lists showed, that a blending Fe I line at 3280.67 Å, which is included in VALD with a log gf of -2.231 dex, could not be found in any other database like NIST or G. Nave's UV Fe lists (Nave et al. 1997). Nave et al. (1997) found and measured a line with similar characteristics but 0.4 Å away. The log gf and excitation potential of the Fe I line at 3280.67 Å are taken from Kurucz's CD-ROM 20-22 (and is a calculated line). By changing this Fe line's log gf to -2.5 dex leads to similar solar silver abundances from both lines, and a double check of all giants and dwarfs confirmed this improved agreement (see Figure 4.3). The largest effect was found for the more metal-rich stars, where the measure of this iron line blend affects and reduces the Ag abundance from the 3280 line much more than in the metal-poor stars.

Returning to the Kitt Peak spectrum, and introducing the modified log gf of the Fe I blending line, an average silver abundance of 0.93 $\pm$ 0.02 dex was obtained (0.94 dex

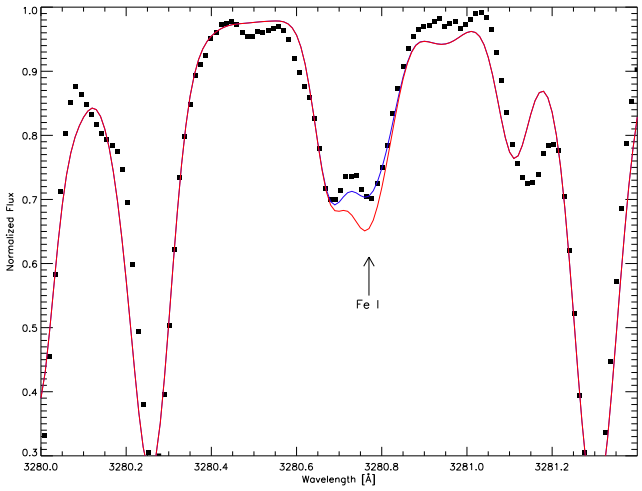

Figure 4.3: The effect of a wrong log gf of the blending Fe line (marked by arrow) shown for HD121004. The too large log gf of Fe not only overestimates Fe but also affects (underestimates) the Ag abundance; see the red line (large log gf) compared to the correctly adjusted log gf shown in blue.

and 0.91 dex is derived from the 3280 Å and the 3382 Å line, respectively). The best fit can be seen in Figure 4.1. This value is in very good agreement with the solar value of 0.94 dex from Asplund et al. (2009). I have for consistency adopted the solar values from Asplund et al. (2009), and the tests on the three solar spectra served as a calibration of the line list, since log gfs of blending lines were adjusted during the abundance fitting. The tests also confirmed the differences of the solar spectra that were earlier noted by Caffau et al. (2010). Further log gf adjustments for other elements were implemented as well, but only if they provided satisfactory results on all test stars. These changes were only made if necessary in all the test stars. Such adjustments are justified in the near-UV range, where the log gf values often are uncertain and only based on theoretical predictions. For instance, the Zr II line blending in the red wing of the 3280 Å line also needed some adjustment since its derived Zr abundance was always higher than the Zr abundance determined from other Zr lines. By reducing the log gf of the 3280.735 Å Zr line by 0.4 dex, the stellar spectra were then satisfactorily fitted and the Zr abundances from other lines agreed with the values obtained from this line (see Figure 4.4).

Checking the synthesis of the region around the Pd line in the Kitt Peak spectrum was more straightforward than synthesizing the regions around the blue silver line. The palladium line list was partially based on the line list published in Johnson & Bolte (2002) and partly on VALD. The list required very few empirical adjustments and the solar value obtained from synthesizing the line in the Kitt Peak solar spectrum was $\log \epsilon\ (\mathrm{Ag})_{\odot} = 1.52$ dex (see Figure 4.5). This values compares very well to the solar abundance of Pd given in Asplund et al. (2009), where they derived 1.57 dex as the solar Pd abundance.

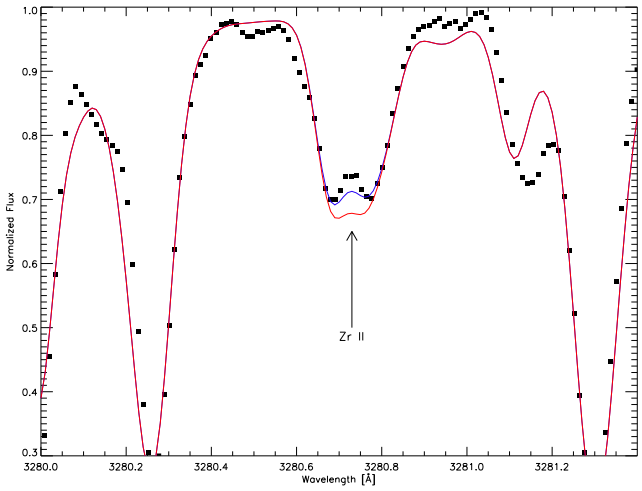

Figure 4.4: Two different log gf values for Zr are shown here; in blue -1.5 dex and in red -1.1 dex, which shows that a reduction in this zirconium line's log gf value was necessary to obtain better fits and correct silver abundances.

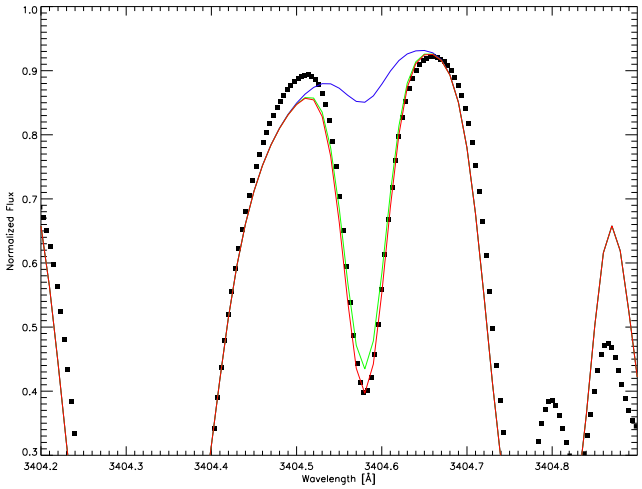

Figure 4.5: Different palladium abundances fitted to the Sun; blue - no Pd, green - log epsilon= 1.39 and red - log epsilon = 1.52.

Including the above mentioned line adjustments abundances derived from different lines of the same element agree within 0.1 dex. A few stars showed larger differences between e.g. the two Ag lines, but this was limited to cases where one of the two lines was very noisy or gave only an upper limit estimate.

All the tests I have preformed, show the importance of a properly calibrated line list, since all the silver abundances obtained from the 3280 Å line would otherwise have been

Table 4.1: Atomic data for the strontium: Wavelength, excitation potential and log gf.

Sr II	ξ [eV]	log gf [dex]
3464.45	3.04	0.49
4077.71	0.00	0.17
4161.79	2.94	-0.50
4215.52	0.00	-0.14

0.3 dex lower than those obtained from the 3382 Å line, which is 'un-physical'.

4.4.1 Determining abundances

Due to severe line blanketing affecting the near-UV/blue part of the spectra of all stars, blends play a big role, thus requiring a spectrum synthesis in order to derive accurate abundances. Equivalent width measurements would lead to erroneous large (overestimated) abundances. The other elements, Sr, Y, Zr, Ba, Eu and in particular Fe have abundances derived from equivalent width measurements, carried out in IRAF and Fe in `Fitline`, due to the large number of Fe lines. All these elements have several lines spreading over a large wavelength range, allowing a choice of un-blended lines in redder parts of the spectra, as well as relatively clean near-UV lines. The equivalent widths were mostly measured by manually fitting Gaussian line profiles in IRAF. Carrying out the measurements this way in IRAF is time consuming but at the same time allows a careful inspection of the spectra, and ensures that possible problems with the data reduction in the spectral region of interest will be caught and corrected. It also allows fitting Lorentz or Voigt profiles to the lines if these profiles seem visually better suited to fit the observed line profile than the standard Gaussian. The average error on the equivalent width measurements of Sr and Y are around 2.5 mÅ and slightly larger for Zr, Ba and Eu ($\sim$ 4 mÅ). These errors have been incorporated in the total uncertainty of the abundances shown in the abundance figures in Chapter 5. The lines chosen to obtain the abundances for target elements between Sr and Eu are listed and shortly discussed below in chronologically increasing atomic number order. In all the tables below, the central wavelength of the line together with the atomic data are given. The excitation potential can be found in the second column and the log gf in the third column. The values are taken from the Vienna Atomic Line Database (VALD Kupka F. 2000).

• Strontium (Sr, Z = 38): This s-process element, is generally detectable even in the most metal-poor stars, due to the strong resonance line found at 4077 Å. This line is NLTE affected according to Belyakova & Mashonkina (1997), however, the corrections depend strongly on the stellar parameters. In halo dwarf stars the NLTE correction can be +0.3 dex or even larger in halo giant stars (Asplund 2005). The lines measured to obtain the Sr abundance are generally ionized (see Table 4.1).

• Yttrium (Y, Z = 39): A neutron-capture (s-process) element. The derived abundances tend to be much lower than predicted by solar scaled ratios, more than what is common

Table 4.2: Atomic data for the yttrium: Wavelength, excitation potential and log gf.

Y II	ξ [eV]	log gf [dex]
3549.01	0.13	-0.28
3600.74	0.18	0.28
3628.70	0.13	-0.71
3774.34	0.13	0.21
3788.70	0.10	-0.07
3950.36	0.10	-0.49
4398.01	0.13	-1.00
4854.87	0.99	-0.38
4883.69	1.08	0.07
5087.42	1.08	-0.17
5200.42	0.99	-0.57

for odd-Z elements. The Y lines are ionized.

• Zirconium (Zr, Z = 40): Again an s-process element that mainly shows ionized lines.

• Palladium (Pd, Z = 46): This is one of the key elements to possibly trace the weak r-process. The line measured is neutral. NLTE effects for this element are of unknown magnitude, and have never been determined, hence only LTE abundances are presented here. Palladium has six stable isotopes: ^{102}Pd,^{104}Pd,^{105}Pd,^{106}Pd,^{108}Pd and ^{110}Pd.

• Silver (Ag, Z = 47): This is another key element to possibly study the weak r-process. The two lines are neutral and have hyperfine structure (*hfs*), as indicated in Table 4.5. Silver has two stable isotopes (^{107}Ag and ^{109}Ag). The isotopic ratio for silver was used to calculate the strength of the lines, and the fraction of ^{107}Ag is 51.84 % while ^{109}Ag accounts for the remaining 48.16 %, i.e. the ^{107}Ag/^{109}Ag-ratio is 51.48/48.16. I carried out tests to see if strong alterations of this almost 50/50 ratio would lead to abundance changes. This was not the case, and even for a 99/1 ratio the abundances have not changed with a line width (see Figure 4.6). Part of the reason why no changes were found in this test, is because the log gf values were derived assuming this ratio, but another part of the reason is due to the resolution. In order to see isotopic changes for e.g. barium very high resolution ($\sim$ 95000) and large S/N-ratios are needed (Gallagher et al. 2010). At this resolution and S/N the details of the observed spectra are not fine enough to detect the influence of possible variations in Ag isotopic ratios.

• Barium (Ba, Z = 56): A s-process element for which I measured the equivalent widths from ionized lines. Barium is one of the few heavy elements that have recently been fully studied under NLTE. These corrections will be discussed in Chapter 5.

• Europium (Eu, Z = 63): This is the heaviest element studied here. It is the only main r-process element (94% main r-process according to Arlandini et al. (1999)). Only few, partial studies have been carried out on how possible NLTE effects will alter the LTE abundances, thus they will not be included in the following discussion. Most of the Eu lines used in this study are of weak to intermediate strength.

Table 4.3: Atomic data for the zirconium: Wavelength, excitation potential and log gf.

Zr II	ξ [eV]	log gf [dex]
3356.09	0.09	-0.51
3499.57	0.41	-0.81
3551.96	0.09	-0.31
3573.06	0.32	-1.04
3607.38	1.24	-0.64
3714.79	0.53	-0.93
4050.33	0.71	-1.00
4161.21	0.71	-0.72
4208.98	0.71	-0.46
4317.32	0.71	-1.38
5112.28	1.66	-0.59

Table 4.4: Wavelength, excitation potential and log gf for palladium.

Pd I	ξ [eV]	log gf [dex]
3404.58	0.814	0.320

Table 4.5: Wavelength, (isotope), excitation potential and log gf (with *hfs*) for silver.

Ag I		ξ [eV]	log gf [dex]
3280.678	(107)	0.00	-1.210
3280.678	(107)	0.00	-0.511
3280.679	(109)	0.00	-1.242
3280.680	(109)	0.00	-0.543
3280.684	(107)	0.00	-0.909
3280.686	(109)	0.00	-0.941
3382.885	(107)	0.00	-0.920
3382.884	(107)	0.00	-1.221
3382.886	(109)	0.00	-1.253
3382.887	(109)	0.00	-0.952
3382.891	(107)	0.00	-1.221
3382.894	(109)	0.00	-1.253

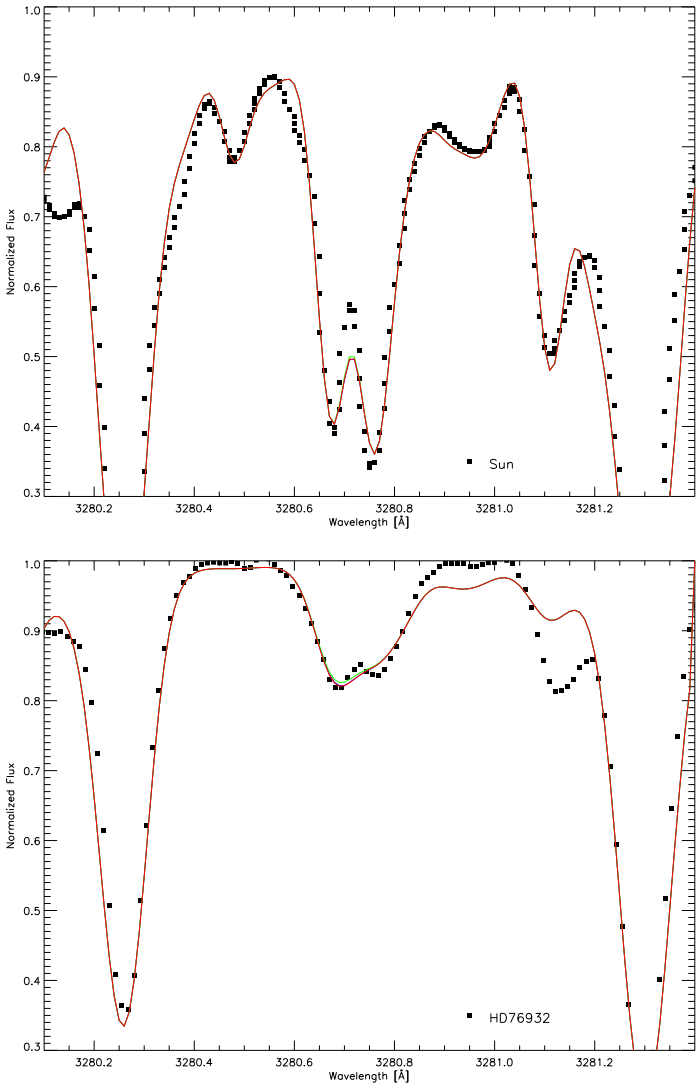

Figure 4.6: Isotopic ratios shown for the Sun and HD76932. The observed spectrum is shown as black squares, the red synthetic spectrum indicates the 48.16/51.84% ratio, the blue spectrum (which basically overlaps with the red synthesis) shows a 30/70% ratio and the green line indicates a 1 to 99% difference between the two isotopes. The red and the green line deviates by a line width, which would not even be detectable if the lines would lie exactly on top of the observations (I have therefore applied a small horizontal shift of the observations to increase the visibility of the similarities/difference in these syntheses). A clear continuum difference ($\sim$ 0.1 dex) is seen between the Sun and HD76932, which in part is due to their different stellar parameters, which molecules are very sensitive to.

The solar values adopted for each of these elements are taken from Asplund et al. (2009) as listed in Table 4.8.

Table 4.6: Wavelength, excitation potential and log gf for Ba.

Ba II	ξ [eV]	log gf [dex]
4130.65	2.72	0.56
4554.03	0.00	0.17
4934.08	0.00	-0.15
5853.67	0.60	-1.01
6141.71	0.70	-0.07
6496.91	0.60	-0.37

Table 4.7: Wavelength, excitation potential and log gf for Eu.

Eu II	ξ [eV]	log gf [dex]
3724.93	0.00	-0.09
4129.73	0.00	0.22
4205.04	0.00	0.21
4435.58	0.21	-0.11
4522.58	0.21	-0.67
6437.64	1.32	-0.32
6645.06	1.38	0.12

Table 4.8: Element and adopted solar abundance.

Element	dex
Sr	2.87
Y	2.21
Zr	2.58
Pd	1.57
Ag	0.94
Ba	2.18
Eu	0.52

Below, focus will be on Ag and Pd, how to derive their abundance, and how the abundances behave with varying line lists and stellar parameters.

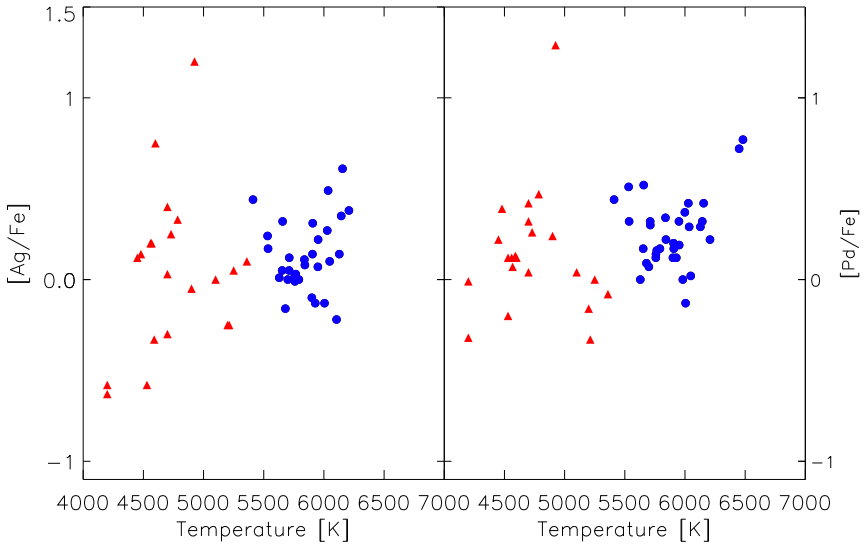

Figure 4.7: Temperature of both dwarfs (blue filled circles) and giants (red filled triangles) plotted versus [Ag/Fe], left, and to the right versus [Pd/Fe].

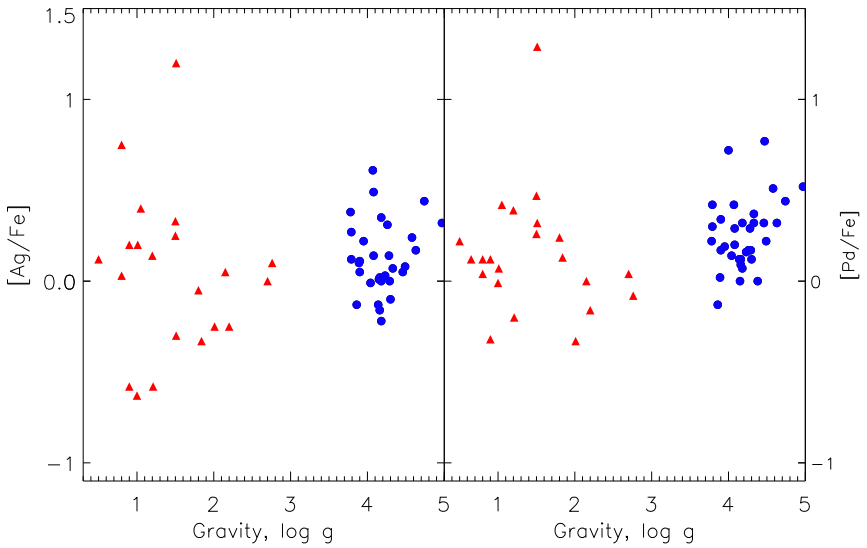

Figure 4.8: Surface gravity, log g, in dex of dwarfs and giants also plotted versus [Ag/Fe] and [Pd/Fe]. Legend as in Fig. 4.7.

4.4.2 How Abundances and Stellar Parameters relate

In order to test the reliability of my abundance determinations and prove that the derived trends provide information only on formation and evolution processes, and not on spurious analytical effects, it is important to carefully investigate the trends of the derived abundances with temperature, gravity and microturbulence. From inspecting Figures 4.7,

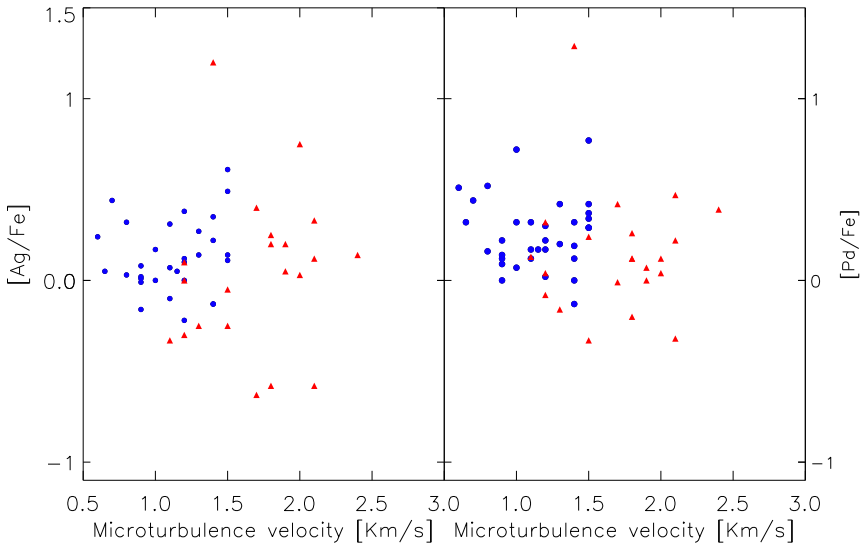

Figure 4.9: Micro turbulence velocity in km/s of dwarfs and giants also plotted versus [Ag/Fe] (left) and [Pd/Fe] (right). Legend as in Fig. 4.7.

4.8 and 4.9, we see that neither dwarfs nor giants show a dependence or correlation with temperature, gravity or microturbulence. In all three figures the abundances scatter or clump arbitrarily. Crawford et al. (1998) studied seven stars for silver abundances and found no trend with metallicity. This was confirmed by Hansen & Primas (2011) studying a much larger sample (see Chapter 5). The Pd abundances are also independent of [Fe/H] (Hansen & Primas 2011). From this much larger sample it should now be evident that neither Ag nor Pd show any dependence on metallicity. The figure showing this will be presented in the following chapter, where it is connected to a longer discussion on elemental abundance behaviour. Palladium and silver do not depend on microturbulence velocity either, as is seen from Figure 4.9.

However, the corresponding plots showing log ϵ (Ag) and log ϵ(Pd) versus stellar parameters indicate larger differences between the dwarfs and giants. Furthermore, in the figures with log epsilon scales there are no Fe abundances to veil the true behaviour of Ag and Pd with stellar parameters. This is clearly illustrated by Figure 4.10. Neither the dwarfs nor the giants show any trends among themselves, but fall in a clump as seen in Figures 4.7, 4.8 and 4.9.

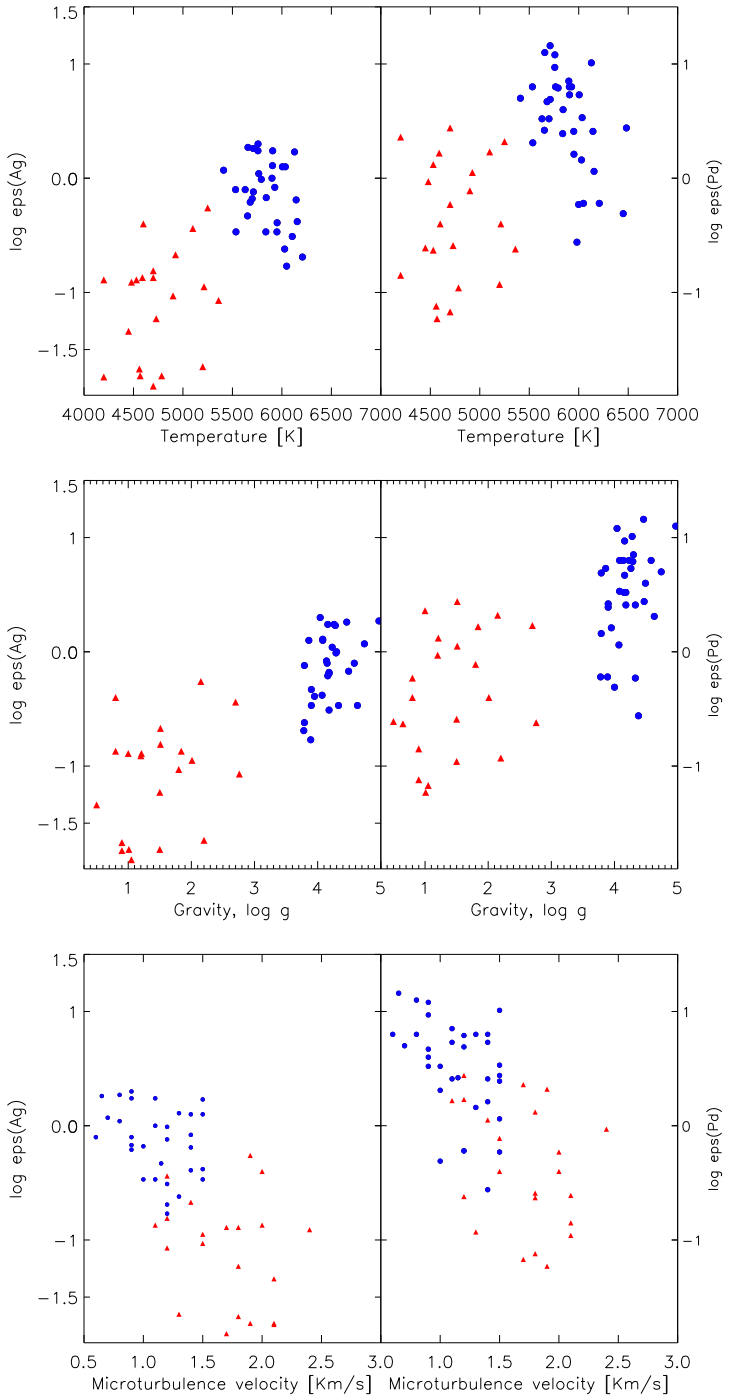

Figure 4.10: Similar to Figures 4.7 - 4.9 these figures show the Ag and Pd abundances and how they behave compared to the stellar parameters. The abundances shown here are on the log epsilon scale (meaning not scaled to the Sun or Fe - see equation 5.3), and they show a clearer division between the dwarfs and the giants, however, within the dwarfs there is no trend seen (only one elongated clump due to the span in abundances) and the same applies to the giants.

This means that by comparing the Ag and Pd abundances to Fe, the difference between dwarfs and giants is reduced, indicating that NLTE effects could be the reason for this difference, but that these effects are reduced by the Fe abundances in the abundance ratios. However, the abundance difference between dwarfs and giants could also be due to microturbulent velocity, to a wrong treatment of the T-τ relation in the model atmospheres of giants, or to unknown line blends in the spectra (Lai et al. 2008). According to Preston et al. (2006) the abundance difference cannot be explained by differences in stellar evolutionary stages.

4.5 Error propagation for the abundances

The typical uncertainties of the stellar parameters were ±100K, 0.2-0.25, 0.15 dex and 0.2 km/s for T, log g, [Fe/H] and the microturbulence velocity, respectively. The effects on the abundances of varying the stellar parameters with their uncertainties need to be investigated. In order to do so tests on two dwarfs and two giants were carried out, to see how the varying parameters would affect the abundances of more metal-poor and more metal-rich dwarfs and giants. The detailed effects of the abundance changes for silver will be described (similar test were made for palladium).

The silver abundances will be discussed for each line individually.
Both lines are very affected by changes in [Fe/H] due to the blends, but also due to the fact that the abundance ratio [Ag/Fe] depends on Fe, this can be reduced by only considering the silver abundances via the log epsilon abundance, which is not calculated relative to iron. However, the log epsilon abundances are still affected by line blends, and thereby indirectly by Fe, which blends with Ag. Besides metallicity, the 3280 Å line is seen to be most sensitive to microturbulence velocity and gravity, and to a slightly lesser extent the temperature, whereas the 3382 Å line is most sensitive to temperature and much less affected by microturbulence and gravity.

Additional uncertainties arise from continuum placement, which is not straightforward in the near-UV. The abundance uncertainty of this placement was based on an average of many stars and amounts to 0.05 dex for both Ag and Pd abundances. The synthesis is also not flawless, and several factors such as model atmospheres, assumptions in the synthetic spectrum code and incomplete line lists add up to an error of 0.1 dex for both elements. Preston et al. (2006) tested the effect different stellar model atmospheres have on the abundances and which kind of uncertainties they lead to. By analysing the same elements, applying the same code but using different model atmospheres (MARCS Gustafsson et al. 2008) versus (ATLAS Kurucz 1993) they obtained a difference of 0.05 dex in abundances, which in turn can account for the uncertainty different stellar model atmospheres cause.

Adding all the uncertainties in quadrature ended up giving an uncertainty of ± 0.2 dex for Pd and ± 0.25 dex for Ag. Similar tests were made for two stars for Sr, Y, Zr, Ba and Eu, one of them being CS 31082-001. The errors on the stellar parameters were very similar to those obtained by Hill et al. (2002), and after checking these two stars finding errors comparable to those published by Hill et al. (2002) as well as other studies

in the literature, these were adopted instead (since they were based on more stars). The error on the synthesis as well as the continuum placement were propagated together with these abundance uncertainties stemming from the stellar parameter uncertainties. The propagated errors for the heavy elements range from 0.1 dex to 0.3 dex (see Hill et al. 2002, and Table 5.4). Some stars have uncertain equivalent width measurements, which is taken into account in the synthesis abundance error.

4.6 From colour to abundances – a recipe

To illustrate how I derive the abundances which I present in the next chapter, I will go through all the steps i.e. determining the stellar parameters and synthesising the Ag abundance for one star, HD189558. I chose this star since it is a dwarf star for which equation 3.1 is valid, and because this star has an accurate parallax so equation 3.6 can be applied to determine the gravity.

Starting from the very beginning only the dereddened V – K colour can be accurately calculated. To determine the temperature the [Fe/H] also needs to be known in addition to the colour. An estimate of [Fe/H] can in some cases be adopted as an average of literature values, however, if the star does not have a well known [Fe/H], a rough estimate can be made based on inspecting its spectrum and looking at the number of lines present. If I have to estimate the metallicity, I will most likely be off by approximately 0.5 dex, which means that I will have to iterate more times in order to determine the stellar parameters. Below I list the values known for HD189558:

Table 4.9: Known values for HD189558, where the parallax (π) is given in arc-seconds and the mass in solar masses.

Star	V	K	π["]	E(B-V)	Mass [$M_\odot$]
HD189558	7.74	6.16	14.76	0.0042	0.76

Based on the many lines present in the spectrum of HD189558 it cannot be very metal-poor, and I assume that the [Fe/H] is $\sim$ -1.0. Calculating the colour, converting filter systems and dereddening at the same time (as described in Section 3.2) V – K in the proper filter (TCS) becomes:

$$V - K_{TCS}^{dereddened} = 0.05 + 0.994 \cdot (7.74 - (6.16 + 0.04)) - 2.72 \cdot 0.0042 = 1.57$$

Now the temperature can be estimated (by using the calibration from Alonso et al. 1996b) with the guess of [Fe/H] = -1.0:

$$T = \frac{5040}{0.555+0.195 \cdot 1.57+0.013 \cdot 1.57^2-0.008 \cdot 1.57(-1.0)+0.009(-1.0)-0.002(-1.0)^2} = 5634K$$

This temperature will change in the later iterations where [Fe/H] is corrected. Since I have an estimate of the temperature and metallicity in addition to the values listed in the table above, I can calculate the gravity once I know ϕ and the bolometric correction, BC according to Nissen et al. (1997):

$$\begin{aligned}\phi &= 2.38619 \cdot 10^{-4} - 1.93659 \cdot 10^{-4}(1.57) + 6.52621 \cdot 10^{-5}(1.57)^2 \\ &- 7.95862 \cdot 10^{-6}(1.57)^3 - 1.01449 \cdot 10^{-5}(-1.0) \\ &+ 8.17345 \cdot 10^{-6}(1.57)(-1.0) - 2.87876 \cdot 10^{-6}(1.57)^2(-1.0) \\ &+ 5.40944 \cdot 10^{-7}(1.57)^3(-1.0) \\ &= 9.60978 \cdot 10^{-5}\end{aligned} \tag{4.6}$$

$$BC = -2.5 \log \tfrac{9.60978 \cdot 10^{-5}}{6.68885 \cdot 10^{-5}} - 0.12 = -0.51$$

and the first gravity estimate becomes:

$$\begin{aligned}\log g &= \log \frac{0.76 M_\odot}{1 M_\odot} + 4 \log \frac{5634K}{5777K} + 0.4 \cdot 7.72 + 0.4(-0.51) + 2 \log(14.76\text{"}/1000 \frac{mas}{\text{"}}) \\ &+ 0.12 + 4.44 = 3.62\end{aligned}$$

where the 7.72 is the dereddened V_0 magnitude ($V_0 = 1.57 + 6.16 - 2.72 \cdot 0.0042$) and the solar values for the temperature (5777K), gravity (4.44) and mass ($1 M_\odot$) have been adopted from the MARCS database (www.marcs.astro.uu.se/). In the equation above the parallax should be inserted in milli-arc-seconds (mas). In order to determine the best possible stellar parameters, I now need to constrain the [Fe/H], which I do by measuring equivalent widths of Fe lines. For this stars I measured equivalent widths of 53 Fe I lines and 8 Fe II lines (all listed in the Appendix Table A.1). To calculate the abundances from these equivalent widths I first need to have a model atmosphere with the proper stellar parameters. I obtain this model by interpolating a grid of models taken from the MARCS model atmosphere database using the code by Masseron (2006) . The parameters I use in the interpolation are T/log g/[Fe/H]/ξ = 5634/3.62/-1.0/1.0, where ξ is the microturbulence velocity, which I for now assume to be 1 km/s. I then run MOOG on a model atmosphere with these parameters and a line list with the necessary atomic data and equivalent widths of the measured Fe I and II lines.

The top panel of Figure 4.11 shows the Fe I abundance (on a log epsilon scale, see Chapter 5 for further explanation) as a function of excitation potential. A slightly negative slope is fitted to the points, which means that it is too easy to excite the lines with low excitation potential. However the slope is very close to being flat, and the temperature will not be altered based on the excitation potentials in this case. The second panel shows

that the microturbulence velocity needs to be increased. This is seen from the positive slope of the fitted line, where the strongest lines (with high log(EW/lambda) which are ξ sensitive) need to yield a lower abundance. By increasing the microturbulence the strong lines will be broadened which in turn will decrease their abundances. The gravity is seen to fulfil ionisation equilibrium, since the log epsilon (Fe I) = 6.32 $\pm$ 0.08 and log epsilon (Fe II) = 6.37 $\pm$ 0.08 agree (within the error). This translates into a [Fe I/H] = -1.20,

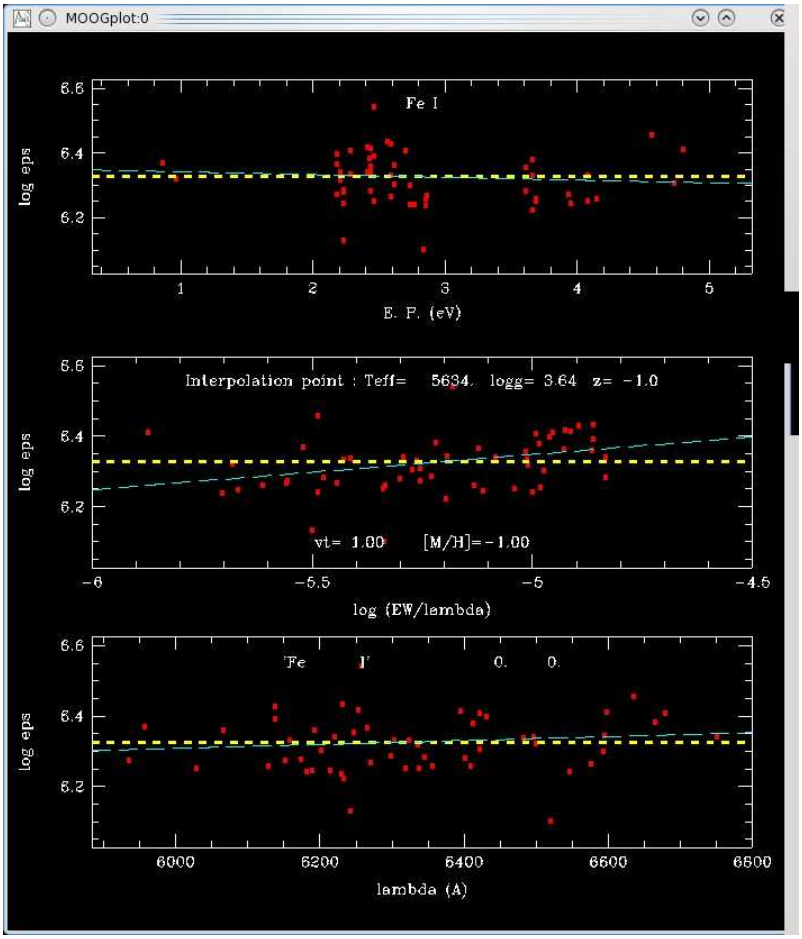

Figure 4.11: The figure shows three output panels from MOOG, where the upper panel shows abundance (on log epsilon scale) as a function of excitation potential. The blue line is fitted to the measurements of the Fe lines and zero slope indicates a well restricted excitation temperature. The slope of the blue dashed line in the second panel indicates how well the microturbulence is determined, since this parameter should be adjusted so that all Fe lines give the same abundance independent of strength. The bottom panel shows the abundance of the Fe lines as a function wavelength and helps remove biases from the Fe line list, so that either very red or very blue lines do not consistently provide too low or too high abundances.

which means that the actual [Fe/H] is 0.2 dex lower than estimated. In order to obtain the correct temperature, [Fe/H], and microturbulence I need to adjust the parameters and calculate all these again. However, since the parameters are interdependent, the gravity will also change when the other parameters are altered. By continuing the iterations until the slope of the microturbulence velocity is numerically less than 0.01 and calculating the gravity and temperature with the new [Fe/H], the final parameters of HD189558 become:

Table 4.10: The final stellar parameters of HD189558.

T	log g	[Fe/H]	ξ
5712 K	3.79	-1.18	1.2 km/s

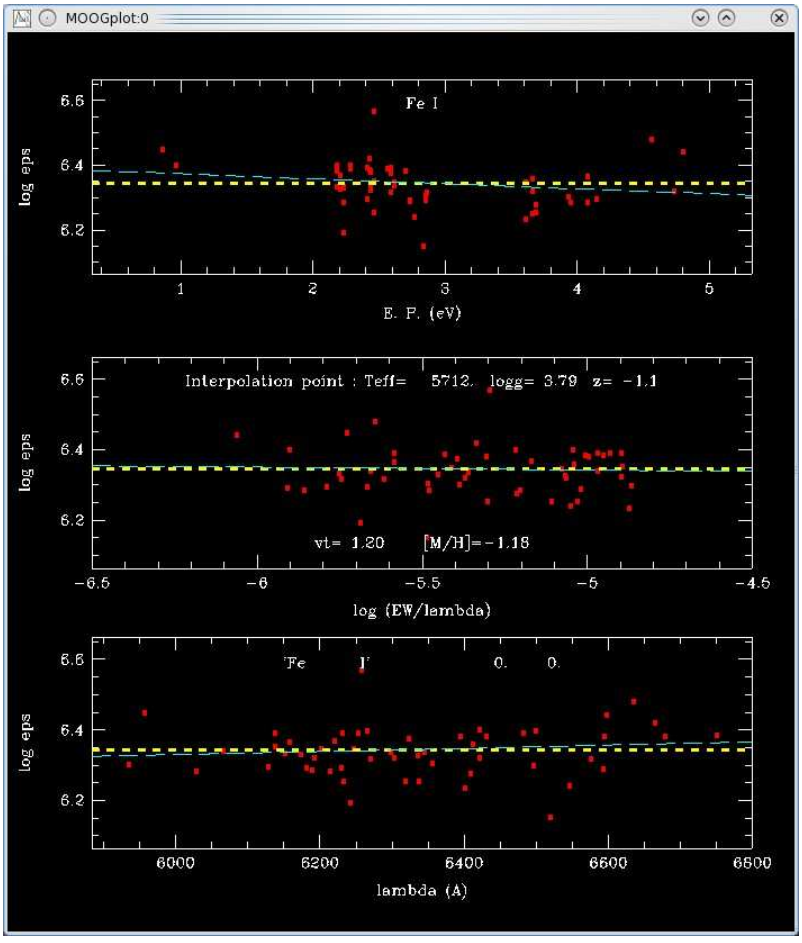

Figure 4.12: The very flat blue lines indicate that the temperature and the microturbulence is well determined.

This set of parameters calculated with the above mentioned formulae is also seen to fulfil excitation equilibrium (see Figure 4.12), since the slope in the top panel is close to being flat (-0.015 i.e. below the limit of ± 0.016 which I accept). The microturbulence is well determined (the slope is -0.008) and furthermore log epsilon (Fe I) = 6.32 ± 0.07 and log epsilon (Fe II) = 6.38 ± 0.08 agree within 0.1 dex i.e. the ionisation equilibrium is fulfilled as well. The log epsilon (Fe I) corresponds to a [Fe/H] = -1.18.

Now the abundances can be derived for HD189558. I will illustrate how the silver abundances are obtained. Once the line list of Ag is calibrated, as described in Section 4.4, I can continue deriving the Ag abundances via spectrum syntheses. Such a synthesis needs a model atmosphere with the correct stellar parameters in order to yield the best possible abundances. To optimize the abundance derivation, I take advantage of MOOG being capable of synthesising four abundances simultaneously. I always choose to make one of the syntheses without any silver e.g. [Ag/Fe] = -50, one with a solar ratio [Ag/Fe] = 0.0, another slightly above or below this value and for the final option I choose a large [Ag/Fe] of e.g 0.75 dex. Based on the synthesis that agrees best with the observations, I can then continue synthesising the Ag abundances with a set of four new values that fit the observations even better. An example of a synthesis carried out with MOOG for the 3382 Å line is shown in Figure 4.13.

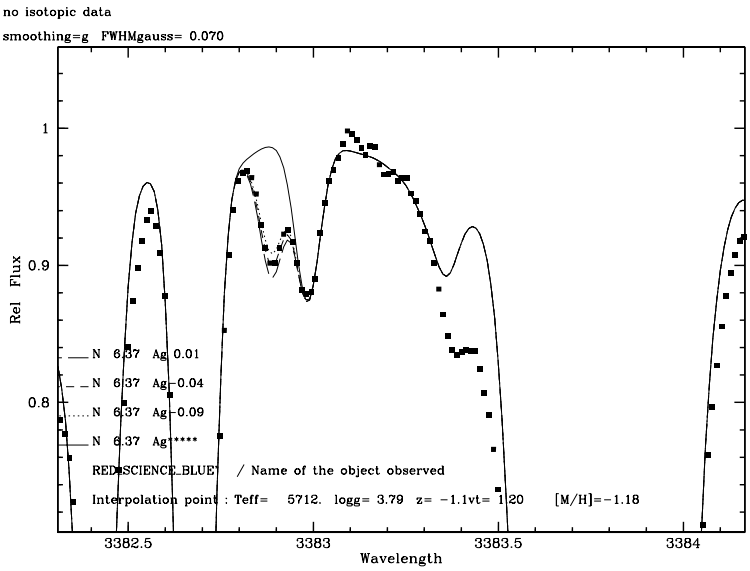

Figure 4.13: Four different Ag abundances ([Ag/Fe] = 0.25 - long dashed, 0.2 - dashed, 0.15 - dotted, -50 - solid) synthesised and compared to the 3382Å line in the observed spectrum of HD189558.

Chapter 5

Results

This chapter presents the first part of my results, which are the observationally derived abundances of the following elements: Sr, Y, Zr, Pd, Ag, Ba and Eu. The elements chosen for this study cover s- and r-process elements. Their correlations and anti-correlations tell us about similarities and differences of their formation processes, and their abundance trends with metallicity describe their evolution as the chemistry of the Galaxy developed. All the abundances presented here have been derived with 1D LTE models.

5.1 Abundances

The abundances discussed in this chapter are mainly given in the notation [X/Fe]. If, for instance X=Ag, this notation describes the number of absorbing silver atoms relative to the number of iron atoms (as mentioned in Section 4.2), scaled to the solar abundances

$$[\mathrm{Ag/Fe}] = [\mathrm{Ag/H}] - [\mathrm{Fe/H}], \tag{5.1}$$

where

$$[\mathrm{Ag/H}] = \log \epsilon(Ag) - \log \epsilon(Ag)_{\odot} \tag{5.2}$$

and

$$\log \epsilon(Ag) = \log(\frac{N_{Ag}}{N_H}) + 12 \tag{5.3}$$

with N_{Ag} and N_H the number densities of absorbing Ag and H atoms. As evident from equation 5.3 I have applied the usual scale where the number of absorbing hydrogen atoms are set to $10^{12}\mathrm{g}^{-1}$. As already mentioned in Section 4.4 all solar abundances adopted are from Asplund et al. (2009). All derived abundances are listed in Table 5.1 and 5.3.

In the following, all elemental abundances are plotted versus [Fe/H] (Figures 5.1 - 5.7) for the entire sample, and all these figures have the same x- and y-range. I have also compared the abundances derived for the elements to the five largest studies, in order to see how my derived abundances compare to previous determinations. The comparison studies are: Johnson & Bolte (2002, J02), Barklem et al. (2005, B05), François et al.

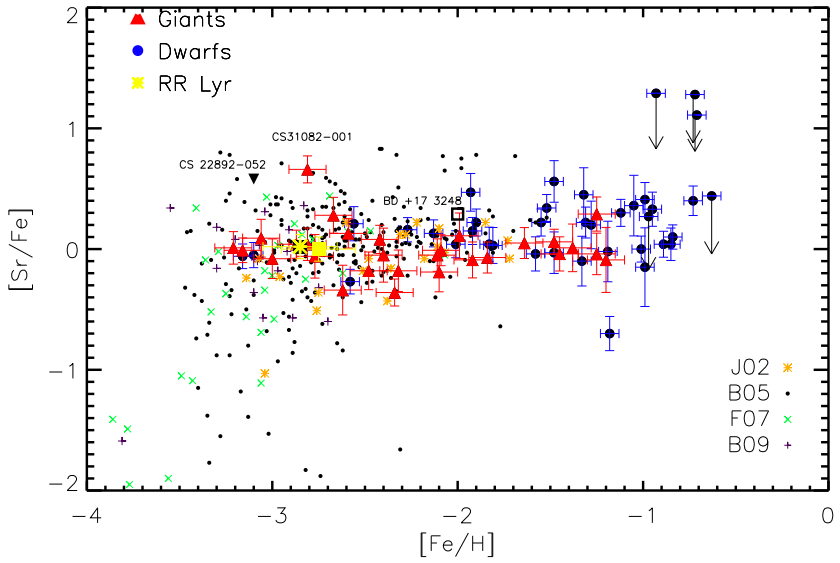

Figure 5.1: [Sr/Fe] plotted as a function of [Fe/H] for my entire sample compared to Johnson & Bolte (2002, J02 - orange asterisk), Barklem et al. (2005, B05 - black dots) and the First stars giants and dwarfs, François et al. (2007, F07 - green ×) and Bonifacio et al. (2009, B09 - purple +), respectively. The dwarfs from my sample are shown as filled blue circles, and the giants are shown as filled red triangles. Three very enhanced stars are shown (with labels) in this and the following figures; BD+17°3248 (Cowan et al. 2002, open black square), CS 22892-052 (Sneden et al. 2003, filled black triangle) and CS 31082-001 (Hill et al. 2002, also analysed in this study, hence the red triangle). A flat trend of [Sr/Fe] is seen down to [Fe/H]∼ -2.5, below which the scatter becomes dominant. The arrows indicate upper limits of the abundances. The Sr abundances for the three 'metal-rich' and seemingly Sr enhanced stars are upper limits, and proper detections could lower their Sr abundances.

(2007, F07), Bonifacio et al. (2009, B09) and Roederer (2009, R09). Throughout this study giants have been plotted as red filled triangles and dwarfs as blue filled circles. In the following figures two RR lyrae stars[1] are shown as yellow asterisks. Despite the very evolved stage and variability of these stars (Hansen et al. 2011b, A&A accepted) have shown that the abundances do not change because of the stellar pulsation, but that these stars are viable chemical tracers as dwarfs, giants and stable horizontal branch stars are. Below I will describe the figures chronologically, Section 5.2 shows the abundance trends, and in Section 5.3 I will enter a discussion on the physics and the outcome of these figures, while Section 5.4 contains the summary.

[1]Since these two stars are not the main part of the thesis the accepted A&A paper has been included in the appendix.

Figures 5.1 to 5.7 show that this study follows the same trends as seen in the comparison samples. The similarity in abundances confirms the values I derived and strengthens the trends I find in these and later plots. In the majority of the figures I find flat trends

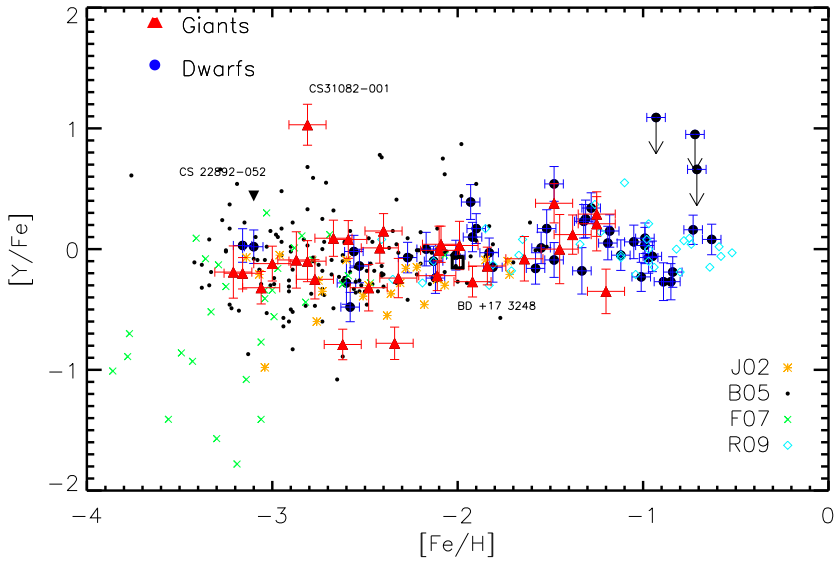

Figure 5.2: [Y/Fe] shows almost no variation with metallicity down to [Fe/H]$\sim$ -2.5 dex. The first three comparison samples are the same as described in the text and in Figure 5.1, but the fourth sample is that of Roederer (2009, R09) - shown as blue open diamonds. The enhanced stars agree with the other comparison samples as well as my sample. However, CS 31082-001 is seen to be particularly enhanced in this light element (Y).

with decreasing metallicity down to [Fe/H] $\simeq$ -2.5. Strontium, yttrium and zirconium show flat trends, the latter two with relatively low scatter (above [Fe/H] = -2.5) compared to what the remaining heavier elements show. The trends seen in Figure 5.1, 5.2 and 5.3 agree with those from Johnson & Bolte (2002); Barklem et al. (2005); François et al. (2007); Bonifacio et al. (2009).

Figure 5.1, showing [Sr/Fe], is seen to have more data points statistically speaking (i.e. abundance measurements) compared to Figure 5.2 and 5.3 (showing [Y/Fe] and [Zr/Fe], respectively). This is due to strontium showing strong resonance lines even in very metal-poor stars, which is not the case for yttrium and zirconium (c.f. log gf in Tables 4.2 - 4.3). All three elements are s-process elements (Arlandini et al. 1999) at solar metallicity, Sr should furthermore be a weak s-process element according to Heil et al. (2009) and Pignatari et al. (2010), Y and Zr experience some contributions from the weak s-process (Pignatari et al. 2010). One could expect to see a difference in trend with increasing metallicity, as the red and asymptotic giant branch stars would start producing additional amounts of these elements compared to that yielded by SN II, but this is not seen. It is not

possible to draw a clear conclusion about the onset of the weak s-process from these plots. However, the homogeneity seen in Figures 5.1 - 5.6 above [Fe/H] = -2.5 dex could be an indication of AGB stars taking over and dominating the main contribution of gas to the ISM and this gas would either be well mixed in the ISM or mainly consist of very similar contributions from the individual AGB stars. In every abundance plot the solar value can be found at zero ((0,0) - [element/H] = 0) and in all of the above mentioned figures, the averages of the abundances are seen to be slightly above the solar value except from yttrium ($[Y/Fe]_{average} \sim$ -0.1). Yttrium has an odd atomic number (Z = 39), and when compared to supernova model predictions, a very low abundance is always found. This is to date still not understood. A too high solar abundance could explain the low abundances. However, for yttrium, the photospheric and meteoritic abundances agree within 0.04 dex making the applied solar abundance trustworthy. Y and Zr are the least scattered elements of the heavy elements studied here. Figures 5.1 and 5.2 indicate that there are three of the more metal-rich ([Fe/H] $\sim$ -0.7,-0.9) dwarf stars (HD175179, HD195633 and G005-040), which have large Sr and Y abundances, but these are in fact only upper limits. This is due to the fact that these stars did not have spectra covering the range ∼3800-4800Å available in the archive, which means that it was not possible to derive the abundances from the strong resonance line of Sr or the cleaner visual lines of Y. This leads to very few equivalent width measurements of Sr and Y (one and two lines respectively) of lines that are most likely affected by unknown blends, which can be quite severe at these metallicities and this in turn caused the large abundance ratios (upper limits) of these three stars.

All figures presenting abundances of heavy elements compared to [Fe/H] have two com-

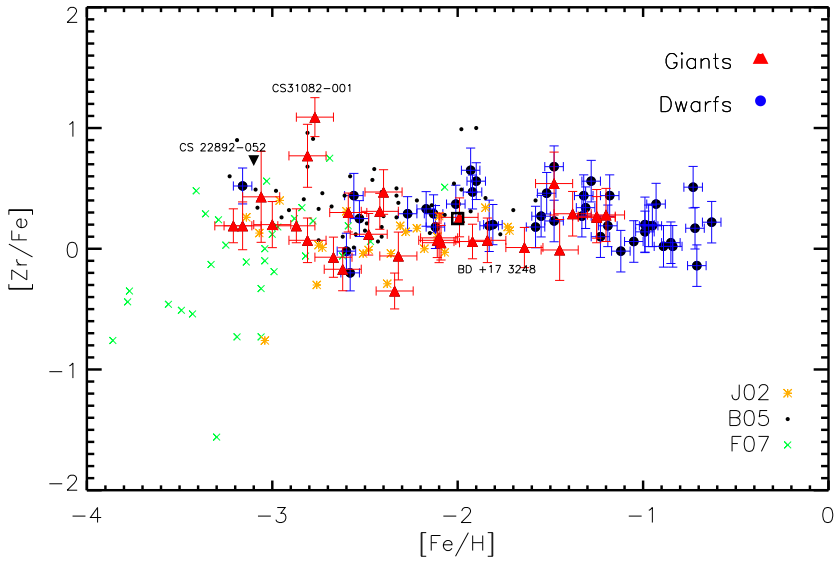

Figure 5.3: Zr shown as a function of [Fe/H]. Zr does not vary with metallicity. The dwarfs and giants follow the abundance trends from the comparison samples. The origin of these samples is explained in the legend and in the caption of Figure 5.1.

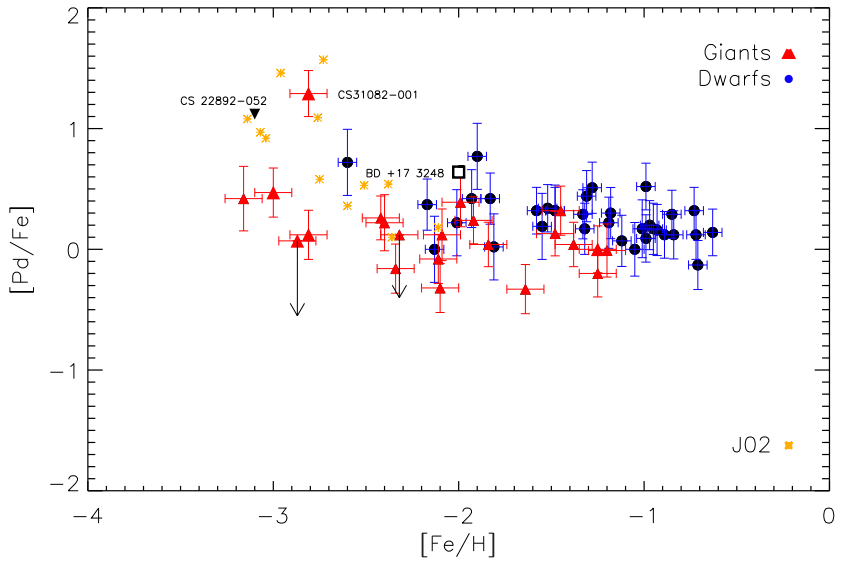

Figure 5.4: [Pd/Fe] as a function of [Fe/H]. A flat trend is seen in this figure. The samples compared differ from the previous plots, and all the stars from J02 seemingly enriched in Pd are upper limits. The additionally enhanced stars from Cowan et al. (2002); Sneden et al. (2003), BD+17°3248 and CS 22892-052 were also added and indicated with labels in the figure. These stars are enriched in r-process elements as is CS 31082-001 from Hill et al. (2002) (as described in Section 1.4). Generally, the stars enriched in r-process elements are indicated by slightly larger symbols.

mon features; the very r-process enhanced star CS 31082-001 (Hill et al. 2002) is indicated by name in the figures and a very large star-to-star scatter is seen around and below [Fe/H] $\sim$ -3. The abundances of CS 31082-001 together with other r-process enhanced stars fall in the upper range but generally agree with those of the chemically not enhanced stars. Two other enhanced stars are BD+17°3248 and CS 22892-052 (Cowan et al. 2002; Sneden et al. 2003), where the enhancement of BD+17°3248 is lower than that of CS 22892-052. BD+17°3248 agrees well with all the other comparison samples and even though the enhancement of CS 22892-052 is very high, it is still positioned in the upper range of the stellar abundances shown here. CS 31082-001 is seen to be one of the stars with the strongest enhancement in the lighter elements (Sr - Ag), this enhancement pattern is not seen in CS 22892-052 (see e.g. Figure 5.2). This is in agreement with Hill et al. (2002) and Sneden et al. (2003), where they also found a difference in the enhancement pattern of these two stars. The large sample from Christlieb et al. (2001b) and Barklem et al. (2005) shows a large star-to-star scatter at the lowest metallicities presented in the plots (as described in the Introduction). The abundances derived for our sample's stars reflect the star-to-star scatter for the heavy elements but not to the same extent for Sr - Zr. In order to detect a larger scatter in the abundances of the lighter elements, more extremely metal-poor stars would probably need to be included and investigated. This scatter could

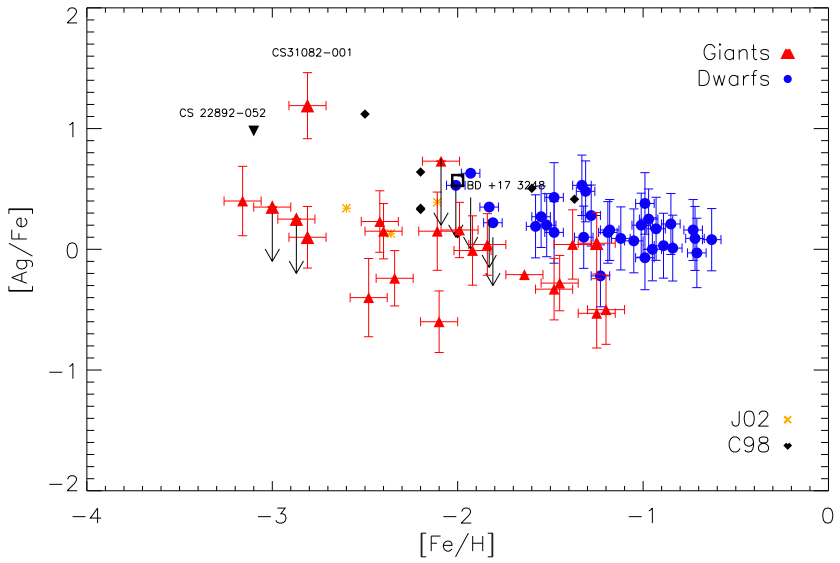

Figure 5.5: [Ag/Fe] versus [Fe/H]. The comparison sample is again J02, and in addition Crawford et al. (1998) - C98, black filled diamonds - was shown to increase the stellar number statistics. All samples show the same flat trend with increasing metallicity.

as stated in the Introduction be an indication of several neutron-capture processes taking place.

Pd and Ag show a relatively large star-to-star scatter around an average value of 0.18 and 0.21 dex, respectively. The scatter for Ag and Pd spans $\sim$ 1 dex and the uncertainties are approximately <0.22 dex, meaning that the scatter exceeds the uncertainties by at least a factor of four. I will investigate the scatter further in Section 5.2 via abundance comparisons, to see which kind of process(es) created Pd and Ag. As mentioned in Section 1.5, only few studies of Pd and Ag can be found in the literature, hence the few comparison stars in Figures 5.4 and 5.5. [Ag/Fe] and [Pd/Fe] do not vary very much with metallicity, indicating that one single process could be responsible for their formation at all metallicities. The [α/Fe] and [O/Fe] abundances show a different behaviour at higher metallicities. Supernovae type II keep yielding both oxygen and α elements as well as iron at all metallicities, whereas SN type Ia start producing a lot of Fe only around [Fe/H] ~ -1.0 Matteucci (2008), therefore a drop in [O/Fe] and [α/Fe] abundances is seen around this metallicity. This is not the case for Ag and Pd. Therefore, the objects creating Ag and Pd must be able to compensate the amount of Fe, thereby keeping the trend flat. Figure 5.4 and 5.5 include r-process enriched giants (slightly larger triangles). In both figures, the r-process enriched stars trace the same trend as the not enriched stars (Hansen & Primas 2011).

Barium and strontium have very strong lines even in metal-poor stars and can therefore be studied in detail down to metallicities around [Fe/H] $\sim$ -4. Barium seems to show varying behaviour with increasing metallicity (Figure 5.6). Starting from low metallicity

(-4.0 < [Fe/H] < -3.0) a very large scatter spanning more than 3 dex is seen. From [Fe/H]$\sim$ -3.2 to $\sim$ -2.2 one can see an increasing trend of [Ba/Fe] with increasing [Fe/H], as well as indications of a relative diffuse but flat trend, creating an intersection of the two trends in the region around [Fe/H] $\sim$ -2.5. Above -2.0 dex in [Fe/H] the trend is flat again. The most metal-poor and metal-rich ranges confirm the findings of François et al. (2007). These trends could indicate, that the main s-process, creating Ba, would start around [Fe/H] $\sim$ -2.5. This agrees with Burris et al. (2000), who predicted that no s-process yields would be found below [Fe/H] = -2.8. Furthermore the scatter seen at low metallicity could, as mentioned in Section 1.4, be explained by an inhomogeneous early Galaxy where, several formation processes might be working. The scatter is not due to observational errors, but is a real indicator of formation processes and homogeneity (as described in the Introduction). Barium and europium show a much larger scatter compared to the lighter elements, which is also seen in the papers by Ishimaru et al. (2004); François et al. (2007). What causes this scatter is still being explored. Europium is one of the elements that have the highest main r-process fraction (94 % main r-process according to Arlandini et al. 1999), and it has therefore been used as a tracer of the main r-process in earlier studies (e.g. Ishimaru et al. 2004) as well as in this study. Due to the very large star-to-star scatter no proper trend can be found in the europium abundance plot (Figure 5.7). This figure does, on the other hand, indicate that there might be a difference between the dwarf and giant Eu abundances.

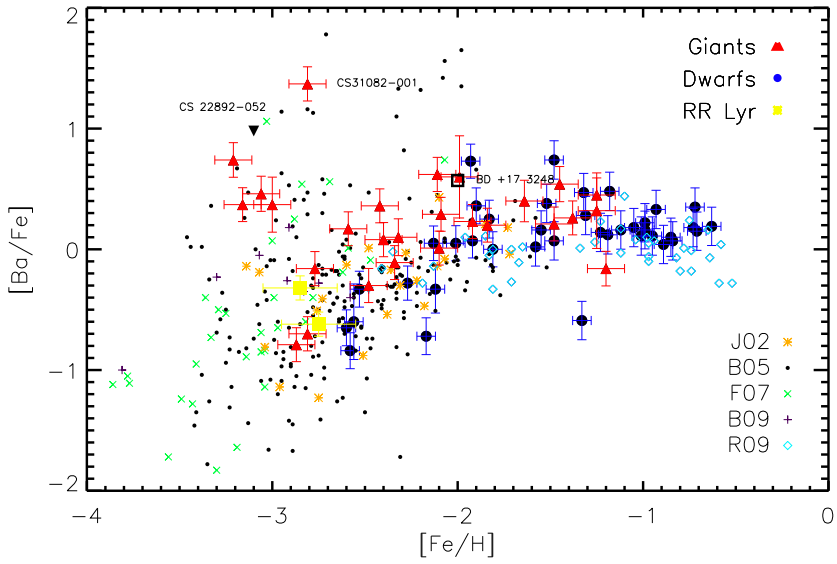

Figure 5.6: [Ba/Fe] plotted versus [Fe/H]. Below [Fe/H] ~ -2.5 a very large scatter in all samples is seen. The samples are indicated in the figure legend and have been described in the three previous figures. The very large scatter at low metallicity ([Fe/H] < -3) can be a sign of a poorly mixed ISM in which the stellar abundances could carry imprint of single supernova explosions, or an indicator of two different processes taking place and yielding very different amounts of Ba (for example).

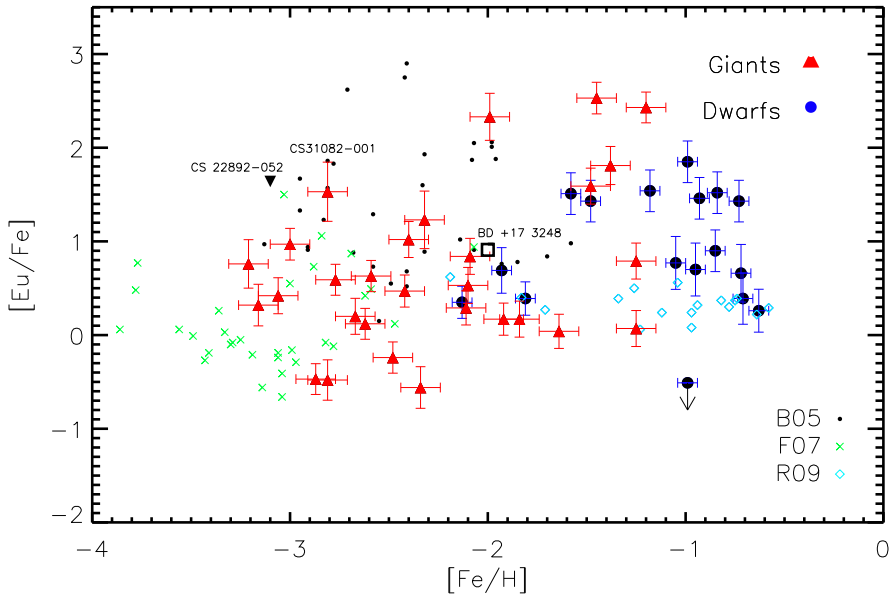

Figure 5.7: [Eu/Fe] as a function of metallicity. A very large scatter is seen at all metallicities (also within the various samples). This is not fully understood, however it can be a combination of line lists (different applied lines) and model treatment of this very heavy element. Especially the heavy elements face problems in models since their atomic structures are far from complete, and hence they are subject to many more approximations than the lighter elements (such as O and Mg) are.

A difference between dwarfs and giants was found in this section, and it was particularly evident for Eu (around [Fe/H] = -1.5), which I will look into in the next section. This difference might be due to non local thermodynamic equilibrium (NLTE) effects or the lack of mixing processes in the models (Eu and Fe might mix differently due to their different masses). Asplund (2005) state that giants (low gravity stars) are normally more affected by the deviations from LTE than e.g. dwarf stars are, which could indicate that the above mentioned difference could also be due to NLTE effects.

Generally flat trends above [Fe/H] = -2.5 were found in the this section's abundance plots. However, below this metallicity large scatters were found. This could indicate that the Galaxy was well mixed after this point, but that the ISM was inhomogeneous below [Fe/H] = -2.5 dex, and that the metal-poor stars were carrying traces of single different supernova events. Hence, in the search of different r-processes it seems to be most likely to find these below [Fe/H] = -2.5. Onsets of various neutron-capture processes were not directly detectable in these figures. However, details will de discussed in Section 5.3. The abundances I derived agree well with the samples compared to and my derived abundances are therefore strengthened. The chemically enhanced stars (e.g. CS 31082-001, CS 22892-

052) show different kinds of enhancement patterns (light versus heavy), but in spite of the enhancement, they seem to follow the same trends as the chemically normal stars.

5.2 Abundance trends

The general behaviour of each of the seven studied elements has now been presented, and a comparison between the elements stemming from slow and rapid neutron-capture processes can now take place - in order to trace the origin of the elements.

In all the figures below (Figure 5.8 to 5.20), abundances of the dwarf and giant stars will be compared. The x- and y-range of the figures are kept the same to ease comparison, except for the figures that include europium, which span a wider abundance range than the other elements.

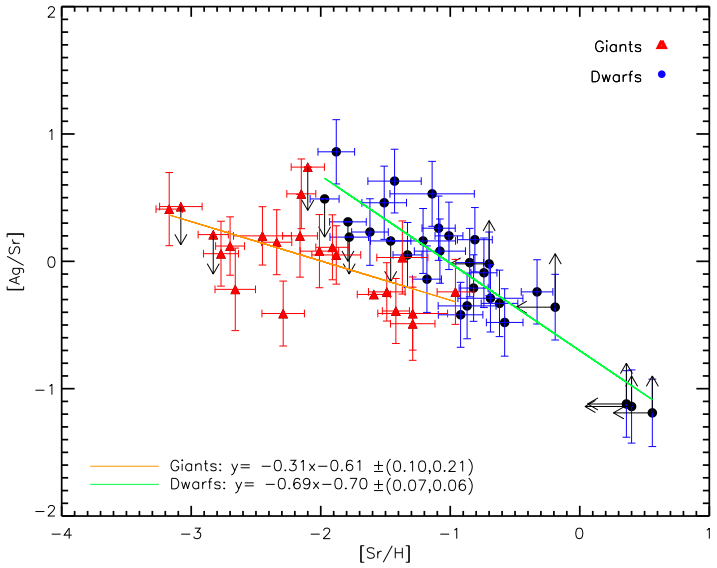

Figure 5.8: [Ag/Sr] as a function of [Sr/H] is shown here for both dwarfs (filled blue circles) and giants (filled red triangles). An anti-correlation is seen in this figure, which is strongest for the dwarfs (see the slopes in the figure). The values given in parenthesis are the uncertainties of the linear fits, the first number is the error on the slope, the second number is the uncertainty of the intersection with the y-axis. The difference between the more metal-rich dwarfs and the more metal-poor giants could indicate different formation processes responsible for creating the abundances. The dwarfs reflect a weak s-process trend, while the giants indicate an r-process contribution. If the Sr abundances would be NLTE corrected, the offset between the dwarfs and the giants would most likely decrease (based on the estimates from Asplund (2005); Belyakova & Mashonkina (1997)).

For clarity, hydrogen was selected as the reference for all ratios on the x-axis. Fe would be the other obvious choice, but selecting Fe would require distinguishing one extra formation process in the abundance plots than the two already present in the ratio shown on the y-axis.

There are two things to keep in mind during these comparisons of the dwarfs and giants. The first is that the difference in the abundances (offset) of the dwarfs and giants could be caused by NLTE effects, and the size of the shift between dwarfs and giants would in turn indicate the size of the LTE deviations. The second and most important reason for the difference between the dwarf and giant stars could be the metallicity range. This is because the detection of silver in the dwarfs is limited to stars with metallicities above [Fe/H] $\sim$ -2.0, whereas the giants can be used as tracers of Ag and Pd down to [Fe/H] $\sim$ -3.5 and below. The dwarfs and the giants can, because of this sample bias, be tracing different processes during the chemical evolution of the Galaxy (e.g. dwarfs will likely trace the s-process while giants might trace the r-process). Both types of stars will therefore provide key information on the formation processes, their evolution and possible onsets of various processes.

Another effect that could cause the difference between the dwarfs and giants, will be mentioned as 'physics' of the stellar model atmospheres, could be atomic diffusion or gravitational settling. This effect describes how heavy elements in the stellar atmosphere sink to the center of the star, thereby changing the surface composition of the star (Salaris et al. 2000; Chaboyer et al. 2001). This settling can be seen to decrease the metallicity of turn-

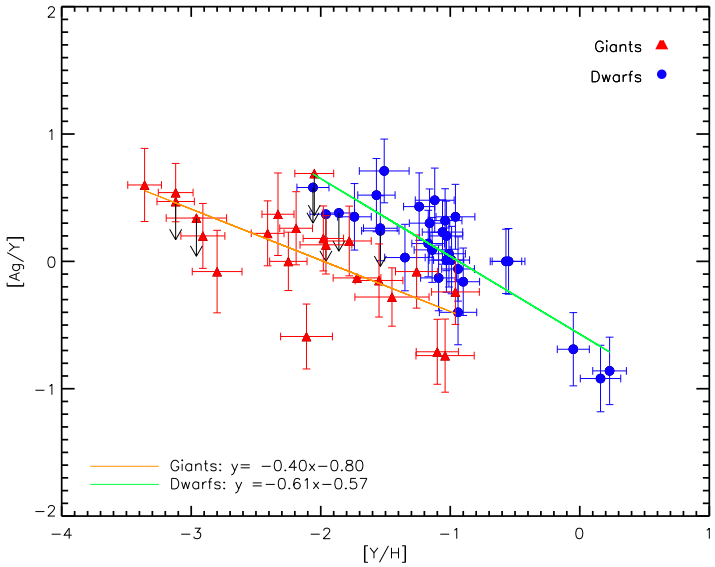

Figure 5.9: [Ag/Y] as a function of [Y/H]. Legend as described in Figure 5.8 and shown in the figure. An anti-correlation between the weak s-process element Y and Ag is seen in this figure.

off stars in globular clusters as well as over estimate the metallicity in dwarf field stars in the halo (Korn 2008). Atomic 'diffusion' was used as the explanation for lithium depletion in evolved globular cluster stars by Korn et al. (2006); Lind et al. (2008). However, Gratton et al. (2001); Mucciarelli et al. (2010) do not support this, they believe that an external mechanism is needed to explain differences between giants and dwarfs of the abundance of the heavy elements. The efficiency of this mechanism is still under debate. The changes it would lead to in the very heavy elements are speculative, and the full explanation for the difference between the dwarf and giant stars is to date not known.

Silver, when compared to the weak s-process element Sr, shows an anti-correlation[2]. In all the figures of this section, linear trends have been fitted to the dwarfs and giants separately. Generally the uncertainty of the trends fitted range from 0.05 to 0.15, with $\sim$0.1 being the most common value. The slopes of the lines are indicated in the figures together with the exact uncertainties. In Figure 5.8 the difference between the dwarfs and the giants is significant.

The NLTE effects depend on the stellar parameters and the Sr lines adopted (Belyakova & Mashonkina 1997). Applying NLTE corrections to the entire sample would seemingly decrease the offset between the dwarfs and giants (according to Asplund (2005); Belyakova & Mashonkina (1997) the corrections of the giants would be $\sim$ +0.3 to +0.4 dex). When looking at the most Sr-poor giant stars, a hint of a flat trend is seen (Figure 5.8), which could indicate similarities in formation processes of Ag and Sr at low Sr abundances ([Sr/H] $\sim$ -3). This could be a sign of a r-process taking place in the early stages of the Galaxy, creating almost equal amounts of Sr and Ag, since [Ag/Sr] seems to lie around 0.0 $\pm$ 0.4 dex (for [Sr/H] $<$ -2).

Now comparing Ag to Y, where Y is another weak s-process element, an anti-correlation is seen from Figure 5.9. As found when comparing Ag to Sr, a difference in [Ag/Y] is seen between dwarfs and giants. This difference could be due to NLTE effects or to our lacking understanding of the underlying physics in model atmospheres and/or synthetic spectrum codes. The difference between the dwarfs and giants is small, which could indicate that e.g. the NLTE corrections of Y are smaller than those of Sr, or that the corrections of Y and Ag counteract each other, however, it is still a significant difference between the dwarf and giant stars, cfr. the slopes in Figure 5.9.

From Figure 5.10 showing [Ag/Zr], the difference in the slopes fitted to the dwarfs and giants is no longer significant (see the uncertainty of the slopes in the figure), and comparing to Figures 5.8 and 5.9 the slopes in Figure 5.10 are close to flat, however a weak anti-correlation is still detectable. This could indicate that Ag and Zr were partly formed by the same process in the early stages of the Galaxy, but at higher metallicities Zr is an s-process element, while Ag is not (Arlandini et al. 1999). The behaviour and role of Zr will be discussed in larger detail in Section 5.3.

An almost flat trend is seen (Figure 5.11) at all metallicities when comparing Ag to Pd including the upper limits and uncertainties of the slopes fitted. The abundances of

[2]An anti-correlation should be interpreted as a tendency which has negative slope, whereas a correlation is seen either as a flat trend or a trend with a positive slope. This was also described in Section 1.4.

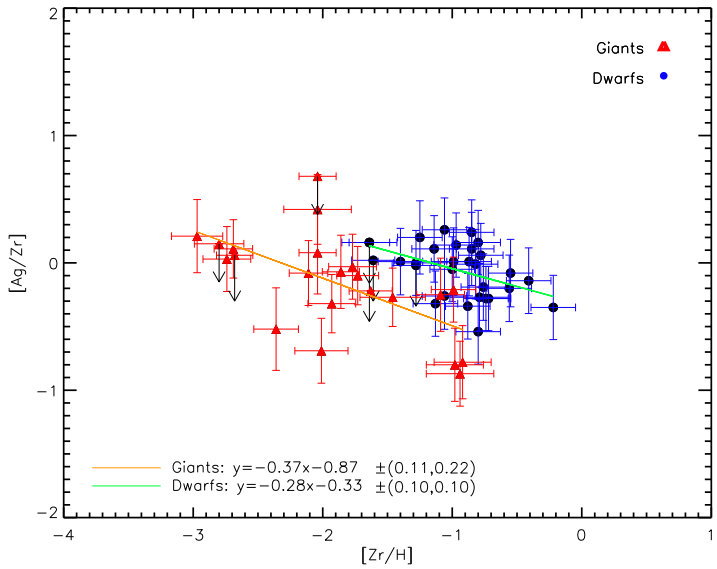

Figure 5.10: [Ag/Zr] as a function of [Zr/H]. A slight correlation could the interpreted from this figure, but the abundances clump. Upper limits for the abundances are indicated by arrows. The formulas of the lines fitted are given in the lower left corner for giants and dwarfs respectively.

Pd and Ag are seen to overlap in giants and dwarfs showing the same trend, which have exactly the same slopes, thus tracing the same process regardless of metallicity and stellar evolutionary stage. Even though the star-to-star scatter is clearly present in this figure (5.11), the scatter is smaller in this plot than in any of the other plots, where Ag is compared to other heavy elements. This supports a similar origin of Ag and Pd.

Barium is a main s-process element, and a comparison of Ag to this element shows an anti-correlation. This can be seen from Figure 5.12. This trend might be more obvious if the stellar sample had included a few stars with [Ba/H] abundances around and below -3.0 dex. However, such stars could also lead to a flattening of the trend, which would mean that Ag would be a main neutron-capture process product at low metallicity ([Ba/H] $<$ -3) as Ba is. A comparison to Eu will help unveiling if this neutron-capture process is a pure main r-process. The horizontal shift between dwarfs and giants is again seen in this Figure (5.6), however, their fitted slopes agree within the error. Applying NLTE corrections might not remove this difference, since the Ba abundances of both dwarfs and giants would increase, according to the values presented in Andrievsky et al. (2009). The corrections vary with metallicity and temperature, so a careful abundance correction must be carried out to contradict or confirm this. A detailed NLTE study of silver would also be necessary to fully understand the [Ag/Ba] behaviour of both dwarf and giant stars. However, in Andrievsky et al. (2009) they conclude that the NLTE corrected abundances of turn-off stars agree well with the abundances of the giants, and they furthermore state

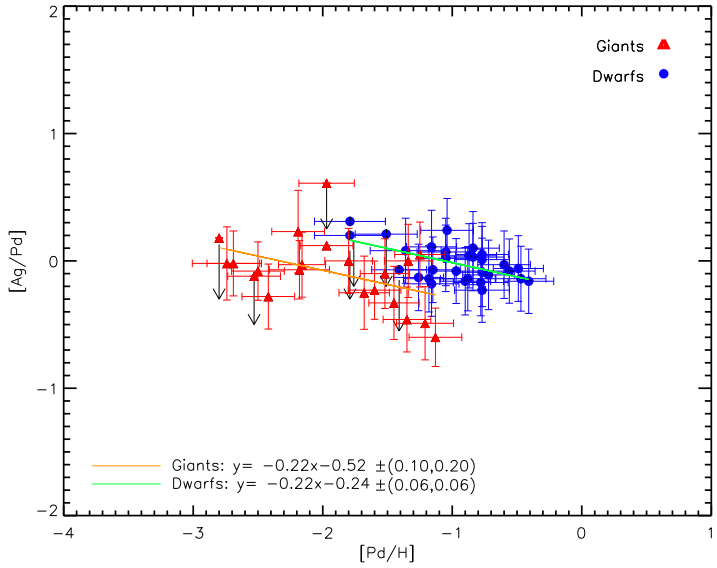

Figure 5.11: An almost flat trend (correlation) is seen in the figure showing [Ag/Pd] as a function of [Pd/H], which is indicative of a similar origin of Ag and Pd.

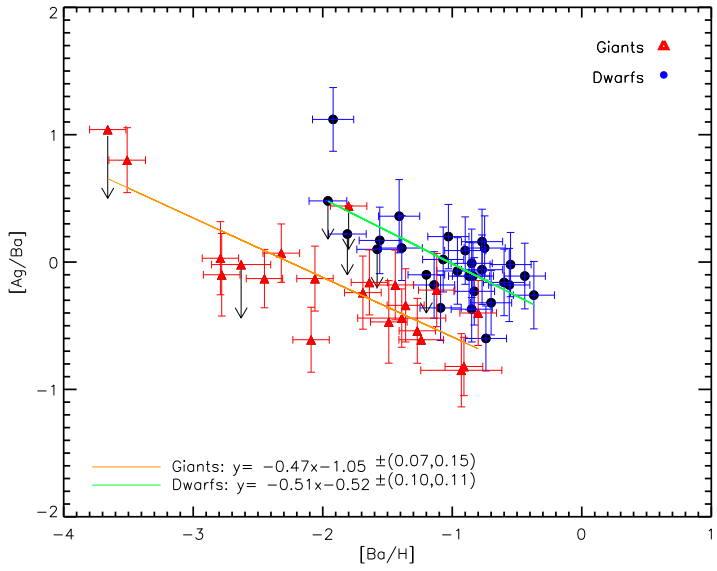

Figure 5.12: An anti-correlation is seen in this plot of [Ag/Ba] versus [Ba/H]. Silver is therefore not a main s-process element.

that Ba does not depend on deep mixing in giant stars, since mixed and un-mixed giants yield the same abundance trends. Therefore, some other physical factor must account

for the shift/difference between dwarfs and giants. An additional indication of different formation processes of Ag and Ba, is the large star-to-star scatter spanning more than 1 dex (see Figure 5.12).

Figure 5.13 shows a very strong anti-correlation between [Eu/H] and [Ag/Eu] (be aware of the difference in x- and y-axis in this figure). It is surprising because Eu is a main r-process element. This trend clearly shows that Ag is not a pure main r-process element. Since Ag is predicted to be 80% r-process produced (Arlandini et al. 1999), and based on the previous comparisons the majority of this element cannot be created by any s-process, but it could very well be a weak[3] r-process element. This will also be discussed in Section 5.3.

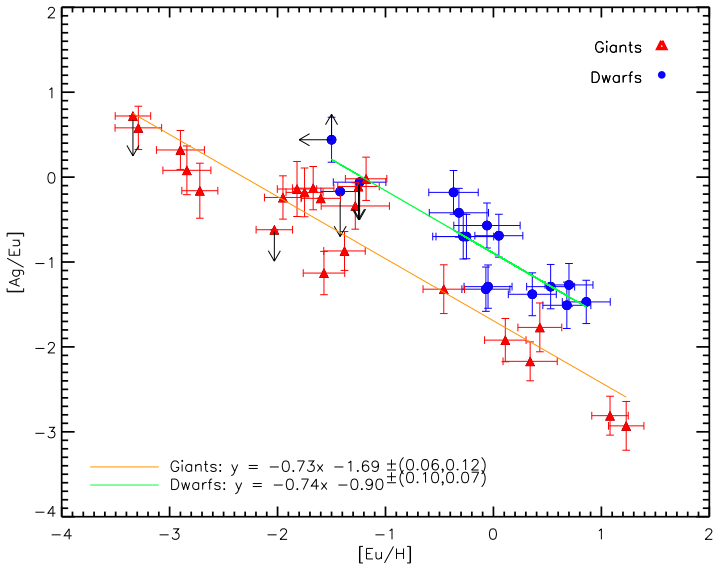

Figure 5.13: [Ag/Eu] plotted as a function of [Eu/H], showing a clear and strong anti-correlation. This means that Ag and Eu are not synthesized by the same process, and silver is therefore not produced by the main r-process.

From Figure 5.8 to 5.13 silver is seen to be created neither by the weak nor the main s-process and is also not by the main r-process. Hence, silver could be a weak r-process tracer. Motivated by Figure 5.11, and later by Figure 5.19, Ag is also seen to be produced by the same process as Pd.

Now I focus on Pd in order to investigate and possibly confirm this statement, I have looked for similar trends when comparing the Pd abundances to the abundances of the other elements. Similar trends will provide strong indications of Ag and Pd being produced by

[3]I will call this process second or weak r-process, in order to distinguish it from the main r-process and indicate that it creates the lighter isotopes (i.e. naming scheme similar to that of the s-process). However, I do not by the use of the name 'weak' to link it to any of the processes suggested by various theory groups such as Kratz et al. (2007); Wanajo et al. (2009); Farouqi et al. (2009).

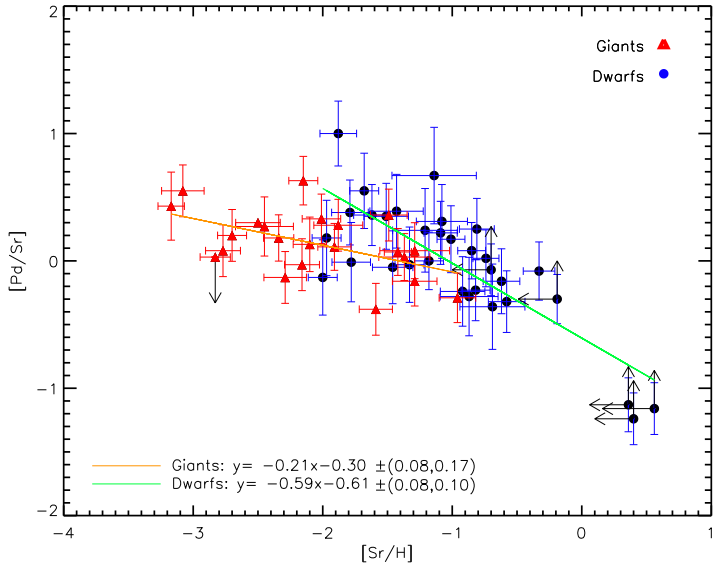

Figure 5.14: An anti-correlation is seen in this figure of [Pd/Sr] versus [Sr/H].

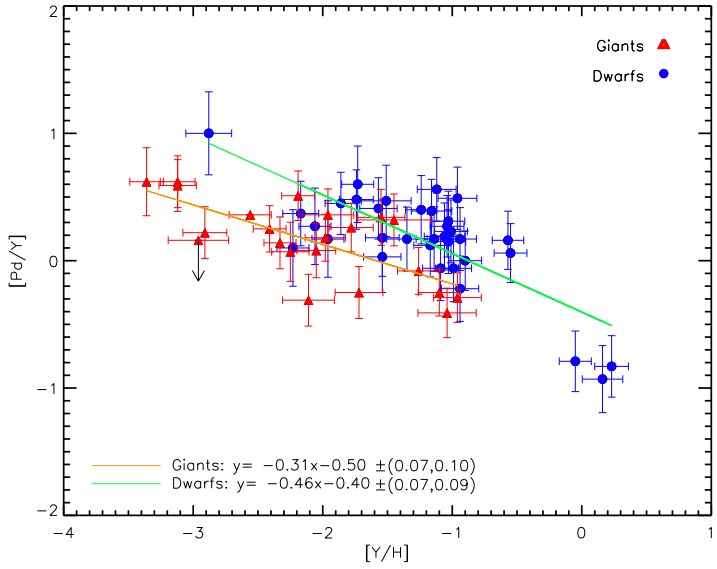

Figure 5.15: [Pd/Y] shown as a function of [Y/H]. An anti-correlation is seen, though abundances in the [Y/H]-range -0.8;0.0 would help strengthen this statement.

the same second/weak r-process. Comparing palladium to strontium and yttrium, anti-correlations are found (Figure 5.14 and 5.15). In these two figures the same three stars as mentioned earlier show artificially large abundances of Sr and Y (i.e. low [Pd/Sr] and

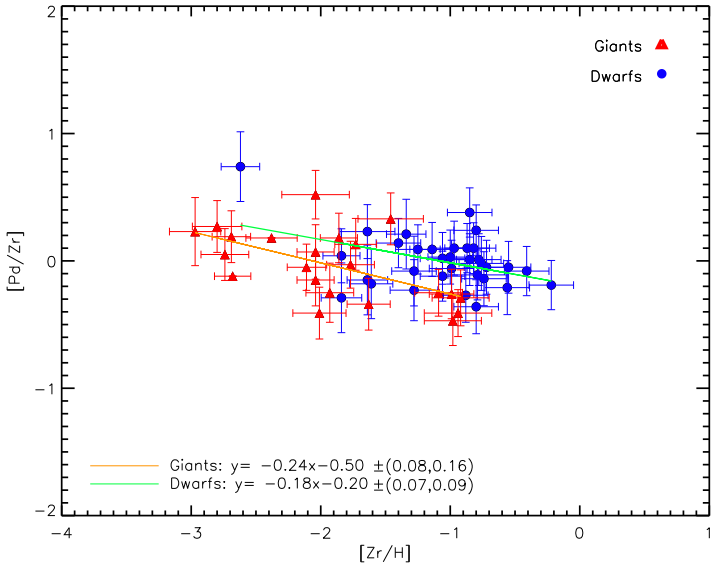

Figure 5.16: Pd and Zr seem to correlate in this figure of [Pd/Zr] versus [Zr/H]. The slopes fitted to both dwarfs and giants are close to being flat.

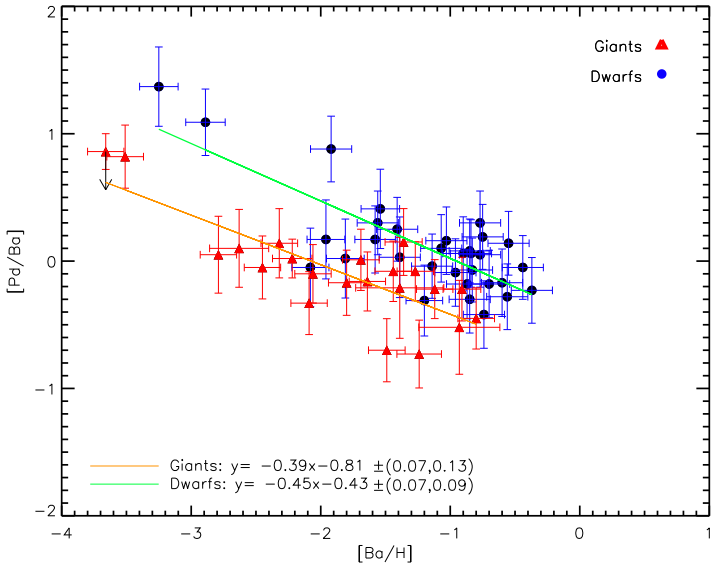

Figure 5.17: [Pd/Ba] as a function of [Ba/H] shows an anti-correlation, as was seen in Figure 5.12. Pd is not a main s-process element.

[Pd/Y]) due to uncertainties in the equivalent width measurements. The dwarfs fall on a line with a negative slope, indicating an anti-correlation even at higher metallicities. The

slope fitted to the giants is slightly less negative than the one fitted to the dwarfs (as in Figures 5.8 and 5.9). This indicates that Pd is not a weak s-process tracer as Sr is. Even though Pd was predicted to be 46% main s-process produced with respect to the Sun (Arlandini et al. 1999), the remaining 54% are clearly not weak s-process created, and the s-process contribution to the Pd abundance is not dominating.

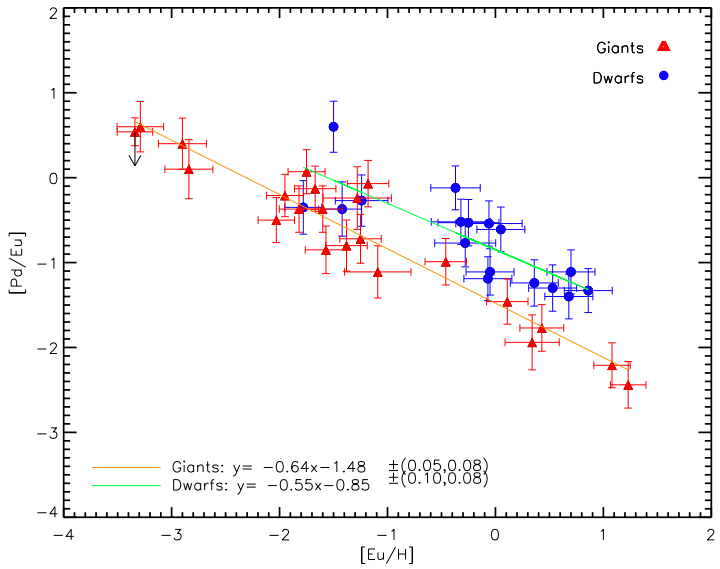

Figure 5.18: From the strong anti-correlation seen in this plot of [Pd/Eu] versus [Eu/H], Pd is seen not to be produced by the main r-process as Eu is. Lines with negative slopes (~ -0.6) are fitted to the dwarf and giant abundances.

Indications of a weak anti-correlation can be seen in Figure 5.16, though considering the error on the slopes ($\pm$ 0.08) the linear trend is almost flat and Pd and Zr seem to correlate. Zr has been predicted to be 82% s-process (Arlandini et al. 1999). Both giants and dwarfs show the same trend and their abundances seem to clump in the centre of the figure. This could indicate that Zr and Pd originate from the same process and that Zr is a transition element, meaning that it bridges from the (weak) s-process to the (weak) r-process. For further discussion see Section 5.3.

Sr, Y and Zr could be created by the same s-process. Farouqi et al. (2009) claimed that elements up to Sr are created by charged particle processes or α-rich freeze out processes, but a weak s-process was suggested by Heil et al. (2009) and Pignatari et al. (2010). There are differences in the trends of Figure 5.14, 5.15 and 5.16, which could indicate that Sr and Y are either created by a charged particle process or a weak s-process, whereas Zr could be created by a second/weak r-process as Pd.

Figure 5.17 shows an anti-correlation of Pd and Ba (slope $\sim -0.4 \pm 0.07$), which shows that Pd is not produced by a main s-process.

[Pd/Eu] plotted versus [Eu/H] shows a striking anti-correlation (Figure 5.18) as seen when Ag was compared to Eu. This means that Pd is not created by the main r-process and that formation process could be a second r-process.

An excellent agreement of Pd and Ag found at all metallicities is seen in Figure 5.19. In Figure 5.19 the least χ^2 fits have been plotted in addition to the [Ag/H] and [Pd/H]

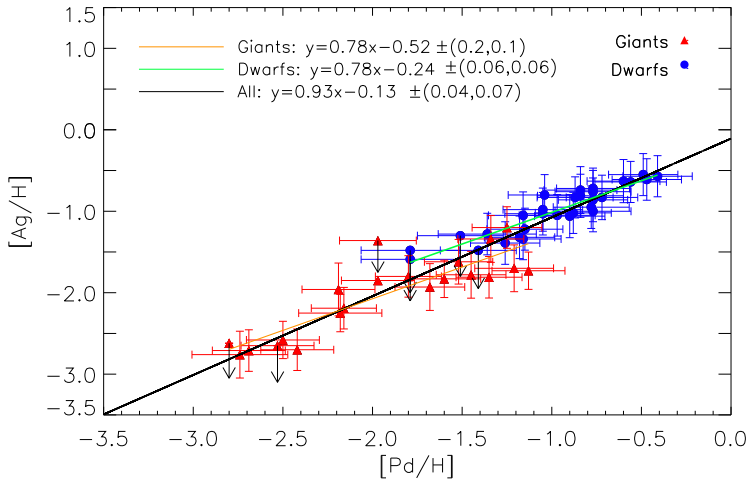

Figure 5.19: A correlation of Pd and Ag is seen in this figure. In order to emphasize this evident agreement, an orange line has been fitted to the giants, a green line to the dwarfs and a black solid line is fitted to all the stars. The slopes of the lines agree within the uncertainty of the fits.

abundances of the dwarfs and giants. The slope of the dwarfs is 0.78±0.1, that of the giants is 0.78±0.1 and the combined slope for both dwarf and giant stars is 0.93 with uncertainty of 0.07. The slope corresponds to the ratio: ΔAg/Δ Pd.
The fact that the slope is less than one can be explained by the growth of Pd being slightly faster than that of Ag. However, the slope is close to one, and the two elements must have the same origin. Despite the difference in predicted s-process contribution of the two elements, a striking correlation to the combined sample of dwarfs and giants is seen at all metallicities in Figure 5.19. This could mean that the r-/s-process ratios are off or that one of the processes is dominating. Now a short comparison of Zr to Sr,Y and Ba will be carried out, in order to see the resemblance of Zr to either weak or main s-process elements.

Figure 5.20 shows that Zr actually correlates with both Sr and Y within a reasonable scatter. Zirconium therefore has something in common with weak s-process elements, but due to the slight correlation with Ag and Pd, Zr could actually be a transition element, of which 83% is s-process produced (Arlandini et al. 1999) and the remaining 17% could be 'weak' r-process created. These 17 % could be dominating in the most metal-poor giants, causing the slight/weak correlation of giant abundances seen in Figure 5.10 and

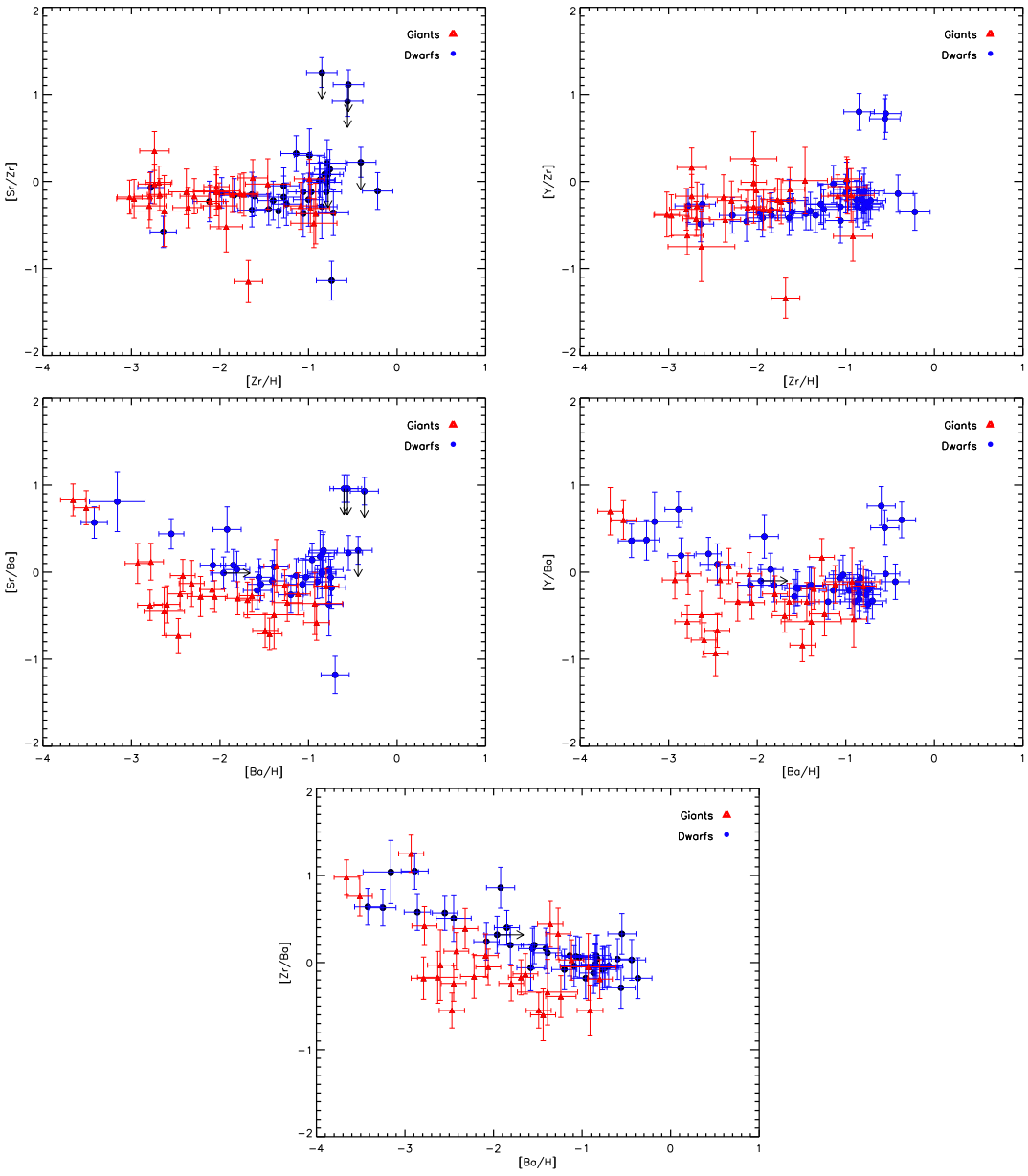

Figure 5.20: The top two figures show how Zr compares to Sr (left) and Y (right), in both cases flat trends are seen (the same three outliers are seen in Figure 5.1 and 5.2). However, when comparing Sr, Y and Zr to Ba in all three cases a decreasing trend with increasing [Ba/H] followed by a flat trend for the largest [Ba/H] abundances. The change in trend takes place roughly around [Ba/H]= -2.5 dex, indicating that the same process could be producing these four elements at higher [Ba/H]. A relatively large scatter is seen above [Ba/H] = -2.5, wherefore contributions from different s-processes can not be ruled out.

5.16. This seems to be confirmed by the comparison of Zr to Ba in Figure 5.20. Figure

5.20 also shows, that Ba does not correlate with either Sr, Y or Zr at low metallicities. A 'weak' r-process might be responsible for partly creating the latter three, whereas Ba should be produced by the main r-process in the early stages. The role of the r-process at low [Fe/H] was emphasized in Section 1.1. Only at higher metallicities do all three light neutron-capture elements correlate with Ba, indicating a common s-process origin at these metallicities (solar to sub-solar; [Ba/H] > -2.3). These trends confirm the findings of François et al. (2007). However, due to the scatter seen when comparing Sr - Zr to Ba, contributions from both a weak and a main s-process seem likely for [Ba/H] > -2.3.

A clear picture of the formation of Pd and Ag has now been presented. It has also been shown, that both dwarfs and giants confirm the findings for Pd and Ag of the same formation process as seen in Figure 5.19, where their abundances clearly overlap in the interval: [Pd/H] = [-1.8;-1.1].

⋆ Conclusions based on the trends from the above shown figures are, neither Ag nor Pd are produced by the main r-, s-process or the weak s-process. A different process must be responsible for their production and this process seems to be working at all metallicities yielding both Pd and Ag.

5.3 Discussion

In this section I highlight my findings and address three main points mentioned repeatedly in the previous section, namely, scatter and inhomogeneities, differences between dwarfs and giants (NLTE effects) and I extract information from the presented abundance trends.

The first point that I will address in this section is the consistently large scatter or ISM inhomogeneity seen at metallicities below [Fe/H]< -2.5 dex in the majority of this chapter's figures. Many of the large abundance studies have found similar large star-to-star scatter at these low metallicities (e.g. Barklem et al. 2005; Preston et al. 2006; François et al. 2007; Bonifacio et al. 2009) and a NLTE follow-up study of the latter carried out by Andrievsky et al. (2009) confirmed that the scatter of Ba was so large even after applying the NLTE corrections to the abundances, that they could not consider the ISM homogeneous. However, the very low star-to-star scatter of alpha and iron-peak element abundances provides a counter argument to this statement (Cayrel et al. 2004; Preston et al. 2006), since these elements would suggest a very well mixed ISM. Based on my findings I would favour an inhomogeneous early ([Fe/H]< -2.5) ISM for the reasons that follow. If we start by considering all these (alpha, iron-peak and neutron-capture) abundances above [Fe/H] = -2.5, all star-to-star scatters are much lower and the ISM seems to be homogeneous. This can be explained by AGB stars being dominant sources, that by their relatively frequent occurrence manage to mix the ISM well thereby producing a homogeneous ISM. However, this is not the case below -2.5 dex in metallicity, where different supernovae explode (this was also suggested by Johnson & Bolte 2002) and due to the different supernova features their yields will vary (see e.g. Heger & Woosley (2002); Wanajo et al. (2003); Kobayashi et al. (2006); Izutani et al. (2009); Farouqi et al. (2009); Wanajo et al. (2010) where they discuss the impact various parameters such as

peak temperature, mass-cut and entropy have on the SN yields). The alpha elements are mainly produced by supernovae type II, i.e. SN II are the dominant source of the alpha-elements. Yet the exact site of the neutron-capture elements is not known, and different neutron-capture elements might be created at different site (Johnson & Bolte 2002), hence, the lack of one dominating source could cause the large scatter. Furthermore, the different supernovae that create the neutron-capture elements could due to their differing nature enable different neutron-capture processes, i.e. a main and a second r-process which would help explain the scatter. Simply put, the inhomogeneity could be explained by several sources/sites yielding different amount of the neutron-capture elements, whereas the alpha-elements are dominated by SN II yielding relatively similar amounts of these elements.

The difference of these processes stand out rather evidently from Figures 5.13 and 5.18, where the strong anti-correlation between Ag and Eu and Pd and Eu are seen. Europium is created by the main r-process, a process that requires very high neutron number densities to produce Eu (typically around 10^{26-28}, Kratz et al. 2007) whereas the lighter isotopes of e.g. Pd can be created in environments with densities that are lower by several orders of magnitudes. It is not possible to create Eu in environments with such low neutron densities (Kratz et al. 2007; Farouqi et al. 2009; Wanajo et al. 2010). This suggests that features of the formation sites of the heavy and the light r-process isotopes differ. Figure 5.11 indicates that the process creates both Ag and Pd and at almost the same rate, which is seen from the slope of dwarf and giant stars being close to one (see Figure 5.19). Since the line fitted to the Ag and Pd abundances in this figure is straight all the way down to [Fe/H] = -3.3 without break, the process seems to be working efficiently at all metallicities down to this value. This process or the production site must be less efficient than the main r-process. For [Eu/H]> -3 the [Ag/Eu] is below zero and rapidly decreasing with increasing Eu (see Figure 5.13). However, at the lowest metallicities and europium abundances ([Eu/H] < -3) the amount of Ag is at the same size or slightly larger than the Eu abundance, which is seen from the [Ag/Eu] abundance being larger than zero. The same is seen from Figure 5.18. This could indicate that the second r-process is more efficient at low [Eu/H]. It cannot be ruled out that Ag and Pd receive small contributions from the main r-process, since it is generally ([Eu/H]>-3) dominating the gas in the ISM. Figures 5.8, 5.14, 5.12 and 5.17 show anti-correlations of Ag and Pd compared to Sr and Ba. At high metallicities, [Fe/H]$\sim>$ -1, the s-process is dominating the ISM compared to the second (weak) r-process (e.g. [Ag/Ba] < 0). However, the same figures show abundance ratios around 0 in a metallicity interval, [-2.5;-1]. This could indicate that the s-process and the second r-process have some features in common, which could be an expression of the lower neutron density they both work at or other characteristics of the second r-process that has yet to be confirmed. Based on this study, it might be more fruitful to look at the s-process when searching for answers to the nature of the second r-process, than looking at the main r-process.

Another important outcome of this study was the discovery of Zr as a 'transition' element. From Figure 5.8 to 5.10 showing Ag compared to Sr, Y and Zr, a gradual increase in slopes is seen i.e. an expression for the growing similarities of their formation processes. The same is seen for Pd compared to Sr, Y and Zr (Figures 5.14 - 5.16). Within the errors

on the slopes, Ag and Pd almost correlate with Zr. When Ag and Pd are compared (Figure 5.11) a close to perfect correlation is seen. This could be the first observational evidence which at higher metallicities [Fe/H]> -2.5 show that Sr and Y are weak s-process products as claimed by Heil et al. (2009); Pignatari et al. (2010) whereas Zr which should mainly be an s-process element, actually receives considerable contributions from a type of r-process. This r-process is responsible for the main production of Pd and Ag. The transition from weak s- (Sr, Y) to 'weak' r-process (Pd, Ag) takes place around Zr (Z=40), hence the name transition element. However, the figures showing [Ag/Ba] and [Ag/Eu] show anti-correlations (the latter strong, see Figure 5.13) meaning that the formation processes differ. The anti-correlation with Ba shows that this process is not a main s-process and the strong anti-correlation with Eu demonstrates the differences of the main and the second r-process. The transition of the second (weak) r-process to the main r-process, should be found among the heavier isotopes was not directly revealed here. However from the anti-correlation of Ag and Ba seen at low metallicities [Fe/H]< -2.5, the weak/second r-process must stop creating elements with atomic numbers less than that of barium (Z=56).

Finally, the differences between dwarfs and giants need to be discussed. Unfortunately, a full NLTE analysis is due to incomplete and complicated model atoms of these heavy elements not yet possible and is furthermore outside the scope of this thesis. However, based on previous studies of some of the heavy elements such as Sr and Ba (Belyakova & Mashonkina 1997; Andrievsky et al. 2009) the NLTE corrections can be relatively large for low gravity metal-poor stars, and the Sr abundance could need corrections on the order of ~ 0.4 dex. These corrections are very dependent on the stellar parameters and would therefore vary from star to star. Additionally, it is not sufficient to only correct one of the elements in the abundance ratios, both elements need corrections to obtain the correct abundances. This means that still a lot of work has to be done in order to correct five out of the seven elements studied here. This indicates that an LTE study is as accurate as abundance studies of heavy elements get to date. Any estimate of the behaviour of the NLTE corrections of e.g. silver would be very speculative, however, from Figure 5.12 the [Ag/Ba] ratio of the giants would need an NLTE correction of $\sim +0.5$ dex estimated from the offset in the figure. The study has been carried out in a very homogeneous way, the same colour-temperature calibrations have been applied to both the dwarfs and the giants, and similar methods were applied to derive gravity, metallicity and microturbulence for these stars, which makes it very unlikely that such a large difference between the dwarfs and giants should be connected to the analysis of these stars. The same lines were studied for both dwarfs and giants, both regarding Fe and the neutron-capture elements, which makes it more likely that the offset between these two groups of stars, would come from assumptions in the models (e.g. NLTE), since these corrections can be quite large (e.g. for Sr ΔNLTE $\sim>$ 0.3 or larger Asplund 2005; Belyakova & Mashonkina 1997).

5.4 Summary

I have conducted an abundance study of 73 stars, all of high-resolution echelle spectra which I reduced, and these allowed this detailed study of Ag and Pd. These two elements have never been studied in such a large homogeneously analysed sample before, which has lead to unprecedented indications on the origin of silver and palladium. I derived silver and palladium abundances in 56 stars which almost tripled the number of stars with known Ag and Pd abundances. This is an important step forward in this field, and it is needed in order to unveil the neutron-capture origin of these elements, which needs a statistically sufficient number of abundance derivations in order to make conclusions on such findings.

Silver and palladium have been compared to five other elements, including two weak s-process elements (Sr and Y) as well as main s- and r-process elements (Ba and Eu), respectively. The outcome of the trends found in this chapter's abundance plots is the following: Silver and palladium appear to be produced by the same process (Hansen & Primas 2011), and this process is neither a main s - nor main r-process. The formation process of Ag and Pd is also not a weak s-process, however, the formation process could be a second (weak) r-process. A slight correlation or resemblance is seen when comparing these two elements to e.g. Zr. This could be because the weak s- and r-process have common features such as similar neutron densities, leading to similarities in the abundance output pattern. Furthermore, the similarity of Ag, Pd and Zr could be explained by Zr being a transition element, of which parts are made by the weak s-process and parts by the 'weak' r-process.

The trends of the heavy elements' abundances seen when compared to [Fe/H], are the following: The abundances I derived generally fit those found in the comparison samples, and except for Eu all the elements show a flat trend at higher [Fe/H] (> -2.5) followed by a drastically increasing scatter (> 2 dex) with decreasing metallicity ([Fe/H]$<$ -2.5). The increasing scatter of the heavy elements is partly an indicator of how well the ISM was mixed at that time, but it also provides information on how uniform the yields of the formation processes forming the elements early on were. The star-to-star scatter is far too big to be removed with NLTE corrections (Andrievsky et al. 2009), and provides a clear indication of multiple formation processes taking place and creating an inhomogeneous early ISM. This means that the early Galaxy (in the interval -4 $<$ [Fe/H] $<$ -3 dex) was not well mixed. The fact that some elements show a very low scatter can be explained by their production being generally of the same size and furthermore dominated by only one type of object (see Section 5.3). The onsets of s- and r-process were not directly detectable from the figures with [Fe/H] plotted on the x-axis, however, they were visible in the other abundance plots including only the heavy elements. These figures provided the following information:

- The second/weak neutron-capture (r-process) elements are seen at low metallicity (below [Fe/H]~ -2.0) (see e.g. Figure 5.13, 5.17,5.18 and 5.20), whereas weak s-process elements are most evidently detected from [Fe/H]$\sim> -2.5$ (Figure 5.20).

- The main s-process seems to dominate and homogenise the s-process abundances at a [Ba/H] $\sim>$ -2.5 (e.g. Figure 5.6 and 5.20).

I find two r-processes reacting simultaneously from the early stages to recent times (-3.3 $<$ [Fe/H] $<$ -0.6), i.e. starting from a much higher metallicity than predicted by Lai et al. (2008).

The second/weak r-process appears to take place at all metallicities, at least down to [Fe/H] $\sim$ -3.3. However, in order to confirm the universality of the weak r-process, or find the very early onset of this process, more r-process enhanced ultra metal-poor stars with high signal-to-noise spectra are needed.

Generally, the dwarfs and giants predict the same trends for Zr - Ag, despite being slightly shifted, either due to NLTE effects or due to e.g. atomic diffusion, i.e. insufficient understanding of the stellar atmospheres. Dwarfs and giants show different trends for [Pd,Ag/Sr] and [Pd,Ag/Ba] i.e. tracing different processes at low and high metallicities (Hansen et al. 2011c in prep.). A slightly lower scatter for [Ag/Pd] was derived here compared to what Johnson & Bolte (2002) found. The difference in scatter is in part due to fact that they mainly found upper limits for Pd, but other reasons could be the difference in line lists and atomic data, which could also explain the lower odd-even effect I obtained compared to them.

The abundances of all described elements will in the next chapter be compared to two different model predictions (Kratz et al. 2007; Wanajo et al. 2010) to see, if this second r-process can be connected either to a SN wind (Kratz et al. 2007; Farouqi et al. 2009) or to a low mass O-Ne-Mg SN as described in paper by Wanajo et al. (2003, 2010).

Table 5.1: Stellar abundances of Fe, Sr, Y, Zr, Pd, Ag, Ba and Eu for dwarfs. The $'<'$ indicates that the abundance is an upper limit.

Star	[Fe/H]	[Sr/Fe]	[Y/Fe]	[Zr/Fe]	[Pd/Fe]	[Ag/Fe]	[Ba/Fe]	[Eu/Fe]
BD+09 2190	-2.60	–	-0.28	-0.02	0.72	–	-0.65	–
BD-13 3442	-2.56	0.21	-0.02	0.44	–	–	-0.60	–
CD-30 18140	-1.92	0.15	0.1	0.47	–	–	0.07	–
CD-33 3337	-1.55	0.22	0.01	0.27	0.19	0.27	0.16	–
CD-45 3283	-0.99	-0.15	0.03	0.14	0.52	0.38	0.22	1.85
CD-57 1633	-1.01	0.00	-0.23	–	0.17	0.20	0.11	–
HD3567	-1.33	-0.1	-0.18	0.27	0.29	0.53	-0.59	–
HD19445	-2.13	0.13	-0.1	0.29	0.00	–	0.05	0.35
HD22879	-0.95	0.33	-0.06	0.19	0.17	0.00	0.11	0.70
HD25704	-1.12	0.30	-0.05	-0.02	0.07	0.09	0.16	–
HD63077	-1.05	0.36	0.06	0.06	0.00	0.07	0.18	0.77
HD63598	-0.990	0.41	0.09	0.20	0.09	-0.07	0.16	<-0.51
HD76932	-0.97	<0.27	-0.07	0.19	0.20	0.25	–	–
HD103723	-0.85	0.04	-0.27	0.05	0.29	0.21	0.10	0.90
HD105004	-0.84	0.10	-0.19	0.02	0.12	0.01	0.07	1.52
HD106038	-1.48	0.56	0.54	0.68	0.32	0.14	0.74	1.43
HD113679	-0.63	<0.44	0.08	0.22	0.14	0.08	0.19	0.26
HD111980	-1.32	0.45	0.23	0.44	0.17	0.10	0.47	–
HD116064	-2.17	–	0.00	0.33	0.37	–	-0.72	–
HD120559	-1.31	0.22	0.25	0.34	0.44	0.48	0.28	–
HD121004	-0.73	0.40	0.16	0.51	0.32	0.16	0.18	1.43
HD122196	-1.81	0.03	-0.15	0.20	0.02	<0.22	0.00	0.39
HD126681	-1.28	0.20	0.34	0.56	0.51	0.28	–	–
HD132475	-1.52	0.34	0.17	0.46	0.34	0.20	0.38	–
HD140283	-2.58	-0.27	-0.48	-0.20	–	–	-0.84	–
HD160617	-1.83	0.04	-0.03	0.19	0.42	<0.35	0.25	–
HD166913	-1.93	0.47	0.39	0.65	0.42	<0.63	0.73	0.69
HD175179	-0.72	<1.28	<0.95	0.17	0.12	0.09	0.35	0.66
HD188510	-1.58	-0.04	-0.16	0.18	0.32	0.19	0.02	1.51
HD189558	-1.18	-0.70	0.15	0.44	0.30	0.16	0.48	1.54
HD195633	-0.71	<1.11	<0.66	-0.14	-0.13	-0.03	0.15	0.39
HD205650	-1.19	-0.02	0.05	0.19	0.22	0.14	0.12	–
HD213657	-2.01	0.04	-0.05	0.37	0.22	<0.53	0.05	–
HD298986	-1.48	-0.03	-0.09	0.23	0.32	0.43	0.07	–
G 01-039	-2.27	0.16	-0.07	0.29	–	–	-0.28	–
G 05-040	-0.93	<1.29	<1.09	0.37	0.16	0.17	0.33	1.46
G 20-024	-1.90	0.22	0.17	0.56	0.77	–	0.36	–
G 64-012	-3.10	-0.05	0.02	–	–	–	–	–
G 64-037	-3.16	-0.06	0.03	0.52	–	–	–	–
G 88-032	-2.53	–	-0.14	0.25	–	–	-0.33	–
G 88-040	-0.89	0.04	-0.27	0.02	0.12	0.03	0.04	–
G183-011	-2.12	–	-0.24	0.18	–	–	-0.33	–

Table 5.2: Errors on the abundances of Fe, Sr, Y, Zr, Pd, Ag, Ba and Eu for dwarfs. A '-' indicates that the error is missing due lacking measurements or upper limits.

Star	error(Sr)	error(Y)	error(Zr)	error(Pd)	error(Ag)	error(Ba)	error(Eu)
BD+092190	–	0.17	0.14	0.27	–	0.14	–
BD-133442	0.14	0.13	0.18	–	–	0.31	–
CD-3018140	0.11	0.12	0.14	–	–	0.14	–
CD-333337	0.11	0.13	0.17	0.27	0.25	0.15	0.22
CD-453283	0.30	0.15	0.17	0.19	0.25	0.15	0.22
CD-571633	0.10	0.12	0.17	0.23	0.26	0.15	0.22
HD3567	0.20	0.19	0.17	0.20	0.25	0.15	0.22
HD19445	0.11	0.12	0.15	0.27	–	0.14	0.17
HD22879	0.14	0.12	0.17	0.21	0.26	0.15	0.28
HD25704	0.11	0.12	0.17	0.21	0.26	0.15	0.22
HD63077	0.25	0.13	0.17	0.22	0.26	0.15	0.28
HD63598	0.14	0.12	0.22	0.19	0.26	0.15	–
HD76932	–	0.13	0.17	0.20	0.25	0.15	0.22
HD103723	0.13	0.15	0.17	0.19	0.25	0.15	0.22
HD105004	0.10	0.12	0.17	0.19	0.27	0.15	0.22
HD106038	0.17	0.14	0.17	0.21	0.25	0.15	0.22
HD113679	–	0.12	0.17	0.19	0.25	0.15	0.22
HD111980	0.22	0.13	0.17	0.21	0.25	0.15	0.22
HD116064	–	0.13	0.14	0.21	–	0.15	–
HD120559	0.12	0.15	0.17	0.21	0.25	0.15	0.22
HD121004	0.12	0.12	0.17	0.19	0.25	0.15	0.22
HD122196	0.14	0.12	0.16	0.27	–	0.14	0.17
HD126681	0.19	0.12	0.17	0.21	0.25	0.15	0.22
HD132475	0.11	0.15	0.17	0.19	0.26	0.15	0.22
HD140283	0.10	0.12	0.14	–	–	0.14	–
HD160617	0.14	0.12	0.21	0.21	–	0.15	–
HD166913	0.15	0.14	0.18	0.23	–	0.14	0.24
HD175179	–	–	0.17	0.20	0.26	0.15	0.30
HD188510	0.14	0.13	0.17	0.19	0.26	0.15	0.22
HD189558	0.14	0.13	0.17	0.21	0.25	0.15	0.22
HD195633	–	–	0.17	0.20	0.28	0.15	0.27
HD205650	0.25	0.13	0.17	0.21	0.25	0.15	0.22
HD213657	0.11	0.12	0.15	0.27	–	0.14	–
HD298986	0.17	0.14	0.17	0.19	0.28	0.15	0.22
G 13-009	0.10	0.12	0.14	–	–	0.14	–
G 05-040	–	–	0.17	0.21	0.26	0.15	0.22
G 20-024	0.11	0.12	0.15	0.27	–	0.14	–
G 64-012	0.10	0.13	–	–	–	–	–
G 64-037	0.10	0.13	0.14	–	–	–	–
G 88-032	–	0.13	0.14	–	–	0.14	–
G 88-040	0.10	0.15	0.17	0.19	0.26	0.15	0.22
G183-011	–	0.12	0.17	–	–	0.19	–

Table 5.3: Stellar abundances of Fe, Sr, Y, Zr, Pd, Ag, Ba and Eu for giants. The $'<'$ indicates that the abundance is an upper limit.

Star	[Fe/H]	[Sr/Fe]	[Y/Fe]	[Zr/Fe]	[Pd/Fe]	[Ag/Fe]	[Ba/Fe]	[Eu/Fe]
BD-01 2916	-1.99	0.11	0.03	0.26	0.39	0.16	0.60	2.33
BD+8 2856	-2.09	-0.01	0.04	0.05	0.12	<0.73	0.29	0.84
BD+30 2611	-1.20	-0.09	-0.35	0.28	-0.01	-0.50	-0.16	2.43
BD+42 621	-2.48	-0.18	-0.32	0.12	—	-0.40	-0.30	-0.24
BD+54 1323	-1.64	0.05	-0.08	0.01	-0.33	-0.21	0.40	0.04
CS22890-024	-2.77	-0.06	-0.25	1.09	—	—	-0.16	0.59
CS29512-073	-2.67	0.28	0.09	-0.07	—	—	–	0.20
CS30312-059	-3.06	0.09	-0.32	0.43	—	—	0.46	0.42
CS30312-100	-2.62	-0.34	-0.79	-0.17	—	—	–	0.12
CS31082-001	-2.81	0.66	1.03	0.77	1.29	1.19	1.37	1.53
HD74462	-1.48	0.06	0.38	0.54	0.13	-0.33	0.21	1.59
HD83212	-1.25	-0.04	0.21	0.27	-0.20	-0.53	0.32	0.79
HD88609	-2.87	0.04	-0.09	0.19	<0.07	<0.25	-0.79	-0.47
HD108317	-2.11	-0.05	-0.22	0.07	-0.08	0.15	0.62	0.29
HD110184	-2.40	-0.05	0.15	0.47	0.22	0.15	0.08	1.02
HD115444	-3.00	-0.08	-0.12	0.20	0.47	<0.35	0.37	0.97
HD122563	-2.81	0.04	-0.10	0.07	0.12	0.10	-0.70	-0.48
HD122956	-1.45	-0.04	0.00	-0.01	0.32	-0.28	0.54	2.53
HD126238	-1.92	-0.09	-0.27	0.06	0.24	-0.01	0.23	0.17
HD126587	-3.16	-0.01	-0.20	0.19	0.42	0.40	0.37	0.32
HD128279	-2.34	-0.36	-0.78	-0.35	-0.16	-0.24	-0.11	-0.56
HD165195	-2.10	-0.19	-0.01	0.09	-0.32	-0.60	0.01	0.53
HD166161	-1.25	0.29	0.29	0.26	0.00	0.05	0.45	0.07
HD175305	-1.38	0.01	0.12	0.29	0.04	0.04	0.26	1.81
HD186478	-2.42	0.08	0.01	0.31	0.26	0.23	0.36	0.47
HD204543	-1.84	-0.07	-0.14	0.07	0.04	0.04	0.20	0.17
HE 0315+0000	-2.59	0.13	0.08	0.30	—	—	0.17	0.63
HE 0442-1234	-2.32	-0.18	-0.24	-0.06	0.12	—	0.10	1.23
HE 1219-0312	-3.21	0.01	-0.19	0.19	—	—	0.74	0.76
CS 22881-039	-2.75	0.00	–	–	–	–	-0.62	–
CS 30317-056	-2.85	0.03	–	–	–	–	-0.32	–

Table 5.4: Errors on the abundances of Fe, Sr, Y, Zr, Pd, Ag, Ba and Eu for giants. A '-' indicates that the error is missing due lacking measurements or upper limits.

Star	error(Sr)	error(Y)	error(Zr)	error(Pd)	error(Ag)	error(Ba)	error(Eu)
BD-012916	0.18	0.20	0.16	0.20	0.22	0.34	0.25
BD+302611	0.26	0.18	0.22	0.21	0.28	0.14	0.16
BD+42621	0.15	0.19	0.17	–	0.32	0.14	0.16
BD+541323	0.12	0.18	0.16	0.20	–	0.17	0.18
BD+82856	0.12	0.15	0.14	0.21	–	0.14	0.19
CS22890-024	0.18	0.16	0.16	–	–	0.14	0.16
CS29512-073	0.14	0.15	0.16	–	–	–	0.19
CS30312-100	0.20	0.12	0.17	–	–	–	0.16
CS30312-059	0.15	0.13	0.37	–	–	0.14	0.19
CS31082-001	0.11	0.16	0.26	0.19	0.27	0.14	0.31
HD74462	0.10	0.16	0.26	0.18	0.25	0.14	0.19
HD83212	0.17	0.22	0.22	0.19	0.28	0.31	0.19
HD88609	0.11	0.23	0.14	–	–	0.14	0.16
HD108317	0.13	0.12	0.14	0.20	0.32	0.14	0.18
HD110184	0.22	0.14	0.18	0.23	0.22	0.14	0.19
HD115444	0.16	0.14	0.19	0.20	–	0.22	0.16
HD122563	0.13	0.16	0.18	0.20	0.25	0.14	0.21
HD122956	0.14	0.28	0.25	0.20	0.22	0.14	0.16
HD126238	0.14	0.12	0.14	0.19	0.28	0.14	0.17
HD126587	0.10	0.13	0.19	0.26	0.28	0.14	0.22
HD128279	0.11	0.13	0.14	0.20	0.22	0.14	0.22
HD165195	0.16	0.20	0.20	0.20	0.25	0.14	0.19
HD166161	0.14	0.18	0.17	0.19	0.25	0.14	0.19
HD175305	0.19	0.16	0.18	0.18	0.28	0.14	0.20
HD186478	0.11	0.12	0.14	0.18	0.25	0.14	0.17
HD204543	0.12	0.15	0.18	0.18	0.25	0.14	0.19
HE0315+0000	0.12	0.15	0.16	–	–	0.14	0.16
HE0442-1234	0.17	0.16	0.19	–	–	0.15	0.30
HE1219-0312	0.13	0.21	0.14	–	–	0.14	0.25
CS 22881-039	0.25	–	–	–	–	0.20	–
CS 30317-056	0.20	–	–	–	–	0.15	–

Chapter 6

The r-process site

The previous chapter discussed the origin of the heavy neutron-capture elements. At solar metallicity, Sr and Y (to some extent Zr) were found to be weak s-process elements, Pd, Ag and partly Zr are weak r-process produced, and barium and europium are main s- and r-process elements, respectively. At low metallicities, on the other hand, all elements are produced by the r-process, but where does this process take place, and is it likely to be in one kind of object only? This chapter focuses on revealing characteristics of the formation site, and several abundance comparisons and constrains are described to get the best trace possible. The model predicted yields are calculated for each stable isotope in the Periodical Table and summed to give elemental yields. In order to discuss the formation site the derived abundances are compared to two different model yield predictions, namely those from a high entropy wind from Kratz et al. (2007); Farouqi et al. (2009, 2010) following immediately after a supernova explosion, and those from a low mass supernova with a O-Ne-Mg core (Wanajo et al. 2003, 2009, 2010).

6.1 Comparison to supernova wind model predictions

First I will introduce the high entropy wind yields, which were calculated by Kratz et al. (2007) and Farouqi et al. (2009) and have kindly been provided to me by K.-L. Kratz and O. Hallmann (priv. comm). The high entropy wind (HEW) is connected to the adiabatically expanding winds from SN type II. These winds occur just after the proto-neutron star has formed, and they allow late neutrinos to interact with the outer layers of this object (see also Section 1.3). This creates relatively high entropies and intermediate neutron densities in the expanding ejecta (Farouqi et al. (2009) and Farouqi et al. (2010)). Most of the matter will be locked up in α-particles, but for an electron fraction, $Y_e = 0.45$ a sufficient amount of seeds and neutrons will be available to allow a rapid neutron-capture process to take place for entropies S = 110 k_B/baryon. These values will change with Y_e. The calculations of the reaction rates were preformed by using NON-SMOKER (Rauscher & Thielemann 2000) and the network code input includes the most up-to-date experimental data such as mass and β-decay rates. The free parameters of the network are $Y_e = Z/A$ (proton

number/atomic mass), the entropy (S) and the expansion velocity (V_{expan}). All three parameters relate to the the neutron-to-seed ratio (Y_n/Y_{seed}) in the following way:

$$\frac{Y_n}{Y_{seed}} = 10^{-11} V_{expan} \left(\frac{S}{Y_e}\right)^3, \qquad \text{where} \qquad \mathrm{S} \sim \frac{\mathrm{T}^3}{\rho} \tag{6.1}$$

where T is the temperature and ρ is the volume density. This formula is only valid for 0.4 $< Y_e <$ 0.495, 1500 $< V_{expan} <$ 30000 and 1 $< S <$350 k_B/baryon.

A large parameter space has been investigated by Farouqi et al. (2009); Kratz et al. (2007), but a typical expansion velocity of 7500 km/s was fixed to compute the yield predictions I use in the present comparison. Several electron fractions were tested as well as various entropies. Generally, the entropy is the free parameter and the neutron number density fixed inside the r-process interval of $10^{20} < n_n < 10^{28}$. The entropies in different ranges represent different processes (for fixed electron fractions). The main r-process, creating Eu, takes place in conditions with n_n values in the high part of the range (and large entropies, see below), while the 'weak' r-process is facilitated by lower n_n conditions (low end of before mentioned range) and lower entropies. Europium can not be created in low density environments (see items below). Four different ranges were mentioned in Farouqi et al. (2009):

- $1 < S < 50$. α-rich freeze out processes producing most stable isotopes between Fe and Sr
- $50 < S < 110$. A few free neutrons are produced, allowing a kind of s-processes
- $110 < S < 150$ and $1 \leq \mathrm{Y_n/Y_{seed}} \leq 10$. A weak r-process can start and Ag isotopes can be created
- $150 < S < 300$ (287). A neutron-rich environment suitable for a main r-process, creating all the heaviest isotopes

An upper entropy limit of 287 k_B/baryon was set when they (Kratz et al. 2007; Farouqi et al. 2009) calculated these yields, in order to avoid fission cycling[1]. It produces a very solid abundance pattern for the heavy isotopes, A $>$ 130, but the solar scaled pattern is not satisfactorily fitted for the lighter elements such as Ru - Ag in ultra metal-poor stars (Qian 2002), hence this cycling is avoided here. The predicted abundance yields I refer to here are mole fractions (Y_j), which are a function of nucleon fractions (X_j) and number densities (N_j) of a certain species j (isotope). They can based on Arnett (1996) be related/expressed in the following way:

$$Y_j = \frac{N_j}{\rho N_A} = \frac{X_j}{A_j} \tag{6.2}$$

where $N_A = 6.02 \cdot 10^{23}$ particles/mole (Avogadro's number), ρ is the volume density and A_j is the atomic mass number. From a ratio of two different species (e.g. j and k), which

[1]Nuclear fission (splitting) of isotopes, creating new lighter isotopes, which then because of liberated energy and/or neutrons can create heavier isotopes. This can continue in a 'cycle'.

creates a relative abundance (Y_j/Y_k), it can be seen that the only difference compared to the standard number density abundances I derive (as described in Chapter 5) is an additional ratio of the two different mass numbers of the species (which is of minor importance to this abundance comparison).

I will now compare the stellar abundances I derived to these model predictions, to see if a large sample of stars with abundances derived for elements between Sr to Eu can confirm or invalidate their findings (Farouqi et al. 2009) concerning entropy ranges and processes. Furthermore, I will investigate which stars fit these model predictions best.

In the following, all abundances (both observationally derived and predicted) will be given relative to Sr. Sr was chosen over Eu, since at the lowest entropies models do not predict any Eu but always Sr, and selecting Sr allows me to normalize all these predicted trends.

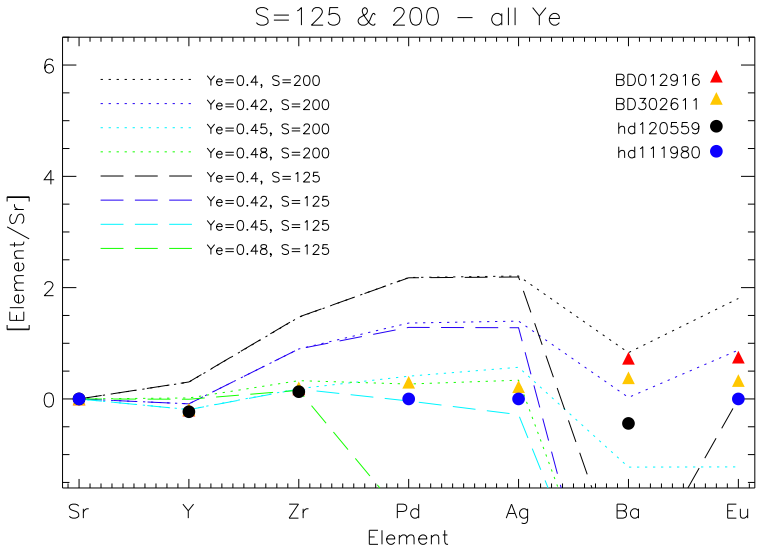

Figure 6.1: Observationally derived abundances of four stars (two giants and two dwarfs) compared to the model predicted abundances from Kratz et al. (2007); Farouqi et al. (2009). Every line represents different entropies (S) and electron fractions (Y_e). The Y_e value that match both low and high entropy best is 0.45.

First I want to constrain the value of Y_e, since many parameters have been varied. This is done by comparing four different electron fractions (0.4,0.42,0.45 and 0.48) at two different entropies to the stars. For clarity, only two giants and two dwarfs were chosen, for which several abundances were obtained.

Figure 6.1 illustrates how the electron fraction was fixed. The electron fraction of 0.45 provide the best agreement to these four stars for both the high and low entropy (as well as the majority of our stars). The $Y_e = 0.48$ also provides a satisfactory fit, but only for the highest entropy (S=200), since Y=0.48 with the lower (intermediate) entropy

that should be sufficient to create Pd and Ag, cannot reproduce the required amounts of these elements needed in order for the model predictions to agree with the observations. The model predictions of the two lower entropies severely overestimate the amount of Zr, Ag and Pd (and to some extent also Eu) and they were therefore not considered in the following comparison. Therefore $Y_e = 0.45$ was chosen since this value agree with the most of the derived abundances (at least in the range; Sr - Ag) regardless of entropy.

The parameters V_{expan} and Y_e are now constrained, but the entropies are varied in the model predictions, which the derived abundances are compared to. In order to constrain the number of entropies plotted in the figures that follow, Figure 6.2 show all the entropies compared to HD106038 and I will following select the most important entropies, needed to describe the production of both the heavy and light elements.

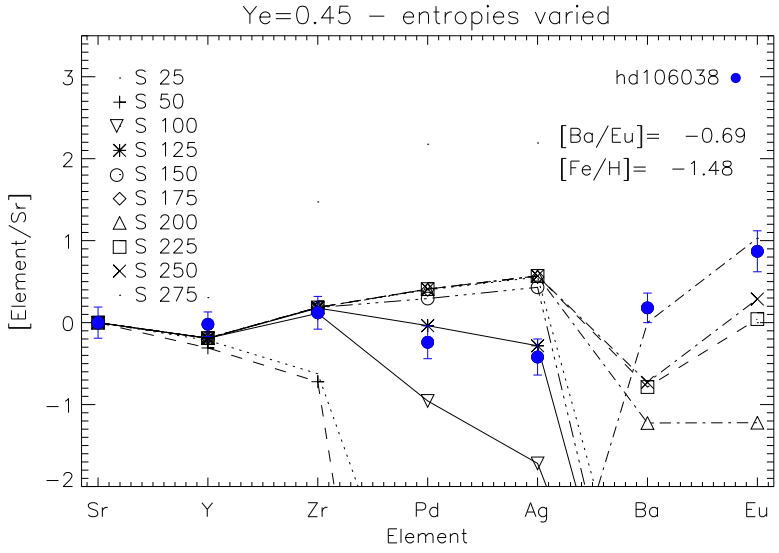

Figure 6.2: All entropies S listed in the units of $k_B/baryon$ compared to HD106038.

The lowest entropies such as 25 - 50 fail to correctly reproduce the observationally derived abundances of elements heavier than yttrium and they were therefore discarded from further comparisons. The entropy, S = 100 consistently under estimate the Pd and Ag abundances, and was therefore also removed from further comparisons. The most descriptive entropies, which are needed to explain the formation of both the heavy elements (such as Eu) and the lighter as well as intermediate elements (Zr - Ag) are S = 125, 175, 225 and 275 $k_B/baryon$.

Stars with different stellar parameters and chemical enrichments are compared to below, and the stars were selected so that they cover cases that indicate only one, two or a mixture of processes. The number of processes and possible mixtures of these were estimated on the basis of different entropies required. As mentioned above the entropy range from 110 to 150 k_B/baryon could be an indicator of a weak r-process, while the range from 150 to 287 k_B/baryon could be a tracer of the main r-process.

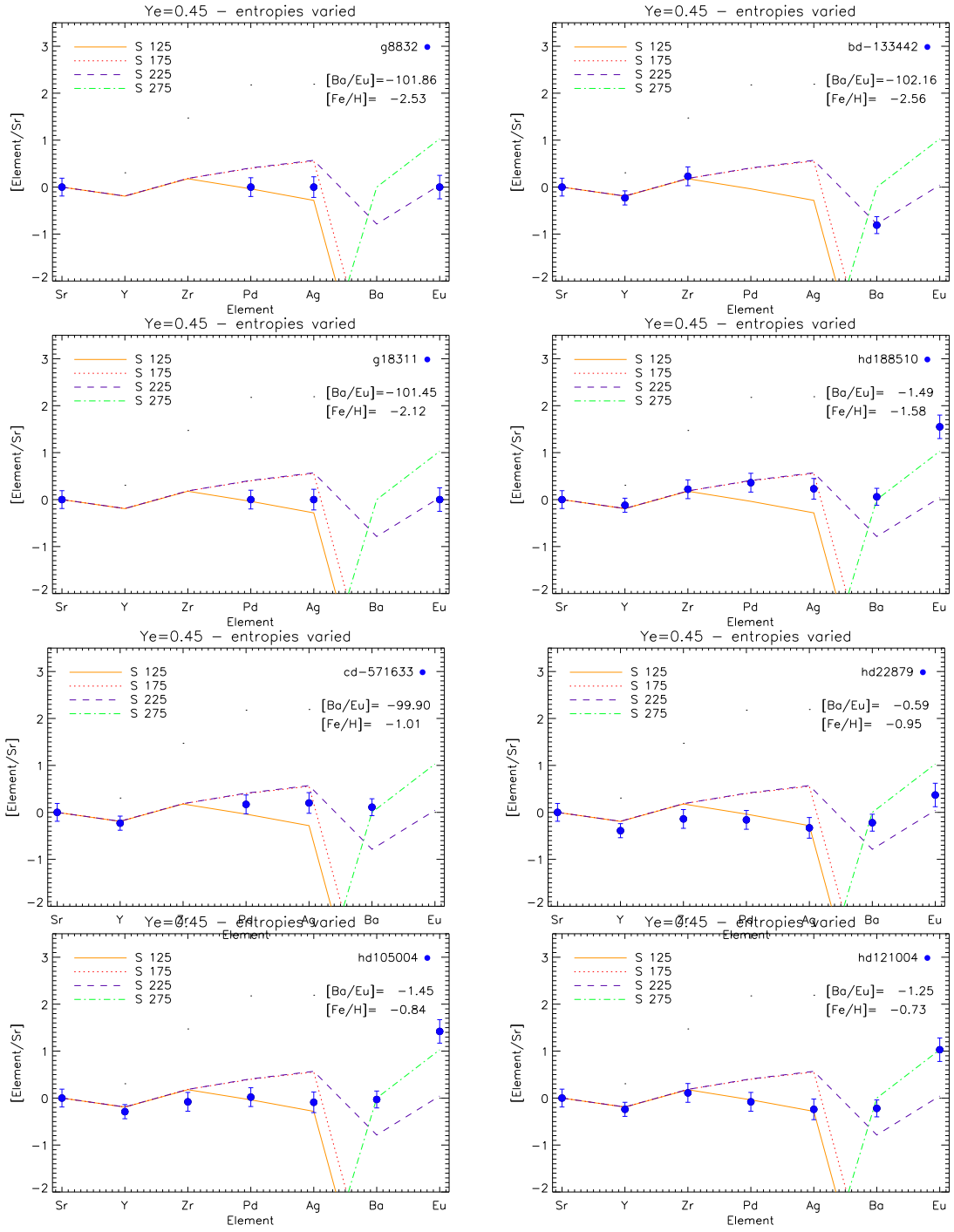

Figure 6.3: HEW model yield predictions for a $Y_e = 0.45, V_{expan} = 7500$ km/s and various entropies (S) compared to eight different dwarf stars. The stellar name, [Ba/Eu], [Fe/H] abundance ratio and values for the entropies are given in the figures.

Whether the underlying formation process of the elements is a 'mixed' or a 'pure' process is judged by the [Ba/Eu] ratio. A pure r-process is found if the value of [Ba/Eu] is below -0.74, an upper pure r-process limit is -0.36, while a pure s-process is obtained for [Ba/Eu] above 1.14 (all values empirically determined, K.-L. Kratz priv. comm.). Figure 6.3 shows a comparison of the HEW yield prediction to the dwarf stars mentioned in the caption. The stars are plotted in order of increasing metallicity (see Figure 6.3). The [Ba/Eu] ratio is sensitive to the relative contributions of main s- and r-process elements, since Ba is a main s-process and Eu is a main r-process. When the Ba/Eu-ratio is low, the r-process is dominant. When either Ba or Eu measurements are missing, the [Ba/Eu] value listed in the figures assumes large negative values. In a few cases the values between the upper r-process limit and the pure s-process value can be found. This could for instance be found in stars enhanced in lighter r-process elements (e.g. the stars from Honda et al. (2006)). Therefore, the entire abundance pattern as well as the metallicity need to be taken into consideration before characterizing the purity and number of processes which took place and enriched the star I compare the yield predictions to.

Figure 6.3 shows that HD188510, HD106038 and HD121004 are purely r-process enriched, and that the intermediate entropies (S = 125 - 150 k_B/baryon) fit the light neutron-capture elements such as Pd and Ag, whereas much larger entropies ($\sim$ 275 k_B/baryon) are required to fit the Ba and Eu abundances of these stars. The very different entropies could indicate that two different processes are needed; one 'weak' r-process with intermediate entropies and relatively low neutron abundances; and second a 'main' r-process with higher entropies and neutron densities. This is in agreement with the findings of Kratz et al. (2007) and Farouqi et al. (2009). However, I seem to find an entropy interval slightly smaller ($200 < S < 275$) than they found for the main r-process. The star HD22879, has a low [Ba/Eu] abundance of -0.59 dex, and can be considered (almost) pure. This star also shows the need for two very different entropies, 125 and 275 $k_B/baryon$, and it might therefore require two different processes to explain this. However, the metallicity of this star is [Fe/H] = -0.95, which is much higher than the metallicity where the s-process sets in and becomes dominating ([Fe/H]$\sim$ -2.5). It is an interesting outcome that this star shows indications of pure r-process products and no (or very little) s-process contamination with such a high [Fe/H]. This could mean that the [Ba/Eu] needs even stronger constraints. Another option is that there exists more metal-rich, [Fe/H]$<$ -1, stars, that mainly show r-process yields, which could indicate that the ISM is either not as well mixed at these metallicities as it is thought to be, or that these stars received the majority of their gas from a supernova, that triggered star formation of gas which was mainly from it's own explosion yields.

Now comparing the giants to the HEW yields, higher [Ba/Eu] ratios are found. Figure 6.4 shows that these values range from 0.05 to -0.6 dex. The lowest value derived for HD115444 indicates an almost pure r-process enrichment, and when taking the metallicities of these five giants ([Fe/H] $\sim$ -3.16 to -2.81) into consideration, the remaining stars in Figure 6.4 are likely to be pure r-process tracers as well. HD122563 also seen in Figure 6.4 is the so-called Honda star (Honda et al. 2006), and is one of the stars defining the upper limit for the pure r-process. All the above giants show the need for two very different entropies,

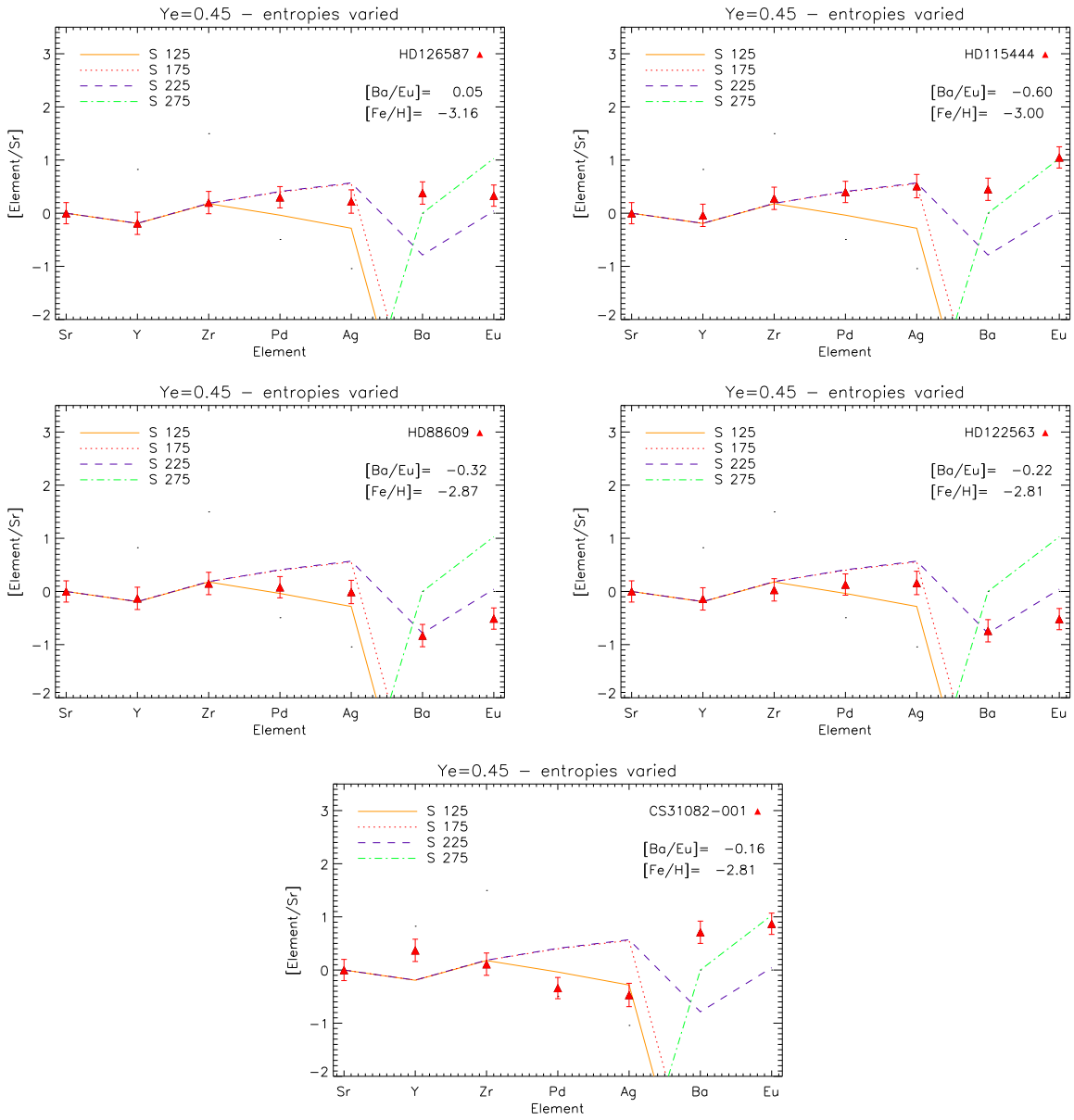

Figure 6.4: HEW predictions compared to abundances of five giant stars (HD126587(might be pure due to the low metallicity), HD115444(pure), HD88609(upper limit of pure), HD122563(upper limit of pure), CS31082-001(upper limit of pure/mixed)). Predictions with varying entropies are shown for the elements between Sr and Eu. The [Ba/Eu] ratio and the star, for which I have plotted the abundances, are given in the figure legend.

in order to explain the production of both lighter elements (Pd - Ag) as well as heavier elements (Ba - Eu). As for the dwarfs, the purity of the r-process and low metallicity ensure that the neutron-capture processes enriching the giants are indeed r-processes.
Based on the comparison from Figures 6.3 and 6.4 which show a need for very different

entropies in order to explain the abundances of both Sr and Eu two different processes seem necessary, however, this is strongly dependent on the models which are compared to, and they face some problems, such as incomplete reaction rates in their networks or that they are modelled in 1D or 2D, not 3D. Hence, there might also be another solution to obtain e.g. different entropies other than having two different processes (see 'A short discussion' just above the Summary for further considerations).

Figure 6.5 shows different trends compared to Figure 6.4. Two stars (HD186478 and

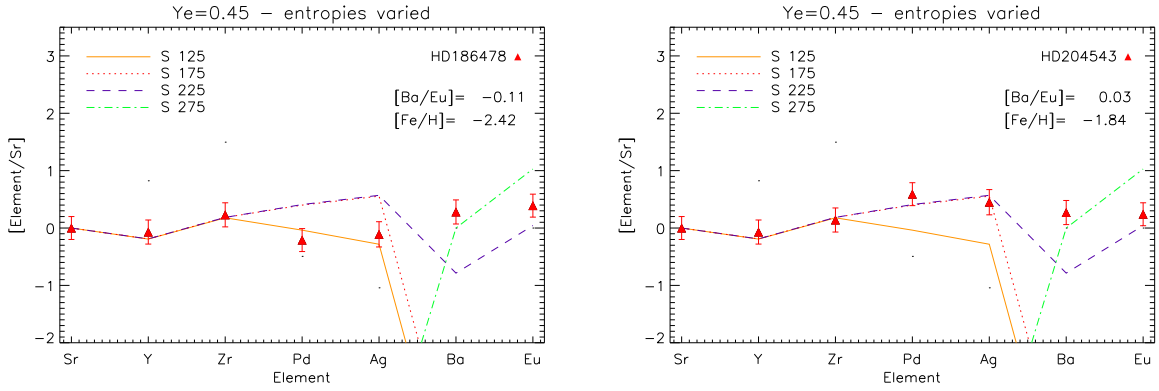

Figure 6.5: Model predictions compared to two stars, HD186478 and HD204543, which show the need for a mixture of processes - not a pure r-process, and a need for one process with a very large entropy.

HD204543) with low to intermediate metallicity ([Fe/H] = -2.42 and -1.84, respectively) show that the first mentioned star's chemical composition is not a pure r-process, but could very well be a mixture of s- and r-processes at this metallicity, whereas the second mentioned star only needs one entropy (i.e. one process) to explain all the abundances. This entropy is high (S $\sim 250 k_B$/baryon) and fits all abundances except Ba, which at this metallicity could have experienced s-process contribution before being incorporated in this star.

The majority of the stars (both dwarfs and giants) show good agreement (within the error) to the HEW yield predictions. More than 70 % indicate the need for very different entropies (S = 125 versus 275) to explain the production of Sr, Y, Zr, Pd, Ag, Ba and Eu. The HEW model predictions show an overall good fit to very metal-poor stars as well as very r-process enhanced stars (such as CS 31082-001). The very r-process enhanced stars always display some scatter, both star-to-star scatter as well as an abnormal stellar abundance pattern, so some deviations from a perfectly well predicted abundance pattern must be expected.

⋆ Conclusions: For the majority of the stars shown in Figures 6.3 - 6.4, two very different entropies are needed in order to explain the abundance ratios derived from observations. Some of these stars have pure r-process abundance patterns (34%), and following the course

of Kratz et al. (2007); Farouqi et al. (2009) this could be an indication of a need for two different r-processes, a main and a weak.

However, the presence of two different r-processes cannot be proven from the abundance comparison found in this chapter's figures. There are possible scenarios that could offer very different entropies within the same object, unfortunately these have not been fully explored yet. The scenarios could be supernovae with delayed detonation or shock fluctuations (Roberts et al. 2008). Therefore, by being limited to the current existing models, two different entropies (S = 125 and 275) are evidently needed to produce an agreement with my derived abundances of Pd, Ag and Ba, Eu which so far points towards two differing processes.

6.2 Comparing to low mass SN yield predictions

The yield predictions for the electron capture supernovae with the O-Ne-Mg cores have been kindly provided by S. Wanajo (priv. comm.), and are based on self consistent 2D models. A careful treatment of the neutrino interactions was included in the models. The yields are calculated using post processing networks, in which the output parameters from the supernova explosion, such as temperature, density, pressure, entropy and Y_e are applied as input parameters, hence there are no free parameters in these calculations. Typical input values are: temperature; T = 9×10^9 K, entropy; S $\sim 15 k_B$/baryon (much lower than in the HEW predictions) and $Y_e \sim 0.4$. The scenario allows neutron-captures to take place in the neutron-rich clumps of matter, which will convectively be transported to the outer layers.

The different Y_e models shown here have been obtained by the following calculations of the mole fractions[2] (for definition see equation 6.2) :

$$Y_Z(Y_e) = \frac{Y_Z(Y_{e,org})M + \Sigma_i Y_Z(i)\Delta M_i}{M + \Sigma_i \Delta M_i} \tag{6.3}$$

where ΔM_i is the relative mass of the elements to be ejected at an Y_e lower than $Y_{e,org}$, and this mass is set to $2 \cdot 10^{-5} M_\odot$. M is the total mass of the ejecta calculated for the higher (original) $Y_{e,org} = 0.4$, and this mass is $1.136 \cdot 10^{-2} M_\odot$ (S. Wanajo priv. comm.). Y_Z is the predicted yield (mole fraction) of the element with atomic number Z . These values are based on Wanajo et al. (2010) and S. Wanajo (priv. comm.). They have been calculated as a function of the decreasing Y_e, and by adding up the yields linearly (equation 6.3) for each element the proper abundances/yields are obtained. This lead to the model predictions compared to the abundances in the Figures 6.6 to 6.11. Yields calculated with lower Y_e were necessary in order to obtain considerable amounts of Pd. Elements heavier than Pd were not predicted in the previously calculated 1D yields from Wanajo et al. (2009), where electron fractions of 0.462 and 0.475 were applied. Wanajo et al. (2010) studied the effects that 2D simulations and low Y_e have on the yields. With electron fractions down to 0.15 they found that the Ba and Eu abundances in HD122563 could be correctly

[2] I will use yield predictions instead of saying calculated mole fractions.

reproduced. I have adopted these 2D model predictions and summed them, as described

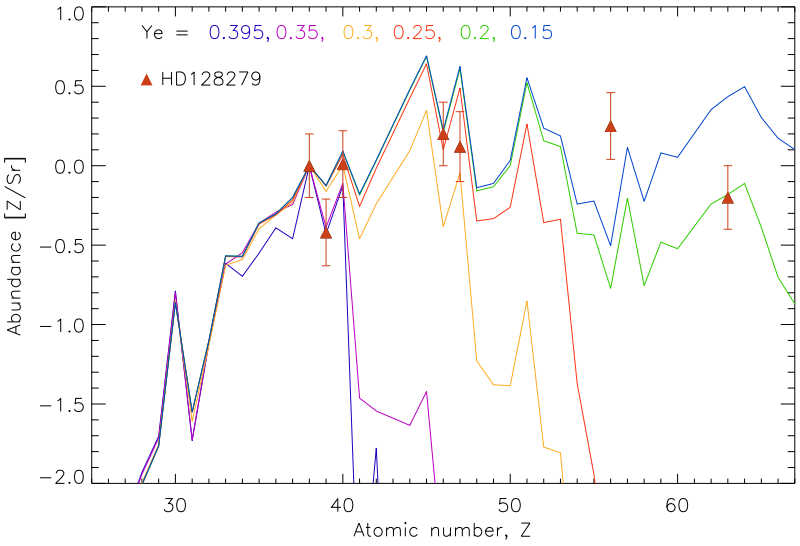

Figure 6.6: HD128279 (giant) is compared to different yields calculated as a function of Y_e. The highest electron fractions (0.395 and 0.35) are seen to have too few free neutrons to create the heavier elements (Ag - Eu).

above (equation 6.3), in order to compare them to my stellar sample, and determine if these model predictions fit the stars better than the yield predictions from Kratz et al. (2007) in previous section. Furthermore the comparison will reveal if the model predictions fit a certain type of stars better than others, e.g. enhanced versus chemically normal, metal-poor versus more metal-rich etc. In the following I binned the yields in steps of 0.05 in Y_e and have shown all the the yield predictions (Y_Z) with varying Y_e between 0.395 and 0.15. I will compare all the different $Y_Z(Y_e)$ to HD106038 in order to select the most relevant Y_e values for the remaining plots (in order to keep them as simple as possible). From Figure 6.6 yields calculated with Y_e= 0.395 and 0.35 only manage to correctly reproduce Sr - Zr, however there are too few neutrons available at these Y_e to create the heavier elements (Ag - Eu) and I have therefore only considered the lowest electron fractions in the following figures.

Stars, for which the majority of elemental abundances under study have been derived are selected, combined with those that provide best and worst agreements with the model predictions from Wanajo et al. (2010). These stars are shown in the Figures 6.7 and 6.11 and are listed below:
BD+54°1323, (BD+08°2856), HD122563 (see Figure 6.8), HD128279, HD186478, HD88609 (see Figure 6.9) and CS 31082-001 (see Figure 6.10),
CS 31082-001 was only added to allow a direct comparison of the model agreement this star shows to Kratz et al. (2007) and Wanajo et al. (2010). The dwarf stars shown are:

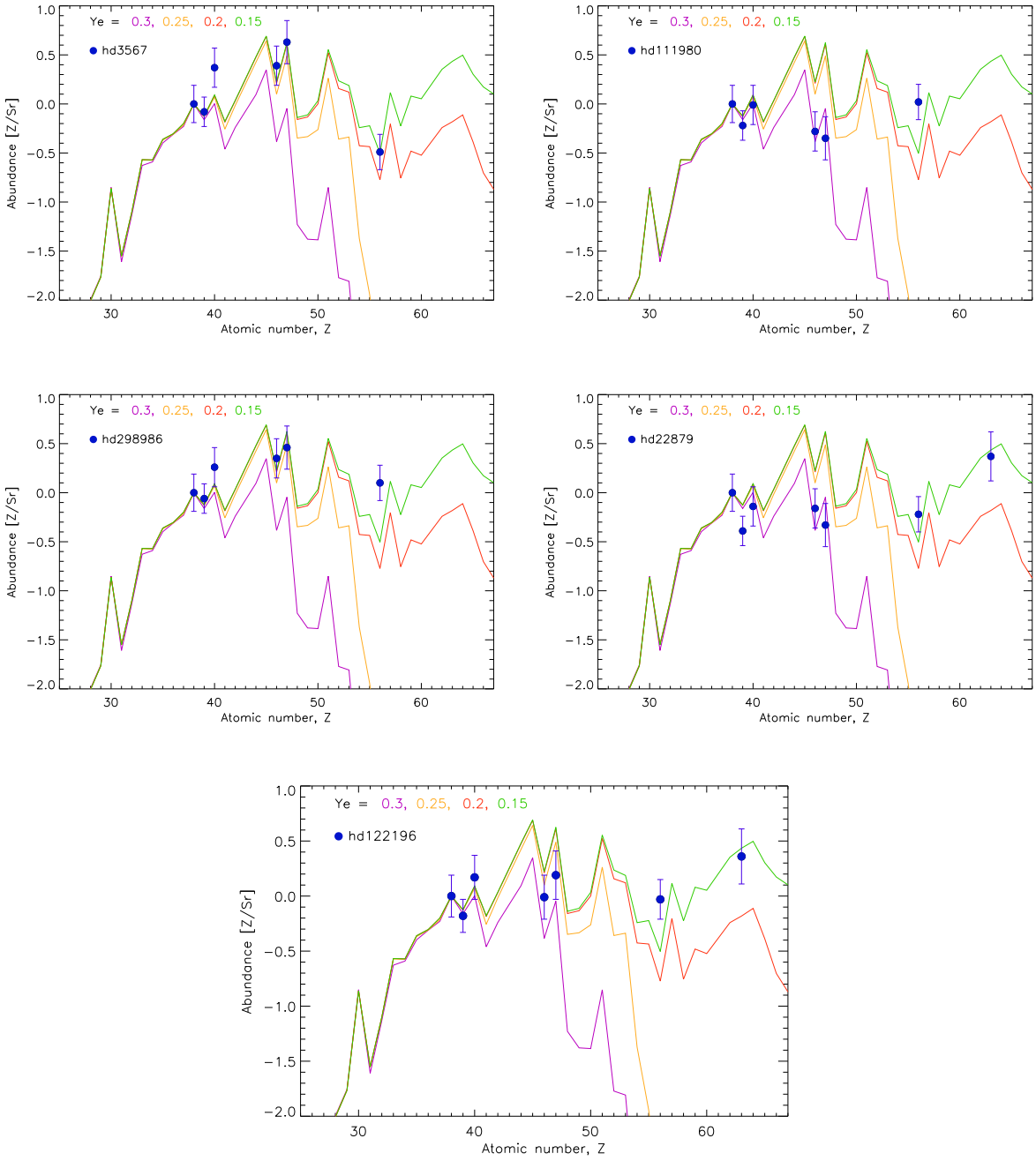

Figure 6.7: Low mass SN model yields with 0.05 step sized decreasing Y_e starting from $\sim$ 0.3 to 0.15 compared to dwarf stars with my derived abundances. The stars are indicated in the figures.

HD3567, HD111980, HD298986, (HD213657), HD122196, (HD105004)
and several other dwarfs providing satisfactory agreement (not shown) are:

HD76932, HD113679, G 88-40, HD63598, HD166913, G 13-9.

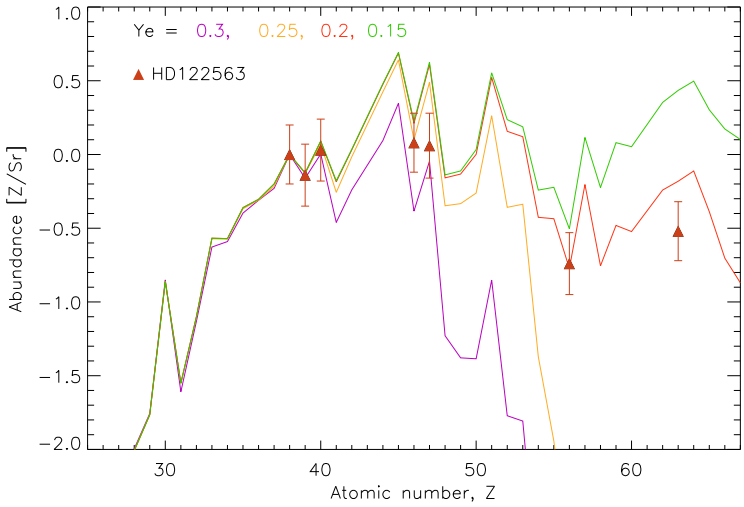

Figure 6.8: HD122563, the prototype star showing enrichments in the lighter of the heavy elements (i.e. from Sr - Ag). Here the model predictions offer a quite good fit to the derived abundances, and electron capture O-Ne-Mg SNe might very well be the formation site of stars with such abundance patterns.

From the dwarf stars (Figure 6.7) the elements are seen to be created at different values of Y_e, where the heavier elements (increasing Z) require a decrease in Y_e - i.e. they need more neutrons to be produced. For the Sr to Zr abundances several dwarf stars provide a good fit to the model predictions calculated with a Y_e in the range 0.35 to 0.395, Pd and Ag seem to start being produced in the proper amounts starting from values of 0.3 down to 0.2 (in Y_e). Most stars shown here have abundances of Ag and/or Pd which agree with the model predictions with $Y_e \sim 0.25$ (i.e. one of the derived abundances lie on the Y_e=0.25 line). The Ba abundances fit the predictions based on a $Y_e \sim 0.2$ well, and the Eu abundances require very low electron fractions (0.15 - 0.2) in order to fit the predictions.

Similar element–Y_e relations are found for the giants, though the Y_e fractions seem to be shifted slightly towards higher values (see Figure 6.11). Abundances of Sr to Zr fit the predictions well in the Y_e range: 0.3 to 0.395, some of the Pd abundances fit model predictions spanning from 0.15 to 0.275, but the majority of the Pd (and Ag) abundances match the predictions in the Y_e range or 0.2 (0.175) to 0.275 (0.25). Again the Ba production seems to set in around $Y_e \leq 0.2$, but many stars would require even lower Y_e to provide a reasonably good agreement, so $Y_e \sim 0.15$ is the preferred value to form Ba. Eu, on the other hand, seems to be produced in sufficient quantities at higher Y_e values than mentioned for the dwarfs and Ba. Eu starts begin correctly accounted for in the 0.225-0.175 Y_e-models, and the model abundance predictions of Eu are often

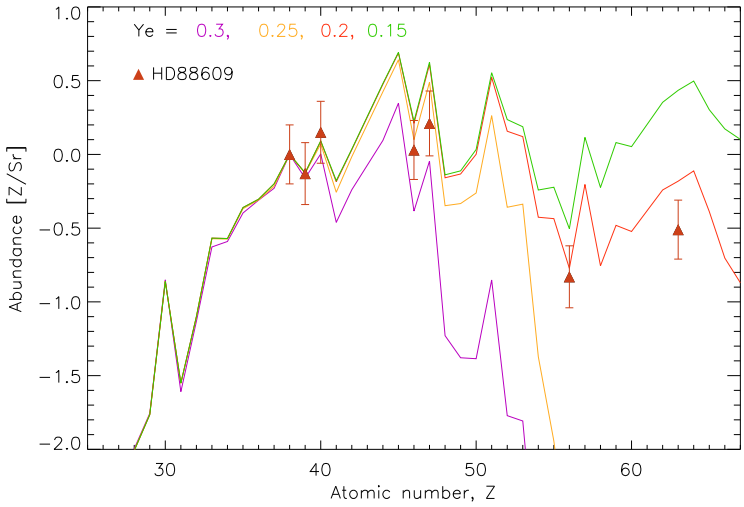

Figure 6.9: HD88609, is like HD122563 enriched in the elements Sr - Ag, and confirms the findings from HD122563, namely that O-Ne-Mg SN could be the formation site for stars with this kind of enrichment, based on the good agreement the model yield predictions provide to this kind of abundance pattern.

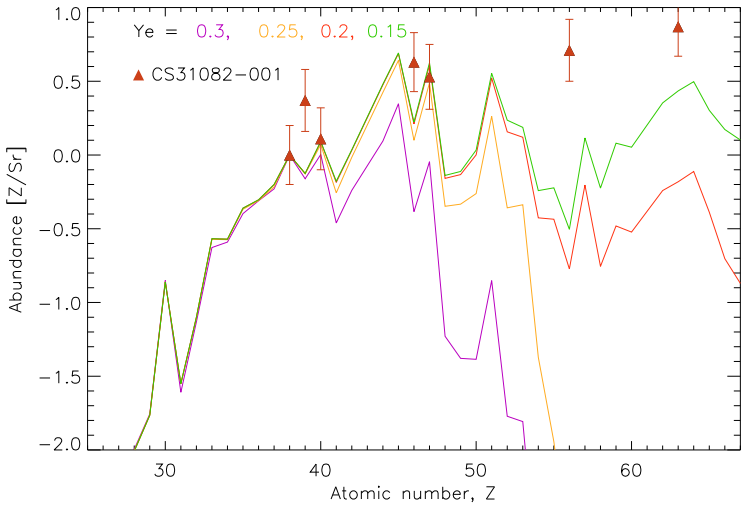

Figure 6.10: This star, CS 31082-001, is extremely enhanced in the heavy elements, and the model yield prediction do not explain this abundance pattern, indicating that a O-Ne-Mg Sn is unlikely to be the origin of these yields.

over-estimated at $Y_e \sim 0.15$. This change in electron fraction needed to produce Eu, could

be due to a different behaviour of Eu in dwarfs and giants, or that the giants need large NLTE abundance corrections. Since Eu is heavier than Ba, it seems unlikely that it would need fewer neutrons (larger Y_e) to form than Ba needs.

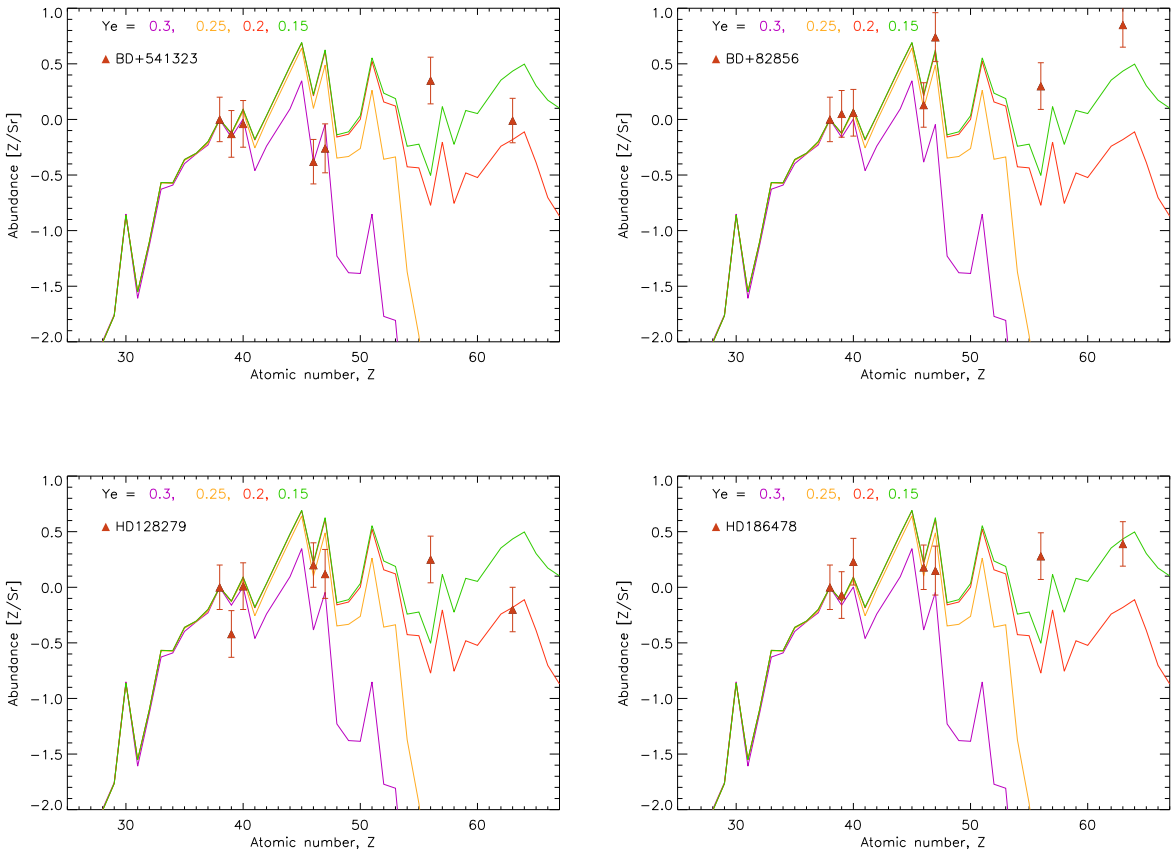

Figure 6.11: Yield predictions from Wanajo et al. (2010) for different Y_e indicated by different colours plotted versus atomic number in the figures. They are compared to four giants which are indicated in the figures. The abundances have been normalized to Sr. The [Sr/Sr] ratio is zero, not one, since the abundances are logarithmic. BD 54°1323, HD128279 and HD186478 all show a very low odd-even effect.

Generally, the model predictions from Wanajo et al. (2010) are seen to provide relatively good fits to 55-65 % of the stars in the various Y_e bins for the dwarf stars. The giant stars show good or satisfactory agreement in 45 - 62% of the cases (for various electron fraction).

The stars that provide the best fit to the model predictions from Wanajo et al. (2010) differ from the stars that fit model predictions from Kratz et al. (2007). Furthermore, the stars that fit the model predictions from Wanajo et al. (2010) best are seen to be enhanced in the lighter r-process elements (HD122563 and HD88609).

A short Discussion

The previous chapter (Chapter 5) showed the need for a fourth process (the second r-process) in order to explain the formation of Sr, Y, Zr, Pd, Ag, Ba and Eu based on the comparisons of observationally derived abundances. However, adding a comparison to the model calculated mole fractions/yields from (Wanajo et al. 2010) did not allow a strong site constraint, but offered a possible explanation. The current models are not capable of simultaneously explaining the seven element's observationally derived abundances. The outcome of this comparison is interesting; the yields from Wanajo et al. (2010) provide good agreement in $\sim$ 50-60% of the cases, especially for the stars enhanced in the lighter elements, which could indicate that low mass O-Ne-Mg core collapse SNe might be good weak r-process candidates, even though they might not be the only ones. It could also mean that O-Ne-Mg supernovae are possible dominant formation sites creating relatively large amount of Sr - Ag leading to the abundance pattern seen in HD122563, whereas the stars enhanced in the heavy elements got their gas from from another site (e.g. HEW), which dominates the production of elements like Eu. Model predictions from Kratz et al. (2007) and Farouqi et al. (2009) showed that two very different entropies were needed in $\sim$ 70% of the stars in order to explain the abundances I derived, and this could indicated that two different r-processes would be needed. The stars that show a pure r-process pattern provide even stronger indications of two r-processes. Their predictions match stars such as CS 31082-001, a star that is enhanced in especially the lighter but also the heavier elements, and satisfactory fits to the chemical normal stars are also provided by their calculations. Unfortunately, neither of these comparisons are sufficient to prove or fix the formation site, even though they offer promising suggestions. More stars might need to be investigated in order to see if the agreement with either of the models is statistically speaking strong enough to constrain the site. The models, however, would also need improvements and further investigations, since the present models fail to simultaneously reproduce all the elements (in the range: Sr - Eu), and modelling of a full SN explosion has still not succeeded. The lack of 3D models come in addition to this. The step from a 1D (Wanajo et al. 2009) to 2D (Wanajo et al. 2010) shows the importance and dependence the yields have on the dimensions modelled. In their 1D models they were not able to produce Pd, Ag and Cd, while with their 2D models they were capable of getting small amounts of these elements with low Y_e values. In order to improve the model calculations better input physics, such as reaction rates, is central to such achievements. However, with the current instruments these measurements are limited to the lighter isotopes, and the heavy isotopes rely on extrapolations of the rates measured for the lighter isotopes. Finally, there is one crucial point related to the yield calculations, which is the mixing of the gas that is fed back into the ISM from the SN event. To date we do not know how these gasses mix and in which ratios they are incorporated into the following stellar generations, and we therefore operate on speculations, where we have to search for the dominating source. This is why old metal-poor stars are so important to such studies, since we might be able to trace the imprint of only one or very few supernovae in these old stars.

6.3 Summary

I compared the derived stellar abundances to the different models, in order to gain an understanding of the formation sites of the second/weak r-process. This is where I can apply my results and try to extract more information from the stellar abundances. The advantage of this comparison is that I have a large homogeneous sample covering both dwarfs and giants, chemically normal and enhanced in neutron-capture elements, whereas the comparison from the theoreticians tend to be a mixture of samples, which can easily introduce offsets and biases in the conclusions they draw. This homogeneity of the sample allowed a very direct comparison, and ensured that the information extracted is a clean trace of the formation site. Now, summarising the results from the section above:

The model predictions from Kratz et al. (2007) are seen to provide very good agreements with stars enhanced in heavy elements (CS 31082-001), and good or satisfactory fits to chemically normal stars, whereas models from Wanajo et al. (2010) agree well with the stars enhanced in the lighter of the heavy elements such as Sr - Ag (e.g. HD122563 and HD88609). The low mass SN from Wanajo et al. (2010) are thought to arise from a super-AGB star, and these O-Ne-Mg SN could very well be the site for the 'weak' r-process. Since the progenitor of the super AGB star and the light SN is the same, it could explain the similarity of the Pd and Ag abundances to the Zr abundances found in Chapter 5, and make a connection between the second r-process and the (weak) s-process.

The supernovae seem to be good r-process sites, but different SN would be needed to explain the stellar abundance pattern (Sr - Eu) and the abundance star-to-star scatter. The picture that can be drawn based on these results is the following: The low mass O-Ne-Mg SNe could be production sites for the lighter of the heavy elements (Sr - Ag) but they cannot produce elements like Eu, whereas the heavier more energetic SN work as objects producing the heaviest elements (Ba, Eu and heavier) by offering higher energies, temperatures and more building seeds. For the latter, the high entropy winds offer a good solution and they can predict a full r-process pattern with varying entropy.

Yet, no final answers related to specifics on the formation site were found, even though Kratz et al. (2007); Farouqi et al. (2009); Wanajo et al. (2010) provide good agreements to certain sub-groups of stars, however, neither of the models investigated here are capable of matching the observationally derived abundance covering the full range between Sr and Eu (with only one set of parameters). Each of the models have some shortcomings, e.g. the post processing models from (Kratz et al. 2007; Farouqi et al. 2009) are not based on self consistent SN models, and the predictions from Wanajo et al. (2010) fail to produce any amount of the heavier elements such as Eu. However, based on the agreement I obtained for 50% - 70% of the stars, these models/sites could contribute at some level to the ISM and explain some (amount) of the abundances studied here. The final site constraint on the second r-process remains to be made.

Deriving stellar abundances of Pd and Ag in ultra metal-poor stars would be essential to see if the weak r-process is working at these metallicities. At such low metallicities a different type of supernova might be needed to explain the abundance pattern (e.g. more massive, experiencing large fall-back and only producing very small yields of the lighter

heavy elements). Very few supernovae would be traced at such low metallicities ([Fe/H]< -4) and the effect of the mixing would be less important. One ultra metal-poor star is HE 0557-4840 with a [Fe/H] = -4.75 dex. The star is far away and very faint, thus the S/N of the spectra is too low to detect Pd and Ag. A great deal of observing time would be needed to allow a derivation of heavy element's abundances in these faint ultra metal-poor stars.

Chapter 7

Discussion and Conclusion

I have carried out a study of 73 stars, mainly halo field stars, for which I have reduced the spectra, determined stellar parameters and derived the stellar abundances of Fe, Sr, Y, Zr, Pd, Ag, Ba and Eu. I compared their abundances and found trends which strongly indicate the existence of a second r-process. From agreements of derived abundances and model predicted yields I extracted characteristics of the formation processes and discussed the formation sites.

Discussion

The Introduction mentioned some of the arguments put forward in the literature of the various neutron-capture elements being produced by a second (weak) r-process. The main indicators were the large star-to-star scatter of the abundances as well as the relative overproduction of the lighter of the heavy elements (Sr - Sn), with respect to the Solar System scaled (SS) main r-process ratio. Since the r-process is a primary process, hence the only process working at very low metallicity, the relative excess of these lighter of the heavy elements must be explained by a second r-process. Unveiling the nature of this process, time of onset, and formation site will allow a better understanding of the chemical evolution of the Galaxy.

Lighter elements produced by the same process, such as α-elements, show very low star-to-star scatter at all metallicities. Similar low scatter are seen for the iron-peak elements, both complete and incomplete silicon burning elements (Cayrel et al. 2004) indicating that the Galaxy was already rather well mixed at low [Fe/H]. Therefore it is unlikely that the neutron-capture elements showing such large star-to-star scatters could be produced by one single process. The uncertainties on the abundances are comprised of observational errors, as well as model uncertainties and assumptions. Combining these uncertainties leads to abundances errors of the order of 0.2 -0.25 dex for elements like Pd, Ag and Ba (see Table 5.4).This demonstrates that these errors cannot account for the star-to-star scatter, which for elements such as Ba spans $\sim$ 2 dex. Hence, the scatter could be due to an inhomogeneous early Galaxy or to multiple processes being at work. The fact that the

alpha elements show such a low scatter could be explained by their yields being produced by one dominant source (SN II), while the neutron-capture processes could come from a variety of supernovae or other objects/sites.

The complexity of the neutron-capture processes, in particular of the r-process, is also evident when comparing stellar abundances of various stars to the Solar System scaled r-process ratio (as done in Figure 1.7). HD122563 is one of the stars enhanced in lighter heavy elements (Sr - Ag) and shows a direct need for an object capable of creating very different entropies and/or electron fractions, or a second site producing the additional amount of these elements. CS 31082-001 and CS 22892-052 on the other hand are generally enhanced in all heavy elements. The SS scaled r-process ratio is not perfect, yet this ratio is calculated based on solar abundances, from which the amount of s-process contribution per isotope is subtracted. Therefore the relative r-process ratio will carry a sum of the small uncertainties from the solar abundance and the errors on the s-process fractions (which can be quite large). Despite the uncertainties, the differences in abundance between the lighter and heavier of the heavy elements cannot be explained by simply improving the r-process ratios. A second r-process is required at lower metallicities.

The outcome of this abundance study confirms the need for two r-processes. The scatter seen in Figures 5.1 to 5.7, starts below [Fe/H] = -2.5 dex. Below this metallicity the chemical history of the heavy elements in our Galaxy is limited to r-process feed-back leaving behind a large scatter in the abundance. Due to the large scatter of the neutron-capture elements the interstellar medium cannot have been well mixed, however, as more supernovae occur, mixing of the interstellar medium increases. Therefore, at very low metallicities the abundance compositions we derive, will carry imprints of very few supernova explosions: the slow mixing of the interstellar medium works in our favour, allowing us to test more clean and pure r-process abundance patterns. Nevertheless varying abundance ratios of neutron-capture elements are obtained at low metallicity in stars that show very little variation in the alpha element abundances (Cayrel et al. 2004; Hansen et al. 2011b), and this carry great challenges for the supernova model predictions.

Based on the scatter and relatively flat abundance trends seen from Figures 5.1 to 5.7, it was not possible to elaborate on the onset of the second/weak r-process. Figure 5.6 shows the barium abundances as a function of metallicity, and the decreasing scatter at metallicities above -2.5 dex suggests that the main s-process begins to dominate and homogenizes the formation of Ba. These results are discussed here and listed in the Conclusion.

Silver and palladium show strong anti-correlations when compared to europium, therefore they cannot be products of the main r-process, as europium is. A weaker anti-correlation, but still statistically significant, is seen when comparing first Ag then Pd to Ba (as shown in Figure 5.12 and 5.17, respectively). Both Pd and Ag differ from the weak s-process elements Sr and Y, but show some resemblance to Zr. Figure 5.20 shows that Zr correlates with Sr and Y. Zirconium must be produced in part by a weak s-process and by a process similar to the second/weak r-process responsible for creating silver and palladium. Thus, Zr is a transition element; it indicates on the Periodic Table where the weak r-process begins. Silver and palladium are clearly seen to be produced by the same process, as shown by the nice correlation in Figures 5.11 and 5.19.

Figures 5.4, 5.5 and 5.11 show that there is considerable scatter ($\sim$ 1 dex) among the stellar Pd (Z=46) and Ag (Z=47) abundances, with Figures 5.4 and 5.5 showing the average abundances of Pd and Ag are 0.21 dex and 0.18 dex, respectively. The scatter is in the same range as described by Johnson & Bolte (2002), however their odd-even effect is much larger than the one derived here. The small odd-even effect ties the origin of these two elements closer together. The flat trend of [Pd/Fe] and [Ag/Fe] (Figure 5.4 and 5.5), together with the tight correlation of [Ag/H] and [Pd/H] (Figure 5.11 and 5.19), illustrate that the second r-process creates these two elements at all metallicities (down to [Fe/H] $\sim$ -3.2 dex). There is no break or slope change in the trends showing the onset of a different process, as is the case for other elements such as barium. Thus the second (weak) r-process is seen in extremely metal-poor stars (i.e. below -3 dex in [Fe/H]). According to Lai et al. (2008), the weak r-process should not be seen in the most (hyper) metal-poor stars, since they did not see such indication for [Ba/H]< -5 (corresponding to a value below -4 dex in [Fe/H]). However, this statement and these values were based on comparisons of Sr to Ba, and Sr might not be the best tracer for the weak r-process since there is a weak anti-correlation of Sr and Ag and Sr and Pd (see Figure 5.8 and 5.14).

Generally the abundance derived in Chapter 5 demonstrate, that there is a shift in the trends of giants and dwarfs. The trends are generally consistent, tend to overlap, but still show a slight shift of a few tenths of a dex. This shift could be due to as yet undetermined non local thermodynamic equilibrium (NLTE) effects of these heavy elements, but it could also be an indication of incorrect assumptions in the model treatment of the stellar atmospheres and/or synthesized abundances. The abundance difference could be a sign of mixing processes taking place in giants, where the heavy elements would sink to the center of the star, and lighter elements brought up to the surface. This would change the stellar surface composition and thereby be reflected in the abundances derived from the surface layers. A large expansion of the 3D models would be required to carefully evaluate this effect on the abundances of the heavy elements.

The site of the second r-process was investigated in Chapter 6 by comparing the derived stellar abundances to model yield predictions from high entropy supernova winds (HEW) (Kratz et al. 2007; Farouqi et al. 2009) and from low mass O-Ne-Mg core collapse supernovae (Wanajo et al. 2010). The two different model predictions turned out to agree with different types of stars. The low mass SN model fits the stars enhanced in elements from Sr to Ag very well, as well as the chemically normal stars. The wind model predictions best fit the normal stars as well as provide good agreements with stars enhanced in the heaviest elements (e.g. CS31082-001). This finding suggests the low mass supernovae are more likely to be the site of the second/weak r-process. To ensure the validity of my results, I consider the [Ba/Eu] ratio to make sure that my trends are purely due to r-processes and not a mixture of r- and s-processes. Still the metallicity should be taken into consideration when defining the purity and uniqueness of the r-process contribution. Both model predictions have their strengths and weaknesses. The low mass supernova predictions from Wanajo et al. (2010) have the advantage to be based on the so far most successful SN model explosion, and is furthermore in 2D. This means that the underlying physics should be weighted quite heavily. However, there are still some shortcomings in the SN model pre-

dictions, since 3D models cannot be fully carried out yet due to computational limitations. Improving the models from 1D to 2D yielded lower Y_e, which allowed the production of Pd, Ag and Cd in these low mass SN. The high entropy wind models on the other hand, have a more exploratory character, examining a large parameter space and basing their detailed chemical reaction network on laboratory experiments. This gives a lot of strength to the chemical reactions.

From the work presented in this thesis, as summarized above, the following conclusions can be drawn:

Conclusion

⋆ I have shown that Pd and Ag are similarly formed and have placed constraints on the formation site.

⋆ In the last two decades the understanding of the neutron-capture processes, and especially the r-process, has been developing very fast. Many studies (Burris et al. 2000; Cowan et al. 2001; Johnson & Bolte 2002; Sneden et al. 2003; Wanajo et al. 2003; Honda et al. 2006; Kratz et al. 2007; François et al. 2007; Lai et al. 2008; Sneden et al. 2009; Farouqi et al. 2009; Wanajo et al. 2010) suggest that there is a second r-process responsible for creating the light rapid neutron-capture elements. I have observationally confirmed this prediction.

⋆ Sr and Y (and Zr less so) are produced by: A weak s-process, with Zr as a possible transition element – bridging from (weak) s- to 'weak' r-process.
Pd and Ag (and to some extent Zr) are produced by: A weak r-process, a process, that possibly has more in common with the s-process than the main r-process, but nevertheless needs a high neutron density.
Ba is produced by: The main s-process.
Eu is produced by: The main r-process.

⋆ A promising site for the second/weak r-process are the O-Ne-Mg cores of low mass supernovae, which are seen to fit the abundance pattern of stars enhanced in the light r-process elements very well. The low mass SN cannot produce main r-process elements such as Eu. The HEW predictions are in general agreement with the vast majority of the stars, and seem to be a good explanation of the 'chemically normal' stars due to the considerable amounts of lighter r-process elements yield, as well as stars enriched in the heaviest of the heavy elements are well predicted by these models.
The main outcome from the comparison of the observationally derived abundances to the model predicted yields, was the evident need for a site capable of providing both medium and high entropies (S = 125 and 275) or very different Y_e values (0.3 - 0.15). However, with these current models, that face some shortcomings, it is yet not possible to place strong constraint on the site.

To fully constrain the site of the r-process to supernovae, the stellar abundances need to be compared to yield prediction from sources such as neutron star mergers as well. These yields still need calibration to carry out such model–abundance comparisons (G. McLaughlin priv. comm.). Conclusions on the r-process site could also be drawn if we understood the physics of supernovae better, i.e. is a low Y_e more likely than a high entropy. Observationally determined abundances of the lighter r-process elements seem to favour the low Y_e. This leads to other future aspects and ideas.

7.1 Future

This study was a step towards understanding the true and complex nature of the r-processes. A lot of work still has to be carried out to map this process in the best possible way, both regarding abundance studies of more elements as well as better model predictions of r-process yields. Detailed abundance studies are crucial for these model predictions, preferably not just elemental abundance studies, but well resolved isotopic abundances would provide help refining the model predictions. This is however very time consuming and requires very powerful instruments. Furthermore, large samples would be needed in order to have a statistically sufficient high number of stars to fully unveil the true nature of the neutron-capture processes.

In order to capture the onset of the weak r-process more ultra - hyper metal-poor stars are needed. These stars are often faint and far away and would therefore need to be observed for many hours, to obtain the proper spectrum quality needed to detect key elements such as Pd and Ag. A luminous subclass of metal-poor giants are the horizontal branch stars, which despite their very developed stage have shown to be good chemical tracers (Tautvaisiene 1997; Hansen et al. 2011b). Even with the VLT this would be very time consuming and more or less limited to the solar neighbourhood. However, the E-ELT could be helpful in this context due to its high-resolution spectrograph (CODEX), planned to search for extra-solar planets and nucleo-chronometry i.e. stellar dating via radioactive decay of e.g. U and Th. The advantage of the E-ELT would be that it would enable observations of stars much further away than the solar neighbourhood, which we so far have been constrained to observe with the current telescopes and instruments. It would be extremely interesting to carry out such an investigation, since it would allow a globalisation of the nature of the neutron-capture processes, and not just the 'localisation' that we are constrained to currently. This, however, lies far in the future, but there are several aspects that can be improved now and at lower costs (in spite of observational restrictions). Most of these improvements relate to our understanding of the physics, chemistry, and the assumptions we have to make in order to deal with the astrophysics in the models.

Our understanding of stellar evolution and the internal processes taking place during the star's life is far from complete. This means that processes such as the internal mixing, which might alter the chemical surface composition are poorly constrained. Some studies show indications of these mixing processes, such as atomic diffusion, and try to apply these

as a possible explanation of the differences in stellar abundance seen between dwarf and giant stars (Korn et al. 2006; Lind et al. 2008). Other studies disregard atomic diffusion as the reason for the abundance difference between dwarfs and giants in globular cluster (Gratton et al. 2001) because they do not detect these abundance offsets.

The lacking knowledge of the atomic structure and line transitions in heavy elements combined with the limited understanding of the stellar atmospheres prevent NLTE effects from being calculated. This in turn leads to less accurate stellar abundances of these heavy elements. To gain this information more laboratory measurement and even better lasers and spectrographs are needed.

From a slightly different theoretical point of view, better model yield predictions would be needed. Future 3D SN models could provide an answer to how low Y_e would be available or how high entropies could be achieved in an explosion. A self consistent exploding supernova model running from the core bounce to the very final explosion stage would be desirable, in order to see if supernovae could provide conditions suitable for creating both the lighter as well as the heavier neutron-capture elements. This would allow the r-process sites to coexist in a single object. Both weak and main r-processes could take place in supernovae if the protoneutron star would 'oscillate' and neutrino driven winds would lead to small shock waves travelling behind the original shock wave (Roberts et al. 2008). These waves would transfer energy to the surrounding media, heating the system and leading to increased entropies. This could provide conditions for a main r-process, but is so far a speculative scenario that needs testing. Furthermore, it would be very interesting to have model predictions with both a detailed understanding of the underlying physics of the object/site, as well as an improved understanding of the chemical reactions. So far reaction measurements have been carried out on isotopes up to atomic numbers around 100 (a few experiments have explored reaction of isotopes with A = 147 and 148), i.e. there is fair understanding on how these isotopes are created by neutron-captures, and how additional fission and delayed decays etc. affect these. However, beyond atomic masses of 100, the reaction rates and processes taking place and building up the very heavy elements are mainly extrapolations of less massive isotope's reactions. Exploring the reactions of heavy isotopes would require very high energies; it would be hard to control the environment such that the reaction would be allowed to take place and to measure the reaction cross-sections and rates. Very sensitive instruments and detectors would be required, and these must not be destroyed by the very energetic radioactive radiation.

Finally, there are studies to carry out with all the current instruments. A thorough revision of all stars having spectra available in the data archives of UVES, Hires and HDS could be carried out. We would not investigate other parts of the Galaxy, or have better atomic data at hand, but it would lead to the statically speaking largest possible sample. It would provide an overview of which stars would need to be re-observed in order to have spectra of high enough quality to detect all elements between Sr and Sn. Some studies have derived abundances of elements in this range, but never in such a large sample as I am referring to with spectra of high-resolution and high S/N ratios. Most of the spectra available are of satisfactory quality, but obtaining extra high S/N ratio spectra for stars like HE 0557-4840 at a metallicity of [Fe/H] = -4.75 dex could allow detections of the

elements with atomic numbers between 38 and 50. This would allow us to determine the onset or the universality of the r-process in the local solar neighbourhood. It would require a lot of telescope time, but it could, if several studies would focus on this, be obtainable within the next 3 to 5 years. Another way to investigate stars further away would be via a detailed kinematical study as carried out by Nordström et al. (2004), but this time including giants as well in the suggested stellar sample. Many metal-poor stars are thought to have very elliptical orbits, and could therefore pass though the solar neighbourhood carrying information on the r-process's behaviour in regions far away from the Sun.

Acknowledgements

First of all I would like to acknowledge IMPRS and ESO for offering this PhD and opportunity to me. My supervisor F. Primas deserves a special thanks for her help, criticism, thesis corrections, and encouragement to independent work, which has prepared me for future positions. I also wish to thank my IMPRS committee (B. Leibundgut, A. Weiss and M. Asplund) for supervision, help, useful comments and guidance during my PhD. During my stay at ESO I was given chances to travel and attend schools and conferences, which I am grateful for, since these provided a lot of contacts and fruitful science perspectives as well as ideas. The contacts I made during these trips lead to very productive collaborations, the first being with N. Christlieb. To him I am very grateful for the time I spent in Heidelberg, the collaboration and observing proposal on silver as well as the spectra I received from him, which are part of my project. I am also very grateful to K.-L. Kratz for offering me the possibility to go to Mainz and for the model predictions (data) he made available to me. In this connection I wish to thank both K.-L. Kratz and O. Hallmann for the help and very useful discussions they had with me. Furthermore, I wish to give my thanks to C. Sneden, who provided me with spectra and helped correcting one of my publications, both contributions are important to my thesis. S. Wanajo, H.T. Janka and B. Müller provided data from their SN models as well as interesting scientific discussions all of which I am very grateful for. Another large contribution to this and a former project of mine I received from the 'First Stars' collaboration, in which I am particularly grateful to M. Spite, J. Andersen, B. Nordströem and P. Bonifacio for providing the opportunity to collaborate with them in Paris and for offering help and very detailed discussions on our common paper. In this connection I am also thankful to P. Molaro, F. spite and T. Beers for their feedback. Additionally, I wish to thank B. Nordströem and J. Andersen for being there for me during more difficult times ready to help, not only in a scientific way. Help and useful discussions were also provided by J. Soebeck, to whom I am also grateful. L. Casagrande deserves to be acknowledged for providing me with temperature estimates. I have repeatedly received comments and language corrections from J. L. Connelly to whom I am grateful not just for these corrections but also for our friendship. Friendship, collaborations, help with language and discussions with P. Jofre, T. Maedler, L. Porter, N. Lützgendorf, P. Klaassen, L. Sbordone, R. Smiljanic and M. Alves-Cruz helped me write this thesis and I am therefore very grateful to all of you. A general acknowledgement to all the support received from the IMPRS and fifth floor students, secretaries, Helpdesk and E. Emsellem for helping me throughout my stay in Garching. Finally, the largest

gratitude and thankfulness goes to my family; my parents, my brother and my aunt, who have encouraged, supported and backed me up during my entire PhD regardless of time and situation.

Appendix A

Appendix

Table A.1. The Fe I line list, with wavelength, excitation potential, log gf and references.

λ[Å]	χ [eV]	log gf [dex]	reference
3536.56	2.88000	0.115000	S
3640.39	2.73000	-0.107000	S
3917.18	0.990000	-2.15500	S
4021.87	2.76000	-0.729000	S
4072.51	3.43000	-1.44000	J20
4076.64	3.21000	-0.530000	J21
4147.68	1.49000	-2.06000	J22
4154.50	2.83000	-0.690000	J21
4156.81	2.83000	-0.810000	J21
4157.79	3.42000	-0.400000	J21
4174.92	0.920000	-2.93000	J22
4175.64	2.85000	-0.830000	J21
4182.39	3.02000	-1.18000	J21
4187.04	2.45000	-0.548000	S
4199.10	3.05000	0.155000	S/N
4202.03	1.49000	-0.670000	J22
4222.21	2.45000	-0.967000	S
4224.18	3.37000	-0.510000	J21
4227.44	3.33000	0.270000	J21
4233.60	2.48000	-0.604000	S/N
4250.12	2.47000	-0.405000	S/N
4271.76	1.49000	-0.120000	J22
4282.40	2.18000	-0.779000	S/N
4337.05	1.56000	-1.66000	J22
4375.93	0.00000	-3.03100	S
4383.55	1.49000	0.240000	J22
4388.41	3.60000	-0.680000	J21
4389.24	0.0500000	-4.54000	J22
4404.75	1.56000	-0.100000	J22
4415.13	1.61000	-0.620000	J21
4427.31	0.0500000	-2.92400	(S)
4430.62	2.22000	-1.62000	J22
4439.88	2.28000	-2.96000	J22
4442.34	2.20000	-1.25500	(S)
4443.20	2.86000	-1.04000	J21
4445.48	0.0900000	-5.40000	J22
4447.73	2.22000	-1.34000	J21
4454.39	2.83000	-1.30000	J21
4461.65	0.0900000	-3.21000	S
4471.68	0.110000	-5.95000	J22
4484.23	3.60000	-0.860000	J21
4489.74	0.120000	-3.93000	J22
4494.56	2.20000	-1.13600	S
4531.15	1.49000	-2.11000	J22
4871.32	2.86500	-0.363000	Vc
4872.14	2.88200	-0.567000	Vc
4885.43	3.88200	-0.971000	V
4890.75	2.87500	-0.394000	V
4891.49	2.85100	-0.112000	V
4918.99	2.87000	-0.342000	(S/N)
4920.50	2.83000	0.0680000	(S/N)
4966.09	3.33200	-0.871000	V
4973.10	3.96000	-0.950000	V
4985.25	3.92800	-0.560000	V
4994.13	0.915000	-2.96900	R
5014.94	3.94300	-0.303000	V
5022.23	3.98400	-0.530000	V
5028.13	3.57300	-1.12200	R
5044.21	2.85100	-2.01700	R
5060.08	0.00000	-5.43100	R
5083.34	0.958000	-2.84200	R

Table A.1. continued.

λ[Å]	χ [eV]	log gf [dex]	reference
5127.36	0.915000	-3.24900	R
5141.74	2.42400	-2.23800	R
5191.46	3.04000	-0.551000	S/V
5192.34	3.00000	-0.421000	(S)
5194.94	1.56000	-2.09000	S
5198.71	2.22300	-2.09100	R
5215.18	3.26600	-0.871000	V
5217.39	3.21100	-1.16200	R
5225.53	0.110000	-4.75500	R
5229.85	3.28300	-0.967000	V
5232.94	2.94000	-0.0580000	S
5242.49	3.63400	-0.967000	V
5247.05	0.0870000	-4.97500	R
5263.31	3.26600	-0.879000	V
5266.56	3.00000	-0.386000	S
5269.54	0.860000	-1.32100	S
5281.79	3.03800	-0.834000	(V)
5324.18	3.21000	-0.103000	S
5371.49	0.960000	-1.64500	(S)
5302.30	3.28300	-0.720000	V
5307.36	1.60800	-2.91200	R
5324.18	3.21100	-0.103000	V
5339.93	3.26600	-0.647000	V
5364.87	4.44600	0.228000	R
5365.40	3.57300	-1.02000	R
5383.37	4.31200	0.645000	R
5393.17	3.24100	-0.715000	V
5405.77	0.990000	-1.84400	S
5415.20	4.38600	0.643000	R
5501.46	0.958000	-3.04600	R
5506.78	0.990000	-2.78900	R
5569.62	3.41700	-0.486000	V
5576.09	3.43000	-1.00000	V
5586.76	3.36800	-0.120000	V
5624.54	3.41700	-0.755000	V
5701.54	2.55900	-2.14300	R
5883.82	3.96000	-1.31400	V
5905.67	4.65200	-0.768000	V
5909.97	3.21100	-2.58700	V
5916.25	2.45300	-2.99400	V
5927.79	4.65200	-1.06700	V
5929.68	4.54900	-1.38400	V
5934.65	3.92900	-1.12300	V
5952.72	3.98400	-1.39400	V
5956.69	0.859000	-4.49800	R
6027.05	4.07600	-1.08900	V
6065.48	2.60900	-1.41000	R
6079.01	4.65200	-1.09600	V
6082.71	2.22300	-3.57300	V
6093.64	4.60800	-1.47400	V
6094.37	4.65200	-1.91500	V
6096.67	3.98400	-1.88300	V
6127.91	4.14300	-1.39900	V
6136.62	2.45300	-1.41000	R
6136.99	2.19800	-2.95000	V
6137.69	2.58800	-1.40300	V
6151.62	2.17600	-3.37100	R
6157.73	4.07600	-1.21500	V
6165.36	4.14300	-1.47400	V
6173.34	2.22300	-2.88000	V

Table A.1. continued.

λ[Å]	χ [eV]	log gf [dex]	reference
6180.20	2.72800	-2.64900	V
6187.99	3.94300	-1.67000	V
6191.56	2.43300	-1.41600	V
6200.31	2.60900	-2.43700	V
6213.43	2.22300	-2.48100	R
6219.28	2.19800	-2.44800	R
6229.23	2.84500	-2.80500	V
6230.72	2.55900	-1.28100	V
6232.64	3.65400	-1.22300	V
6240.65	2.22300	-3.17300	R
6246.32	3.60300	-0.877000	V
6252.56	2.40400	-1.76700	R
6265.13	2.17600	-2.54000	R
6270.23	2.85800	-2.60900	V
6271.28	3.33200	-2.70300	V
6280.62	0.859000	-4.39000	V
6297.79	2.22300	-2.74000	V
6301.50	3.65400	-0.718000	V
6311.50	2.83200	-3.14100	V
6322.69	2.58800	-2.42600	V
6335.33	2.19800	-2.17700	V
6336.82	3.68600	-0.856000	V
6338.88	4.79500	-1.03800	V
6344.15	2.43300	-2.87700	R
6355.03	2.84500	-2.29100	V
6364.37	4.79500	-1.40700	V
6380.74	4.18600	-1.37600	V
6393.60	2.43300	-1.57600	R
6408.02	3.68600	-1.01800	V
6411.65	3.65400	-0.717000	R
6419.95	4.73300	-0.275000	V
6430.85	2.17600	-1.94600	R
6469.19	4.83500	-0.808000	V
6475.62	2.55900	-2.94200	V
6481.87	2.27900	-3.01000	R
6494.98	2.40400	-1.23900	R
6495.74	4.83500	-0.917000	V
6496.47	4.79500	-0.606000	V
6498.94	0.958000	-4.68900	R
6533.93	4.55900	-1.42800	V
6546.24	2.75900	-1.53600	V
6592.91	2.72800	-1.47300	V
6593.87	2.43300	-2.42200	V
6597.56	4.79500	-1.04500	V
6667.71	4.58400	-2.11200	V
6677.99	2.69200	-1.41800	R
6699.14	4.59300	-2.10100	V
6703.57	2.75900	-3.06500	V
6739.52	1.55700	-4.79400	V
6750.15	2.42400	-2.58400	R
6752.71	4.63800	-1.20400	V
6786.86	4.19100	-2.02300	V
6793.26	4.07600	-2.32600	V
6804.00	4.65200	-1.49600	V
6804.27	4.58400	-1.81300	V
6806.84	2.72800	-2.13300	V
6810.26	4.60700	-0.986000	V
6820.37	4.63800	-1.28800	V
6828.59	4.63800	-0.888000	V
6837.01	4.59300	-1.68700	V

Table A.1. continued.

λ[Å]	χ [eV]	log gf [dex]	reference
6841.34	4.60700	-0.776000	V
6842.69	4.63800	-1.28700	V
6843.66	4.54900	-0.894000	V
6854.82	4.59300	-1.92600	V
6855.16	4.55900	-0.741000	V
6858.15	4.60800	-0.930000	V

J + 21 = Johnson & Bolte (2002) + O'Brian et al. (1991)
J + 22 = Johnson & Bolte (2002) + Blackwell et al.
N = Nissen et al. (2002, 2004, 2007)
R = Ryan et al. S = Hansen et al, 2010 submittet A&A + (Fuhr et al. 1988; O'Brian et al. 1991)
V = VALD (Kupka F. 2000)
() indicates that the line is blended and 'c' that the continuum is low in this region.

Table A.2. The Fe II line list, with wavelength, excitation potential, log gf and references.

λ[Å]	χ [eV]	log gf [dex]	reference
3106.56	3.81400	-1.89100	
3116.58	3.89200	-1.49700	
3135.36	3.89200	-1.10800	
3154.20	3.76800	-0.513000	
3163.09	1.67100	-2.84900	
3170.34	1.69500	-2.60600	
3185.32	1.72400	-2.81900	
3186.74	1.69500	-1.77100	
3193.80	1.72400	-1.78200	
3237.40	3.88900	-1.94000	
3255.89	0.986000	-2.55800	
3258.77	3.89200	-1.15400	
3277.35	0.986000	-2.38900	
3281.29	1.04000	-2.74000	
3289.35	3.81400	-1.56800	
3387.30	3.96700	-2.74800	
3406.76	3.94400	-2.74700	
3436.11	3.96700	-2.21600	
3535.62	3.89200	-2.96800	
4178.86	2.58300	-2.53500	
4233.17	2.58300	-1.94700	
4416.83	2.77800	-2.60200	
4489.18	2.82800	-2.97100	
4491.40	2.85600	-2.75600	
4508.29	2.85600	-2.34900	
4515.34	2.84400	-2.54000	
4520.22	2.80700	-2.61700	
4522.63	2.84400	-2.16900	
4541.52	2.85600	-2.97300	
4555.89	2.82800	-2.42100	
4576.34	2.84400	-2.97600	
4583.84	2.80700	-1.86700	
4923.93	2.89100	-1.50400	
4957.46	10.2730	-1.43100	
5004.19	10.2730	0.504000	
5018.44	2.89100	-1.34500	
5100.66	2.80700	-4.13500	B
5169.03	2.89100	-1.25000	
5197.58	3.23000	-2.34800	
5234.62	3.22100	-2.27900	
5254.93	3.23000	-3.33600	
5264.81	3.23000	-3.13300	
5284.11	2.89100	-3.19500	B
5325.55	3.22100	-3.32400	
5362.87	3.19900	-2.61600	
5414.07	3.22100	-3.64500	B
5425.26	3.19900	-3.39000	
5534.85	3.24500	-2.86500	B
6084.11	3.19900	-3.88100	
6149.26	3.88900	-2.72400	B
6238.39	3.88900	-2.75400	
6247.56	3.89200	-2.32900	B
6416.92	3.89200	-2.87700	
6432.68	2.89100	-3.50100	

B = Biémont
' ' = VALD (Kupka F. 2000)

Bibliography

Alonso, A., Arribas, S., & Martinez-Roger, C. 1994, Astronomy & Astrophysics Supplement Series, 107, 365

Alonso, A., Arribas, S., & Martinez-Roger, C. 1995, Astronomy & Astrophysics, 297, 197

Alonso, A., Arribas, S., & Martinez-Roger, C. 1996a, Astronomy & Astrophysics Supplement Series, 117, 227

Alonso, A., Arribas, S., & Martinez-Roger, C. 1996b, Astronomy & Astrophysics, 313, 873

Alonso, A., Arribas, S., & Martínez-Roger, C. 1999, Astronomy & Astrophysics Supplement Series, 140, 261

Andrievsky, S. M., Spite, M., Korotin, S. A., et al. 2009, Astronomy & Astrophysics, 494, 1083

Argast, D., Samland, M., Thielemann, F., & Qian, Y. 2004, Astronomy & Astrophysics, 416, 997

Arlandini, C., Käppeler, F., Wisshak, K., et al. 1999, Astrophysical Journal, 525, 886

Arnett, D. 1996, Supernovae and nucleosynthesis: an investigation of the history of matter, from the big bang to present (Princeton University Press)

Asplund, M. 2005, Annual Review of Astronomy & Astrophysics, 43, 481

Asplund, M., Grevesse, N., Sauval, A. J., & Scott, P. 2009, Annual Review of Astronomy & Astrophysics, 47, 481

Barklem, P. S., Christlieb, N., Beers, T. C., et al. 2005, Astronomy & Astrophysics, 439, 129

Beers, T. C., Preston, G. W., & Shectman, S. A. 1985, Astronomical Journal, 90, 2089

Beers, T. C., Preston, G. W., & Shectman, S. A. 1992, Astronomical Journal, 103, 1987

Belyakova, E. V. & Mashonkina, L. I. 1997, Astronomy Reports, 41, 530

Bessell, M. S. 2005, Annual Review of Astronomy & Astrophysics, 43, 293

Biémont, E. 1974, , 14, 959

Blackwell, D. E., Petford, A. D., & Simmons, G. J. 1982, Mon. Not. R. Astron. Soc, 201, 595

Bonifacio, P., Monai, S., & Beers, T. C. 2000, Astronomical Journal, 120, 2065

Bonifacio, P., Spite, M., Cayrel, R., et al. 2009, Astronomy & Astrophysics, 501, 519

Brandsden, B. H. & Joachain, C. J. 2003, Physics of Atoms and Molecules (Prentice Hall)

Bromm, V. 2010, in IAU Symposium, Vol. 265, IAU Symposium, ed. K. Cunha, M. Spite, & B. Barbuy, 27–33

Burbidge, E. M., Burbidge, G. R., Fowler, W. A., & Hoyle, F. 1957, Reviews of Modern Physics, 29, 547

Burris, D. L., Pilachowski, C. A., Armandroff, T. E., et al. 2000, Astrophysical Journal, 544, 302

Busso, M., Gallino, R., & Wasserburg, G. J. 1999, Annual Review of Astronomy & Astrophysics, 37, 239

Caffau, E., Ludwig, H., Steffen, M., Freytag, B., & Bonifacio, P. 2010, , 66

Carlsson, J., Jönsson, P., & Sturesson, L. 1990, Zeitschrift fur Physik D Atoms Molecules Clusters, 16, 87

Casagrande, L. 2008, Physica Scripta Volume T, 133, 014020

Casagrande, L., Ramírez, I., Meléndez, J., Bessell, M., & Asplund, M. 2010, Astronomy & Astrophysics, 512, A54+

Cayrel, R. 2006, Reports on Progress in Physics, 69, 2823

Cayrel, R., Depagne, E., Spite, M., et al. 2004, Astronomy & Astrophysics, 416, 1117

Chaboyer, B., Fenton, W. H., Nelan, J. E., Patnaude, D. J., & Simon, F. E. 2001, Astrophysical Journal, 562, 521

Christensen-Dalsgaard, J. 2004, Stellar Structure and Evolution (Springer)

Christlieb, N., Beers, T. C., Barklem, P. S., et al. 2004, Astronomy & Astrophysics, 428, 1027

Christlieb, N., Green, P. J., Wisotzki, L., & Reimers, D. 2001a, Astronomy & Astrophysics, 375, 366

Christlieb, N., Wisotzki, L., Reimers, D., et al. 2001b, Astronomy & Astrophysics, 366, 898

Cowan, J. J., Pfeiffer, B., Kratz, K., et al. 1999, Astrophysical Journal, 521, 194

Cowan, J. J. & Sneden, C. 2006, Nature, 440, 1151

Cowan, J. J., Sneden, C., Burles, S., et al. 2002, Astrophysical Journal, 572, 861

Cowan, J. J., Sneden, C., & Truran, J. W. 2001, in American Institute of Physics Conference Series, Vol. 586, 20th Texas Symposium on relativistic astrophysics, ed. J. C. Wheeler & H. Martel, 337–342

Cowan, R. D. 1981, The theory of atomic structure and spectra, ed. Cowan, R. D.

Crawford, J. L., Sneden, C., King, J. R., Boesgaard, A. M., & Deliyannis, C. P. 1998, Astronomical Journal, 116, 2489

Dekker, H., D'Odorico, S., Kaufer, A., Delabre, B., & Kotzlowski, H. 2000, in Presented at the Society of Photo-Optical Instrumentation Engineers (SPIE) Conference, Vol. 4008, Society of Photo-Optical Instrumentation Engineers (SPIE) Conference Series, ed. M. Iye & A. F. Moorwood, 534–545

D'Odorico, S., ed. 1998, Society of Photo-Optical Instrumentation Engineers (SPIE) Conference Series, Vol. 3355, Optical Astronomical Instrumentation

Emerson, D. 1996, Interpreting Astronomical Spectra (Wiley)

Farouqi, K., Kratz, K., Mashonkina, L. I., et al. 2009, Astrophysical Journal Letters, 694, L49

Farouqi, K., Kratz, K., Pfeiffer, B., et al. 2010, Astrophysical Journal, 712, 1359

François, P., Depagne, E., Hill, V., et al. 2007, Astronomy & Astrophysics, 476, 935

Freiburghaus, C., Rosswog, S., & Thielemann, F. 1999, Astrophysical Journal Letters, 525, L121

Fuhr, J. R., Martin, G. A., & Wiese, W. L. 1988, Journal of Physical and Chemical Reference Data, Volume 17, Suppl. 4. New York: American Institute of Physics (AIP) and American Chemical Society, 1988, 17

Gallagher, A. J., Ryan, S. G., García Pérez, A. E., & Aoki, W. 2010, ArXiv e-prints

Gilroy, K. K., Sneden, C., Pilachowski, C. A., & Cowan, J. J. 1988, Astrophysical Journal, 327, 298

Gratton, R. G., Bonifacio, P., Bragaglia, A., et al. 2001, Astronomy & Astrophysics, 369, 87

Gustafsson, B., Edvardsson, B., Eriksson, K., et al. 2008, Astronomy & Astrophysics, 486, 951

Hammond, C., R. 2004, The Elements, in Handbook of Chemistry and Physics 81st edition (CRC press)

Hansen, C. J., Nordström, B., Bonifacio, B., et al. 2011b, Astronomy & Astrophysics, accepted

Hansen, C. J. & Primas, F. 2011, Astronomy & Astrophysics, 525

Heger, A. & Woosley, S. E. 2002, in Nuclear Astrophysics, ed. W. Hillebrandt & E. Müller, 8–13

Heil, M., Juseviciute, A., Käppeler, F., et al. 2009, Publications of the Astronomical Society of Australia, 26, 243

Hill, V., Plez, B., Cayrel, R., et al. 2002, Astronomy & Astrophysics, 387, 560

Honda, S., Aoki, W., Ishimaru, Y., Wanajo, S., & Ryan, S. G. 2006, Astrophysical Journal, 643, 1180

Honda, S., Aoki, W., Kajino, T., et al. 2004, Astrophysical Journal, 607, 474

Ishimaru, Y., Wanajo, S., Aoki, W., & Ryan, S. G. 2004, Astrophysical Journal Letters, 600, L47

Izutani, N., Umeda, H., & Tominaga, N. 2009, Astrophysical Journal, 692, 1517

Jofré, P., Panter, B., Hansen, C. J., & Weiss, A. 2010, Astronomy & Astrophysics, 517, A57+

Johnson, J. A. & Bolte, M. 2002, Astrophysical Journal, 579, 616

Kobayashi, C., Umeda, H., Nomoto, K., Tominaga, N., & Ohkubo, T. 2006, Astrophysical Journal, 653, 1145

Korn, A. J. 2008, in Astronomical Society of the Pacific Conference Series, Vol. 384, 14th Cambridge Workshop on Cool Stars, Stellar Systems, and the Sun, ed. G. van Belle, 33–+

Korn, A. J., Grundahl, F., Richard, O., et al. 2006, Nature, 442, 657

Kratz, K., Farouqi, K., Pfeiffer, B., et al. 2007, Astrophysical Journal, 662, 39

Kupka F., Ryabchikova T.A., P. N. S. H. W. W. 2000, Baltic Astronomy, 9, 590

Kurucz, R. L. 1993, in Astronomical Society of the Pacific Conference Series, Vol. 44, IAU Colloq. 138: Peculiar versus Normal Phenomena in A-type and Related Stars, ed. M. M. Dworetsky, F. Castelli, & R. Faraggiana, 87–+

Lai, D. K., Bolte, M., Johnson, J. A., et al. 2008, Astrophysical Journal, 681, 1524

Lind, K., Korn, A. J., Barklem, P. S., & Grundahl, F. 2008, Astronomy & Astrophysics, 490, 777

Masana, E., Jordi, C., & Ribas, I. 2006, Astronomy & Astrophysics, 450, 735

Mashonkina, L., Gehren, T., Shi, J., Korn, A., & Grupp, F. 2010, in IAU Symposium, Vol. 265, IAU Symposium, ed. K. Cunha, M. Spite, & B. Barbuy, 197–200

Masseron, T. 2006, PhD thesis, Observatoire de Paris

Matteucci, F. 2008, in IAU Symposium, Vol. 250, IAU Symposium, ed. F. Bresolin, P. A. Crowther, & J. Puls, 391–400

McWilliam, A., Preston, G. W., Sneden, C., & Shectman, S. 1995, Astronomical Journal, 109, 2736

Meléndez, J., Asplund, M., Gustafsson, B., Yong, D., & Ramírez, I. 2010, in IAU Symposium, Vol. 265, IAU Symposium, ed. K. Cunha, M. Spite, & B. Barbuy, 412–415

Meyer, B. 1994, Annu. Rev. Astro. Astrophys., 32, 153

Montes, F., Beers, T. C., Cowan, J., et al. 2007, Astrophysical Journal, 671, 1685

Moore, C. E., Minnaert, M. G. J., & Houtgast, J. 1966, The solar spectrum 2935 A to 8770 A, ed. Moore, C. E., Minnaert, M. G. J., & Houtgast, J.

Mucciarelli, A., Salaris, M., Lovisi, L., et al. 2010, ArXiv e-prints

Nave, G., Johansson, S., & Thorne, A. P. 1997, Journal of the Optical Society of America B Optical Physics, 14, 1035

Nidever, D. L., Marcy, G. W., Butler, R. P., Fischer, D. A., & Vogt, S. S. 2002, Astrophysical Journal Supplement Series, 141, 503

Nissen, P. E., Akerman, C., Asplund, M., et al. 2007, Astronomy & Astrophysics, 469, 319

Nissen, P. E., Chen, Y. Q., Asplund, M., & Pettini, M. 2004, Astronomy & Astrophysics, 415, 993

Nissen, P. E., Hoeg, E., & Schuster, W. J. 1997, in ESA Special Publication, Vol. 402, Hipparcos - Venice '97, ed. R. M. Bonnet, E. Høg, P. L. Bernacca, L. Emiliani, A. Blaauw, C. Turon, J. Kovalevsky, L. Lindegren, H. Hassan, M. Bouffard, B. Strim, D. Heger, M. A. C. Perryman, & L. Woltjer, 225–230

Nissen, P. E., Primas, F., Asplund, M., & Lambert, D. L. 2002, Astronomy & Astrophysics, 390, 235

Nordström, B., Mayor, M., Andersen, J., et al. 2004, Astronomy & Astrophysics, 418, 989

O'Brian, T. R., Wickliffe, M. E., Lawler, J. E., Whaling, W., & Brault, J. W. 1991, Journal of the Optical Society of America B Optical Physics, 8, 1185

Önehag, A., Gustafsson, B., Eriksson, K., & Edvardsson, B. 2009, Astronomy & Astrophysics, 498, 527

Pickering, J. C. & Zilio, V. 2001, European Physical Journal D, 13, 181

Pignatari, M., Gallino, R., Heil, M., et al. 2010, Astrophysical Journal, 710, 1557

Preston, G. W., Sneden, C., Thompson, I. B., Shectman, S. A., & Burley, G. S. 2006, Astronomical Journal, 132, 85

Primas, F. 2010, in IAU Symposium, Vol. 268, IAU Symposium, ed. C. Charbonnel, M. Tosi, F. Primas, & C. Chiappini, 221–230

Primas, F., Molaro, P., & Castelli, F. 1994, Astronomy & Astrophysics, 290, 885

Qian, Y. 2002, Astrophysical Journal Letters, 569, L103

Ramírez, I. & Meléndez, J. 2005, Astrophysical Journal, 626, 465

Rauscher, T. & Thielemann, F. 2000, Atomic Data and Nuclear Data Tables, 75, 1

Roberts, L. F., Woosley, S., Heger, A., & Hoffman, R. 2008, in Nuclei in the Cosmos (NIC X)

Roederer, I. U. 2009, Astronomical Journal, 137, 272

Ross, J. E. & Aller, L. H. 1972, Solar Physics, 25, 30

Ryan, S. G., Norris, J. E., & Bessell, M. S. 1991, Astronomical Journal, 102, 303

Salaris, M., Groenewegen, M. A. T., & Weiss, A. 2000, Astronomy & Astrophysics, 355, 299

Schlegel, D. J., Finkbeiner, D. P., & Davis, M. 1998, Astrophysical Journal, 500, 525

Seeger, P. A., Fowler, W. A., & Clayton, D. D. 1965, Astrophysical Journal Supplement Series, 11, 121

Sneden, C., Cowan, J. J., & Gallino, R. 2008, Annual Review of Astronomy & Astrophysics, 46, 241

Sneden, C., Cowan, J. J., Ivans, I. I., et al. 2000, Astrophysical Journal Letters, 533, L139

Sneden, C., Cowan, J. J., Lawler, J. E., et al. 2003, Astrophysical Journal, 591, 936

Sneden, C., Lawler, J. E., Cowan, J. J., Ivans, I. I., & Den Hartog, E. A. 2009, Astrophysical Journal Supplement Series, 182, 80

Sneden, C., Preston, G. W., McWilliam, A., & Searle, L. 1994, Astrophysical Journal Letters, 431, L27

Sneden, C. A. 1973, PhD thesis, THE UNIVERSITY OF TEXAS AT AUSTIN.

Tautvaisiene, G. 1997, Mon. Not. R. Astron. Soc, 286, 948

Vogt, S. S., Allen, S. L., Bigelow, B. C., et al. 1994, in Society of Photo-Optical Instrumentation Engineers (SPIE) Conference Series

Wanajo, S., Janka, H., & Mueller, B. 2010, ArXiv e-prints

Wanajo, S., Kajino, T., Mathews, G. J., & Otsuki, K. 2001, Astrophysical Journal, 554, 578

Wanajo, S., Nomoto, K., Janka, H., Kitaura, F. S., & Müller, B. 2009, Astrophysical Journal, 695, 208

Wanajo, S., Tamamura, M., Itoh, N., et al. 2003, Astrophysical Journal, 593, 968

Wasserburg, G. J. & Qian, Y. 2000, Astrophysical Journal Letters, 529, L21

Wisotzki, L., Koehler, T., Groote, D., & Reimers, D. 1996, Astronomy & Astrophysics Supplement Series, 115, 227